1 Nuclear Magnetic Resonance Imaging and Spectroscopy

Anne Leroy-Willig and
Danielle Geldwerth-Feniger

1.0 Introduction

Nuclear magnetic resonance (NMR) detects the magnetic moments of nuclei using their orientation in a strong magnetic field and their response at a specific resonance frequency. Discovered in 1946 by Bloch and Purcell, NMR spectroscopy (MRS), at first used for chemical and physical studies, quickly became a major tool for spectroscopic analysis of complex molecules and further of biochemical systems. Then in the 1980s, NMR gave rise to magnetic resonance imaging (MRI), a medical imaging technique very attractive despite its cost, from the profusion of anatomical and physiological information available.

In biomedical research, the two modalities, imaging (MRI) and spectroscopy (MRS) are increasingly used for *in vivo* animal studies, with benefit from the technical developments carried out for human studies. These two modalities give access to various data ranging from three dimentional (3D) anatomy to physiological and biochemical information, and many applications are available via specific measurement techniques that we will shortly explain here.

NMR is fully based upon quantum physics. Here we give a simplified and then by some ways approximate description, mixing classic and quantum physics, in paragraphs one to six; the later paragraphs are oriented towards *in vivo* explorations.

In this chapter, several levels of information are given, which are as follows: readers can jump the paragraphs labelled as 'more physics' or 'more technology'; also they may read only key points before coming to the following paragraph. For those who wish to know more about MRI and MRS, more complete descriptions are given in a free access Web book (Hornack, 2005), in books by Webb (2003) and Bushberg *et al.* (2001), and concerning the toolbox of MRI sequences, in Ness Aiver (1997) with a fully graphic presentation. Gadian (1995) wrote an excellent introduction to *in vivo* MRS.

1.1 Magnets and magnetic field

In everyday life, a magnet is a piece of a material which attracts or repels another magnet and creates a magnetic field. For example, the magnetic bar shown in Figure 1.1.1(a) has two poles; the magnetic field it creates goes from the North Pole to the South Pole. The magnetic field all around this magnet can be probed by its action, which is the force exerted on another magnet. For example, the weak earth's magnetic field acts upon a needle compass: The compass rotates and lines along the magnetic field pointing towards the magnetic North.

Magnetism is the fundamental property of matter. The magnetism of nuclei is weak, hidden behind the stronger contribution of electrons, and one may easily ignore its existence. Magnetism is the result of moving electrical charges (mostly the electrons). The magnetic field, the mediator of magnetic force, is created either by electric current flowing in a wire or by the microscopic electric circuits, which exist inside materials like iron, at the atomic scale.

Figure 1.1.1 How to create a magnetic field.
(a) The magnet bar, a rod made with iron, is a permanent source of magnetic field throughout space. The field lines (black curves), that indicate the direction of the magnetic field, go from North Pole to South Pole. A small needle compass lines along the direction of the magnetic field.
(b) A loop of copper wire, fed with electrical current, creates a magnetic field with similar spatial distribution at long distance as indicated by field lines.
(c) A solenoidal winding is made by many conductive wire loops winded upon a cylinder. In the central part of the cylinder, the magnetic field is lined along the axis of the cylinder (white lines) and is homogeneous

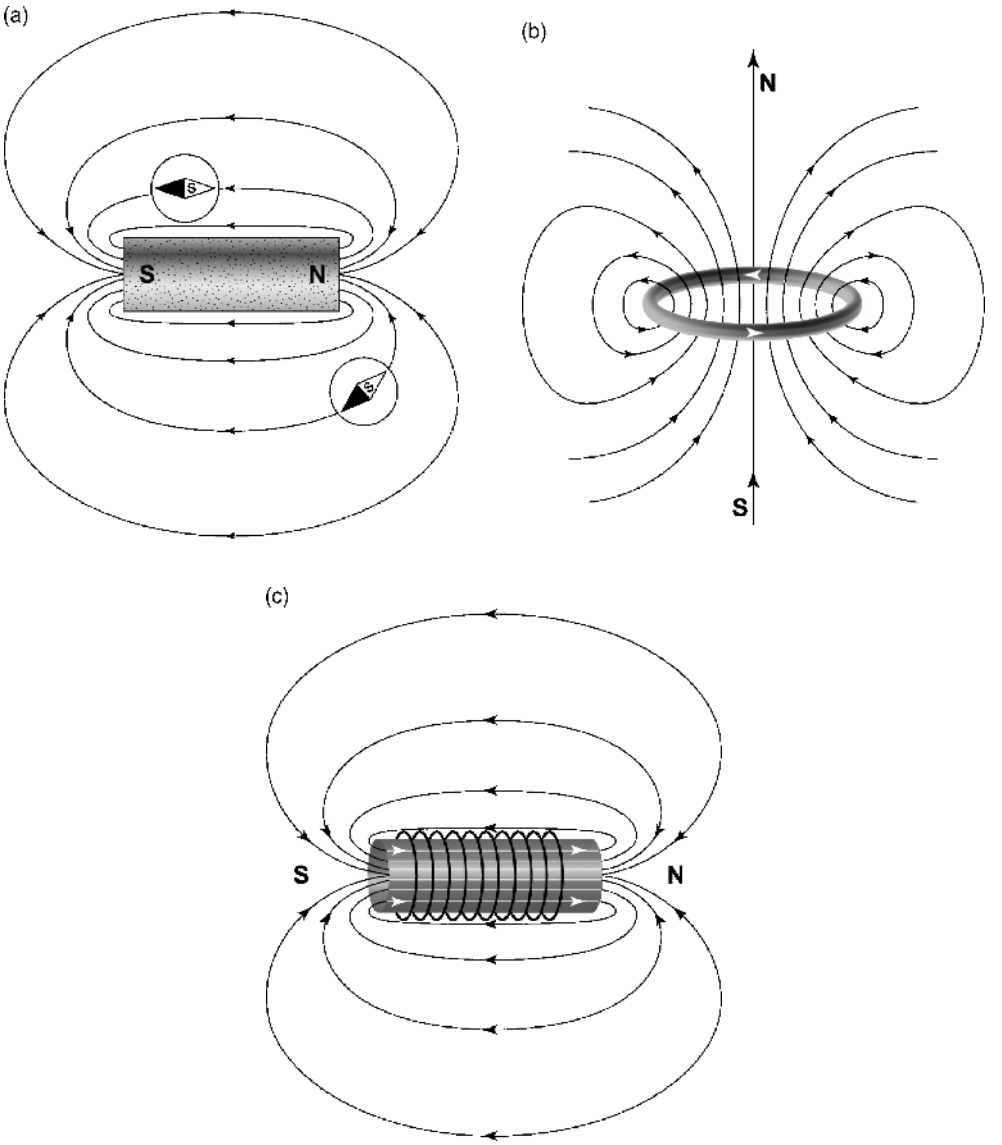

The magnetic field is measured in Tesla or in Gauss, with $1\,\mathrm{T} = 10^4\,\mathrm{G}$. (*Note that we make a rather loose use of magnetic units, forgetting the difference between magnetic field and magnetic induction, only needed when studying ferromagnetic materials.*)

Another simple magnet is made by a circular loop of copper wire fed with electric current, shown in Figure 1.1.1(b). A basic physical law tells us that the magnetic field created by a current rotates around the wire where the electric current is flowing. Then the magnetic field is perpendicular to the circle at its centre; elsewhere its intensity and its direction vary through space. The solenoid is made with multiple loops of wire coiled upon a cylinder (Figure 1.1.1(c)). The magnetic field inside the cylinder is very homogeneous.

1.1.1 More technology: The 'perpetual' magnet

Nearly all magnets for NMR are solenoids, made of supraconductive wire winded upon a hollow cylindrical support. Electric current circulates in the circuit that is immersed in a cryostat filled with liquid helium at temperature −269°C. Since the supraconductive wire has zero electrical resistance at low temperature, no electrical power is dissipated. This system creates a very stable magnetic field that may be disconnected from a power supply, as long as the temperature is kept low enough. The low temperature is maintained by high vacuum insulation that reduces liquid helium boil off.

Besides the high intensity, high homogeneity and stability of the magnetic field are also needed. The magnet is the more heavy and expensive piece of NMR hardware. There is a growing demand for high field magnets dedicated to biomedical research, but few centres can buy very high field magnets for large animals.

Big magnets delivering magnetic fields between 0.3 and 3 T are currently used for NMR human studies. For smaller animals, smaller magnets delivering higher fields (1.5 to 11 T) are currently used. *In vitro* experiments are done at still higher fields. For comparison, the earth magnetic field is 5×10^{-4} T (or 0.5 G).

Magnets for small animals are either vertical (as those commonly used for *in vitro* studies) or horizontal, yielding wider access and allowing more physiological housing of animals during NMR examination (as shown by Figure 1.1.2).

Figure 1.1.2 The supraconductive magnet used for NMR experiments. (a) High field supraconductive magnet for rats and mice NMR examination. This horizontal magnet, weighting 2 tons, delivers a magnetic field of 7 T inside a cylindrical access 30 cm wide. After installation of the shim and gradient coils, the access available for small animals is 15 cm wide. The chimney above the magnet is used for liquid helium refill. (b) Examination bed. The small animal is lain inside an anaesthesia chamber. The bed is positioned at the centre of the magnet bore during the examination (Courtesy of Bruker, SA, Ettlingen, Germany)

(a)

(b)

1.2 Nuclear magnetization

1.2.1 The magnetic moment of the nucleus

Key points
The nuclei that bear a net magnetic moment (such as ^{1}H, ^{31}P, ^{13}C) can be detected by NMR. Hydrogen nuclei, that bear the largest magnetic moment amongst stable nuclei, are detected to build *in vivo* NMR images. Hydrogen, phosphorus, sodium, fluorine nuclei are currently detected to build *in vivo* NMR spectra.

All elementary particles (electron, proton, neutron and others) bear a spin. The spin is purely quantic without strict correspondence in classical physics, but it can be described as a quantity of rotation of the particle spinning about one axis, where each spin $\vec{s}$ is associated with an elementary magnetic moment $\vec{\mu}$, related to the spin by a number, the gyromagnetic factor γ.

$$\vec{\mu} = \gamma . \vec{s} \qquad (1.1)$$

The elementary magnetic moment may be described as a tiny magnet that we will represent as an arrow; a more accurate description is possible only by quantum mechanics, out of our scope.

The spin is the kinetic moment of the particle (a 'quantity of rotation'), and the magnetic moment is always associated – and proportional – to this kinetic moment. (*Note that in many books, the word "spin" is written instead of 'magnetic moment'.)*

For one given nucleus, the magnetic moment is the sum of the magnetic moments of its protons and its neutrons. Hydrogen nucleus is made of one proton (Figure 1.2.1). When protons or neutrons are associated as pairs with their magnetic moments in opposed direction, these pairs have a net magnetic moment equal to zero. For example, the carbon nucleus ^{12}C (with 6 protons and 6 neutrons) cannot be detected by NMR, whereas the less abundant isotope ^{13}C (6 protons, 7 neutrons) has a detectable magnetic moment. *In vivo* NMR spectroscopy of ^{13}C allows the quantification of molecules such as glucose, acetate and glycogen.

Electrons bear a much larger elementary magnetic moment, nearly two thousand times bigger than that of protons. In most molecules, electrons are associated as pairs with their magnetic moments in opposed direction, and these pairs have nearly net zero magnetic moment. The iron atom has several non-paired electrons and then bears a large magnetic moment from its electrons, so that iron is a good material to experience what is magnetism, or to make magnets, and also NMR contrast agents (see paragraph 1.9).

1.2.2 The motion of a magnetic moment around the magnetic field and the resonance frequency

Key points
A magnetic moment rotates around the direction of the magnetic field $\vec{B_o}$ as does a spinning top. Its longitudinal component, along $\vec{B_o}$, is constant, whereas its transverse component, perpendicular to $\vec{B_o}$, rotates at the frequency F_o. F_o is proportional to the magnetic field intensity $\vec{B_o}$ and to the gyromagnetic factor characteristic of the nucleus, γ. The gyromagnetic factor γ has a characteristic value for each nucleus, so that at a given field value each kind of nucleus rotates at a specific frequency.

A magnetic moment $\vec{\mu}$ in presence of a magnetic field $\vec{B_o}$ is submitted to a torque: It rotates along a cone around the direction of the magnetic field, as does a spinning top. This special rotation is named precession (it is the name for the motion of a gyroscope when a torque is applied upon it). Then the longitudinal component of $\vec{\mu}$, μz, along $\vec{B_o}$, keeps a constant value, and the transverse component, μt, perpendicular to $\vec{B_o}$, rotates (Figure 1.2.2). The precession takes place at a well-defined frequency, F_o, proportional to the magnetic field intensity B_o and to the gyromagnetic factor, γ, characteristic of the nucleus.

F_o is the resonance frequency of this nucleus:

$$F_o = \gamma/2\pi.B_o \qquad (1.2)$$

The gyromagnetic factor γ is determined by the internal quantum structure of the nucleus. It has a characteristic value for each nucleus, so that at a given field value each kind of nucleus rotates at a specific frequency as shown in Table 1.2.1.

Figure 1.2.1 The hydrogen nuclear magnetic moment. The proton, with mass rotating upon itself, has some analogy with a spinning top. The positive charge rotating can also be described as some current flowing in a circuit and then behaves as a small magnet. Rotation (spin) is symbolized by the black arrow, magnetic moment by the grey arrow. The magnetic moment $\vec{\mu}$ and the spin $\vec{s}$ of a proton are collinear, and they are related by: $\vec{\mu} = \gamma.\vec{S}$, where γ is the gyromagnetic factor

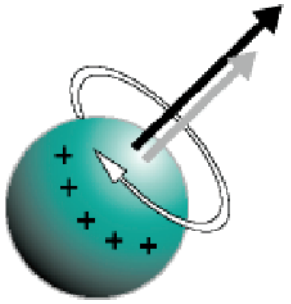

Figure 1.2.2 Precession of a magnetic moment around the magnetic field. The magnetic moment of a proton rotates around the field $\vec{B_o}$ tangentially to a cone. The angle between $\vec{\mu}$ and $\vec{B_o}$ is constant; the projection of $\vec{\mu}$ on the direction of $\vec{B_o}$, μz – named the longitudinal component, has a fixed value. The projection upon the plane perpendicular to $\vec{B_o}$, μt – named the transverse component, rotates at the frequency F_o

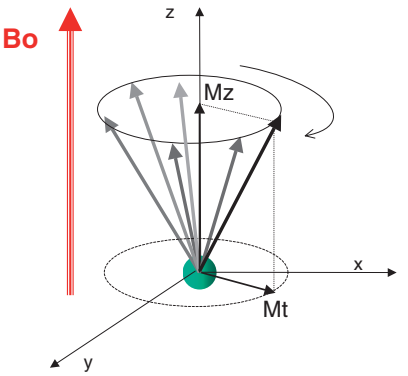

1.2.3 Resonance frequencies of nuclei of biological research

Amongst the stable nuclei, the hydrogen nucleus has the highest gyromagnetic factor and then the highest resonance frequency at a given magnetic field. NMR signals of hydrogen are currently detected at frequencies between 64 and 900 MHz (corresponding to magnetic field intensity between 1.5 T and 21.13 T). Other nuclei resonate at lower frequencies, because they have lower magnetic moments. These resonance frequencies are in the range used for radio, telephones and radars. In Table 1.2.1, the gyromagnetic factor γ of nuclei is expressed by their resonance frequency at $B_o = 4.7$ T (the field of many NMR spectrometers used for small animal examinations).

Table 1.2.1 Nuclear magnetic resonance frequencies at Bo = 4.7 Tesla for nuclei of biological interest

Nucleus	Frequency at 4.7 Tesla (MHz)	Natural abundance (%)	Sensitivity*
^{1}H	200	99.98	1
^{3}He	152.4	$1.3 \cdot 10^{-4}$	6.10^{-5}**
^{13}C	50.2	1.1	$0.18 \cdot 10^{-3}$
^{19}F	188.2	100	0.85
^{23}Na	52.9	100	0.136
^{31}P	80.9	100	0.063

*The sensitivity for a given nucleus is the ratio of its signal to the signal of hydrogen, at same number of atoms (taking into account the natural abundance of the isotope detected), at the same magnetic field. The sensitivity for ^{13}C is low because ^{13}C nuclei are only 1.1% of all carbon nuclei. The sensitivity varies as the square of the gyromagnetic ratio of the nucleus.

**This nucleus is detected at abundance higher than its weak natural abundance, after separation from ^{4}He, and after hyperpolarization (cf paragraph 1.10.1).

1.2.4 The nuclear magnetization

Key points
Nuclear magnetization is the sum of the individual magnetic moments per unit volume.

In presence of the external magnetic field B_o, individual magnetic moments are lined either parallel or anti-parallel to B_o, corresponding to two energy levels. The weak difference between the populations in these two energy levels determines the nuclear magnetization. At equilibrium, the nuclear magnetization is parallel to B_o, and its value M_o is proportional to the number of nuclei N and to B_o.

The magnetization is the sum of the individual magnetic moments in one unity of volume. These magnetic moments are borne by nuclei and electrons.

Here we consider only the magnetization from the nuclei, that we call 'nuclear magnetization', and only the contribution from the nuclei to be detected (very often hydrogen nuclei).

Let us consider a water sample of volume V that contains N hydrogen nuclei. In the absence of external magnetic field, the individual nuclear magnetic moments are oriented randomly with zero sum, and then the total magnetization is equal to zero (Figure 1.2.3(a)).

In the magnetic field $\vec{B}_o$, they do not behave as a classic magnet: A compass needle would always align with the field. Here they orientate either along or opposite the magnetic field (Figure 1.2.3(b)). Their z-component μz is quantified, taking values $+\mu$ or $-\mu$.

The magnetic energy of a magnetic moment $\vec{\mu}$ in the field $\vec{B}_o$ is given by

$$E = -\vec{\mu}.\vec{B}_o \tag{1.3}$$

The two orientations relative to B_o determine two energy levels. The energy of the lower level is $E^+ = -\mu.B_o$, for $\vec{\mu}$ parallel to $\vec{B}_o$ (assuming μ is positive).

The energy of the upper level is $E^- = +\mu.B_o$, for $\vec{\mu}$ in the direction opposite to B_o.

The two levels are separated by

$$\Delta E = 2.\mu.B_o \tag{1.4}$$

If the N hydrogen nuclei were reparted equally between these two levels, magnetization would still be zero. From thermal agitation, the hydrogen nuclei are continually jumping from one energy level to the other. At equilibrium, N^+ nuclei are in the lower level (which is slightly more populated) and N^- nuclei are in the upper level as drawn in Figure 1.2.4.

The magnetization, the sum of individual moments, is parallel to the magnetic field $\vec{B}_o$, and has the value M_o:

$$M_o = (N^+ - N^-).\mu/V \tag{1.5}$$

This magnetization is much lower than $N.\mu/V$, which would be its value if all magnetic moments were in the lowest energy level. The magnetization at equilibrium

Figure 1.2.3 Nuclear magnetic moments and magnetization. The sum of the elementary magnetic moments in a unit volume is the magnetization. (a) At zero magnetic field, the magnetic moments are randomly oriented. (b) At the magnetic field intensity B_o, the magnetic moments are oriented either parallel or anti-parallel to $\vec{B}_o$ and their sum is parallel to $\vec{B}_o$

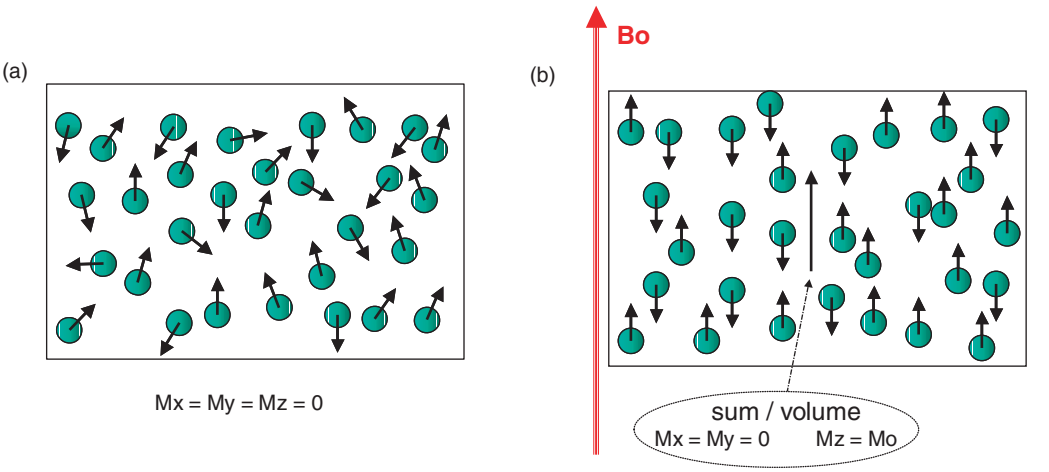

Figure 1.2.4 Population of the nuclear energy levels.
(a) Magnetic moments at equilibrium in the magnetic field B_o. The energy levels corresponding to the two orientations relative to B_o are separated by $\Delta E = 2\ \mu\ B_o$. The lower level contains N^+ hydrogen nuclei; the upper level contains N^- hydrogen nuclei. The net magnetization of the sample is $M_o = (N^+ - N^-)\ \mu/V$.
(b) Excitation of nuclear magnetic resonance. Photons from the electromagnetic field B_1, that have the energy $h\ F_o = \Delta E$, are absorbed and allow magnetic moments in the lower level to reach the upper level: The populations N^+ and N^- are modified by the absorption of photons. When $N^+ = N^-$ the longitudinal magnetization is equal to zero, while the photons have brought their polarization to the transverse magnetization that is no longer equal to zero.
(c) Energy levels and longitudinal relaxation. The recovery of M_z to equilibrium, or longitudinal relaxation, derives from rebuilding the difference between the populations N^+ and N^- of the two energy levels of hydrogen nuclei magnetic moments. The hydrogen nuclei that have been previously excited to the upper level have to emit the excess of energy in order to return to the lower level

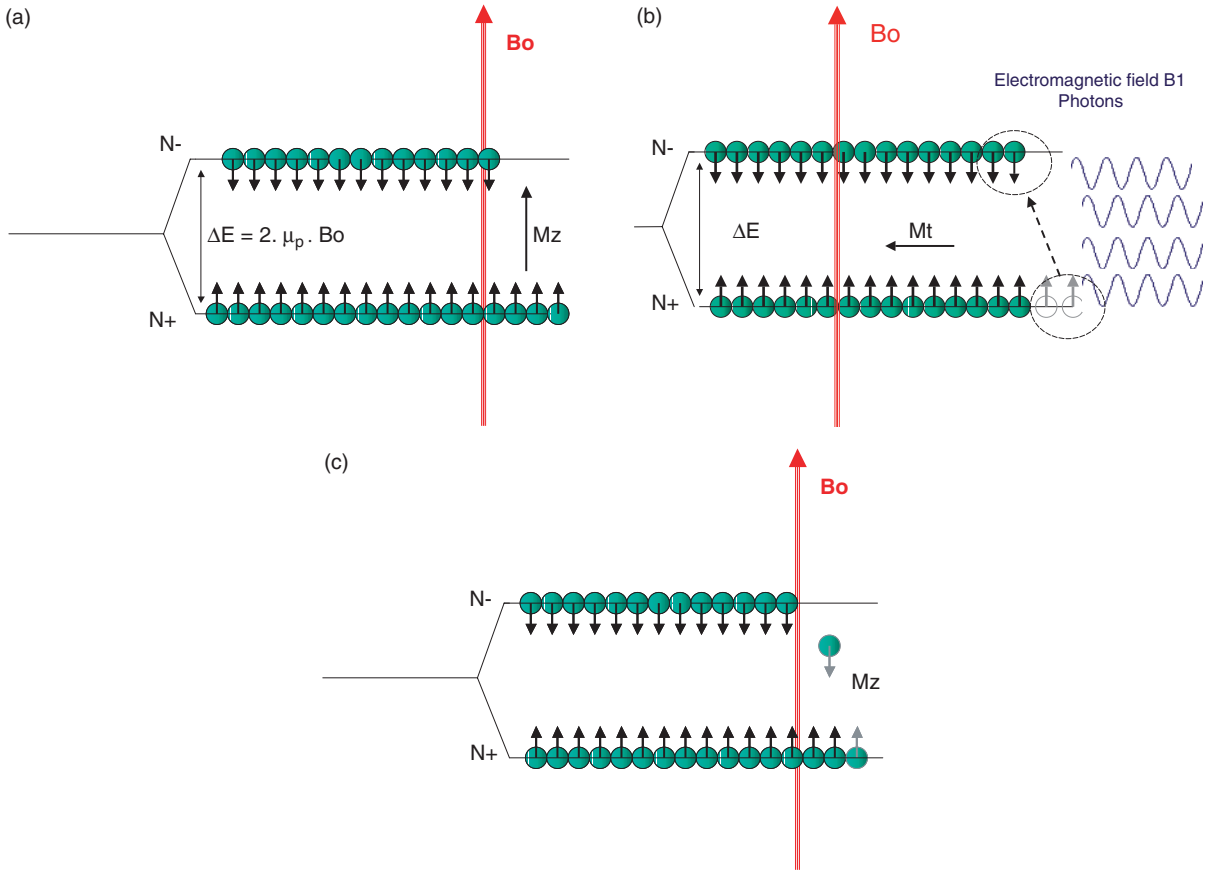

is calculated from the polarization P of nuclei that quantifies how much the magnetic moments are oriented by the magnetic field.

The polarization of nuclei by the magnetic field B_o, P is the ratio between the difference of populations of the two energy levels, $\Delta N = N^+ - N$, and the total population of nuclei, $N = N^+ + N^-$

$$P = \Delta N/N, \quad \text{so that } M_o = N\ P\mu/V. \tag{1.6}$$

At equilibrium, P depends on the ratio of the magnetic energy μBo (the source of magnetic order) to the thermal energy $k\ T$ (the source of disorder), where k is the Boltzman constant and T the temperature.

This ratio is very low in usual *in vivo* conditions. The polarization of hydrogen nuclei is equal to 3×10^{-6} at 1 T, at 300°K. We shall later see that the signal from nuclei is related to the polarization. A benefit of stronger magnetic field is the higher polarization of nuclear magnetic moments. Special

Figure 1.2.5 Nuclear magnetization precesses around the magnetic field.
(a) At equilibrium, all individual magnetic moments experience precession around B_o at the frequency F_o. The individual magnetic moments are distributed randomly across each cone. The upper cone (corresponding to the lower energy level) is more populated than the lower cone: there is a net longitudinal magnetization, $M_z=M_o$. The transverse components of the magnetic moments rotate; their rotations are not coherent, so that there is no net sum along the other directions. Then for the nuclear magnetization of the sample $M_x = M_y = 0$.
(b) When the absorption of photons from the RF field B_1 has equalized the populations of the two cones and has modified the transverse orientations of the magnetic moments, $M_z = 0$ and M_t gets a net value (M_x and $M_y \neq 0$)

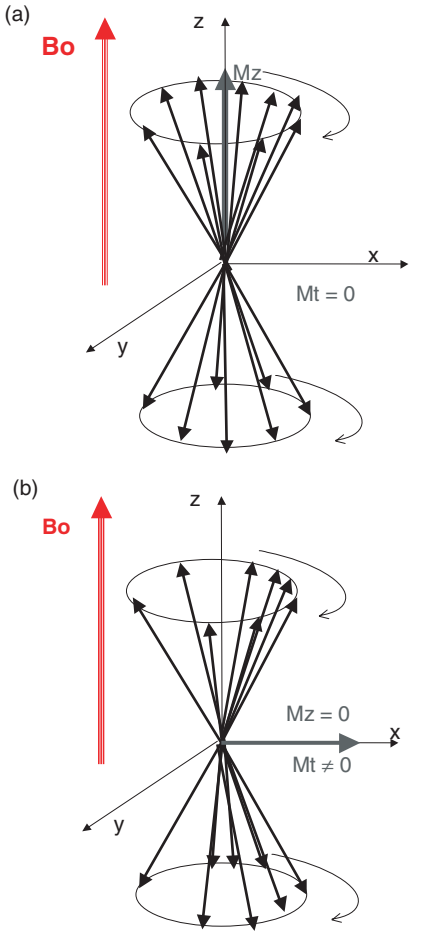

techniques allow to increase very strongly the polarization of nuclei such as Xenon, Helium and Hydrogen (see paragraph 1.10.1).

Let us come back to our small water sample and complete the description of magnetic moments.

At equilibrium, all the individual magnetic moments experience precession around B_o at the frequency F_o as displayed by Figure 1.2.2, but their transverse components are reparted randomly in the plane perpendicular to B_o and the sum of transverse components, M_t, is equal to zero (Figure 1.2.5(a)). After excitation of nuclear magnetic resonance, their transverse components are oriented in the plane perpendicular to B_o and the sum of transverse components, M_t, can be detected (Figure 1.2.5(b)).

1.3 Excitation and return to equilibrium of nuclear magnetization

Key points
Excitation of NMR is done by irradiation of the sample with a magnetic field oscillating at the resonance frequency F_o. This magnetic field tips the nuclear magnetization away from its initial orientation along B_o. While the transverse nuclear magnetization M_t rotates, it can be easily detected. The receiver probe picks the weak magnetic signal created by the rotation of M_t and generates a voltage oscillating at the frequency F_o. Detection can be done during a time limited by the decay of M_t, measured by the transverse relaxation time T2. One has to wait for the return to equilibrium of the longitudinal nuclear magnetization, during a time related to the longitudinal relaxation time $T1$, before repeating excitation and detection.

The magnetization at equilibrium, parallel to B_o, cannot be measured directly: Magnetic forces are small and difficult to measure. Conversely, when the global magnetization rotates around B_o at the resonance frequency, measurement of an electrical signal is possible.

Here we describe how to excite resonance, how to detect NMR signal, and the way nuclear magnetization returns to its initial equilibrium.

An oscillating or rotating physical phenomenon can be described by its amplitude, its frequency and its phase.

Both the RF magnetic field B_1 and the transverse magnetization M_t are vectors perpendicular to B_o that rotate or oscillate at the resonance frequency F_o (for definition of phase, see Figure 1.3.1).

At best, the field B_1 used for NMR excitation is a rotating field; however, the experiment is often driven

Figure 1.3.1 Oscillating/rotating vectors. The rotating vector M rotates in the plane XOY, as the needle of a clock; Ma, the amplitude of M is like the length of the needle. The angle of this vector with the reference axis OX is the phase ϕ. The rotation takes place at the frequency F (measured in turns per second or hertz). The phase at time zero is ϕ_o; later at time t the phase is written as

$$\phi = 2\,\pi\,F\,t + \phi_o. \tag{1.7}$$

The components of the vector M are

$$M_x = M_a \cos(\phi) = M_a \cos(2\,\pi\,Ft + \phi_o), \tag{1.8}$$
$$M_y = M_a \sin(\phi) = M_a \sin(2\,\pi\,Ft + \phi_o), \tag{1.9}$$

M_x is an oscillating quantity, also characterized by its amplitude M_a, its frequency of oscillation F and its phase at $t = 0$, ϕ_o

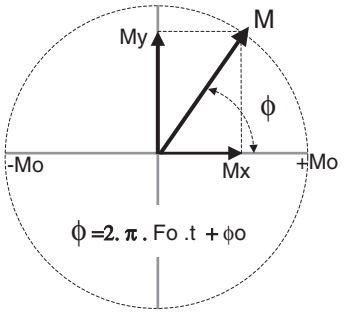

by a linear oscillating magnetic field that can be discomposed into two rotating fields: One of them rotates clockwise and the other counterclockwise. One of them is efficient to excite nuclear magnetic resonance and the other is not efficient.

The three characteristics of the transverse magnetization M_t are its amplitude, its precession frequency and its phase. They intervene in the generation of the NMR signal: The intensity of signal is proportional to the amplitude of the local magnetization, whereas the frequency and phase of the signal inform upon the spatial localization.

1.3.1 The excitation of nuclear magnetic resonance

To excite nuclear resonance means to set nuclear magnetization out of equilibrium by using *a second magnetic field*, the RF magnetic field $\vec{B_1}$ (RF means 'radio frequency'). This is done by irradiating the sample with an electromagnetic field rotating at the resonance frequency F_o. This field is created by sending current oscillating at the frequency F_o in a coil around the sample. (Note that this irradiation by an electromagnetic field is usually fully devoid of biological effects, except the thermal effects due to heating, because the energy of photons is more than 1×10^6 times smaller than any energy of ionisation: At the highest field used for MRI, 17.6 T, the photons of frequency 748 MHz have an energy equal to 3×10^{-6} eV. These photons can only heat tissues.)

The RF magnetic field $\vec{B_1}$ is perpendicular to $\vec{B_o}$ and rotates around the direction of $\vec{B_o}$. From the equivalence between electromagnetic field and photons, here again, there are two complementary descriptions of the excitation of resonance.

1.3.1.1 *In terms of energy levels and populations*

An electromagnetic wave of frequency F can also be described as made by photons of elementary energy

$E = h\,F$ (where h is the Planck's constant equal to 6.634×10^{-27} J.s).

The RF magnetic field $\vec{B_1}$ at the resonance frequency F_o is the magnetic component of an electromagnetic wave. The energy of the corresponding photons, equal to $h\,F_o$, is exactly equal to the difference between the magnetic energy of magnetic moments in the two energy levels, $\Delta E = 2\,\mu\,B_o$. Such photons convey exactly the energy needed to raise one magnetic moment from the lower level up to the higher level, whence the name of resonance frequency (Figure 1.2.4(b)).

When the two populations get equal, M_z is equal to zero and $M_t = M_o$. This is described geometrically as a 90° flip of the vector $\vec{M}$ that rotates around the direction of the RF field $\vec{B_1}$ (Figure 1.3.2).

The photons of the electromagnetic field at frequency F_o are fully polarized: This means that for every photon, the direction and phase of $\vec{B_1}$ is well defined and identical. When the photons are absorbed by the magnetic moments they give a well-defined value to the transverse component of the elementary magnetic moments, so that the transverse magnetization is no more equal to zero.

1.3.1.2 *In terms of vectors and forces*

The magnetic field $\vec{B_1}$ is perpendicular to $\vec{M}$ and exerts a force upon it. Under this force, the orientation of $\vec{M}$ is modified: $\vec{M}$ is tipped away the z axis.

Figure 1.3.2 Flip of the magnetization induced by the RF magnetic field B_1. The magnetic field B_1, perpendicular to the magnetization M and to B_o, exerts a torque upon M and modifies its direction. Since B_1 rotates around B_o at the same frequency F_o than does M, it keeps an adequate angle with M during the precession, and its action goes on during the rotation of M. Note that this drawing does not shows the fast rotation of M and B_1 at the frequency F_o: The observer is 'in the rotating frame' that rotates at the frequency F_o. Many of the following graphs are drawn with the same convention

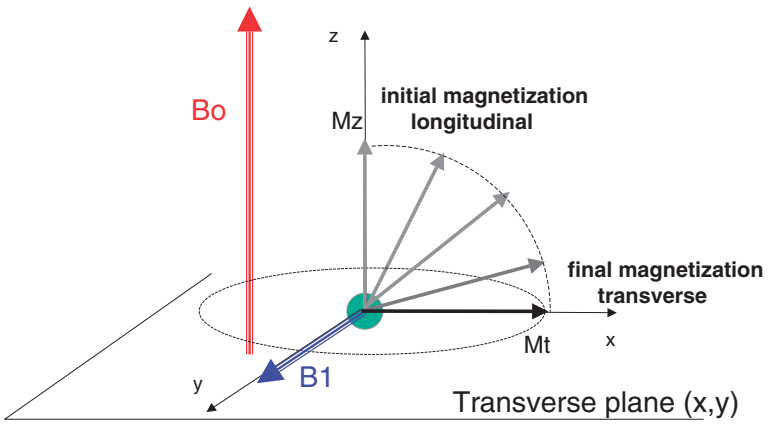

Both $\vec{M}$ and $\vec{B_1}$ rotate at the frequency F_o: The force exerted by $\vec{B_1}$ upon $\vec{M}$ also rotates, so that $\vec{M}$ goes on tipping away from z axis, and, while continuing its precession around $\vec{B_o}$, rotates around $\vec{B_1}$ (Figure 1.3.2).

The angulation of $\vec{M}$ relative to $\vec{B_o}$, induced by application of the RF field $\vec{B_1}$, is measured by the angle between the two vectors and is named as *the flip angle*. The magnitude of the flip angle depends on the amplitude of B_1 and the duration of its application τ, and also on the gyromagnetic factor γ, according to the relation

$$\alpha = \gamma B_1 \tau. \qquad (1.10)$$

When the flip angle reaches 90°, so that $\vec{M}$ is perpendicular to $\vec{B_o}$, the RF field $\vec{B_1}$ is shut down. Now the magnetization is fully 'transverse': The vector $\vec{M}$ lies in the plane x-y and rotates around $\vec{B_o}$ at the frequency F_o. The transverse component M_t is the largest possible at the end of a 90° flip: Then M_t is equal to the value of M_z before the application of $\vec{B_1}$ and $M_z = 0$.

The sample is ready for detection of the rotating transverse nuclear magnetization.

Usually B_1 is applied during a very short time, at high intensity: This is called a pulse of RF magnetic field. The RF pulse, which makes a 90° flip angle, is called a '*90° RF pulse*'.

Other trajectories are possible with a flip angle smaller than 90° (M_z is smaller but positive at the end of the RF pulse) or larger than 90° (M_z is negative at the end of the RF pulse).

More physics: the 180° RF pulse.
Initially, the nuclear magnetization is at equilibrium ($M_z = M_o$) corresponding to the difference ΔN between the populations N^+ and N^-. After irradiation by the RF field B_1 at the resonance frequency, when the number of photons absorbed by the nuclear magnetic moments is twice of that corresponding to a 90° pulse, the difference between populations N^+ and N^- is inverted: The upper level is more populated and the longitudinal magnetization has the value $-M_o$. Magnetization has been inverted; geometrically, this corresponds to a flip angle of 180° around the direction of B_1.

A 180° RF pulse is also applied in order to refocus the transverse magnetization and hence to generate a spin echo (see Section 1.3.4). Then its effect is to invert the component of M_t perpendicular to the RF field B_1 as shown in Figure 1.3.3(b).

1.3.2 How to detect the nuclear magnetization?

Nuclear magnetization can be detected while it rotates at a well-defined frequency after excitation. Voltage at the same frequency is induced in a receiver coil.

When a magnet bar rotates next to a loop of conducting wire, a voltage is induced and current flows in the loop. The simplest receiver coil is a loop of conductive wire designed to deliver a large voltage when it 'sees' a small magnetic field oscillating at the frequency F_o.

Let us consider a small sample containing water, in proximity to the receiver coil. After excitation of NMR

Figure 1.3.3 Signal induced in the receiver coil by the rotation of the transverse magnetization. The magnetization of the sample creates a small magnetic field b at vicinity. The flux of this field $\vec{b}$ through the receiver coil is modulated by the rotation of the transverse magnetization $\vec{M}_t$ of the sample at resonance. Thus, a voltage v is induced in the receiver coil. This voltage is the NMR signal. It is modulated at the frequency of rotation of magnetic moments, F_o. The decay of the transverse magnetization causes the NMR signal decay

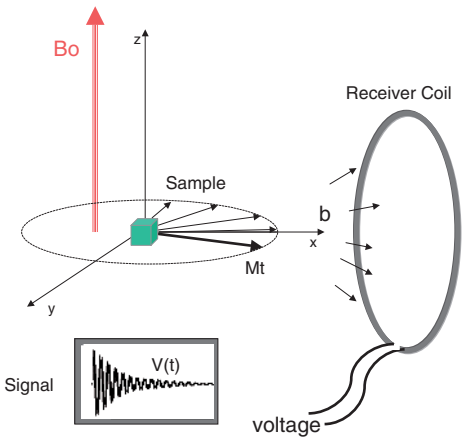

for hydrogen nuclei, the transverse magnetic moment M_t, the sum of hydrogen magnetic moments in the sample, rotates around B_o and creates a variable magnetic field $\vec{b}$ across the receiver coil as shown in Figure 1.3.4.

ψ is the flux of this magnetic field through the coil, written as the integral of the magnetic field $\vec{b}$ over the receiver coil surface. Faraday's law states that when the magnetic flux varies, a voltage v is induced in the coil, given by

$$v = -\mathrm{d}\psi/\mathrm{d}t. \qquad (1.11)$$

As M_t rotates with frequency F_o, the voltage v also oscillates at the frequency F_o. It is proportional to the magnetization M_t, M_t itself being proportional to M_o. From the derivation of the flux versus time, the voltage is proportional to the frequency F_o. (Remember that M_o and F_o are both proportional to B_o.)

The hydrogen magnetic moments in other adjacent samples also contribute to the total magnetic flux, and then to the total voltage V induced in the coil.

This voltage is named the free induction decay signal (FID) signal. The measurement of the FID signal is the simplest way to detect the nuclear magnetic resonance from nuclei in a sample.

1.3.3 The return to equilibrium of the nuclear magnetization

Key points

After excitation, the nuclear magnetization, set perpendicular to the external magnetic field, is out of equilibrium. Processes that bring back the nuclear magnetization to its equilibrium state take place. The recovery to equilibrium, named relaxation, is described by different evolutions for the longitudinal component M_z and the transverse component M_t of the vector magnetization M.

The longitudinal component M_z returns to its equilibrium M_o with the time constant $T1$, named the longitudinal relaxation time.

The transverse component M_t returns to its equilibrium value zero with the time constant $T2$, named the transverse relaxation time. Its decay is caused by the dephasing of magnetic moments due to the occurrence of different precession frequencies.

The local static inhomogeneity of magnetic field also contributes to the decay of M_t, often measured by the apparent relaxation time $T2^*$.

1.3.3.1 The longitudinal relaxation time T1

After emission of a 90° RF pulse at $t = 0$, the longitudinal component of magnetization, M_z, has been set to zero by the excitation, and M_z returns, or 'relaxes' towards its value M_o, by exchanging energy with its surrounding. Its evolution is described by

$$M_z = M_o[1 - \exp(-t/T1)], \qquad (1.12)$$

where $T1$, the longitudinal relaxation time, is the time constant characteristic of this exponential process of return to equilibrium. It depends on the probability of energy transfers between the nuclear magnetic moments and their environment, needed to rebuild the difference of population $N^+ - N^-$ at equilibrium as shown in Figure 1.2.4(c).

1.3.3.2 The transverse relaxation time T2

In a perfectly homogeneous magnetic field B_o, the transverse magnetization $\vec{M}_t$, while rotating in the plane perpendicular to $\vec{B}_o$, decays towards its equilibrium value which is zero. This decay is exponential:

Figure 1.3.4 The return to equilibrium of the longitudinal magnetization M_z. Curves are drawn for $T1$=2000 ms.
Full curve, M_z recovery starting from zero after excitation by a 90° RF pulse
M_z tends to its equilibrium value M_o according to Eq. (1.12). At $t=T1$, M_z/M_o=63%; at $t=3T1$, M_z/M_o=95%; at t=5, $T1$ M_z/M_o=99%.
Dotted curve, M_z recovery after inversion by a 180° RF pulse at t=0. The recovery of M_z, starting from the value $-M_o$, is written as

$$M_z = M_o[1 - 2\exp(-t/T1)]. \qquad (1.13)$$

At $t = 0.693\ T1$, $M_z = 0$. The span of variation of M_z is doubled during recovery. The inversion of M_z is used to generate images with higher $T1$ weighting or to suppress the signal of a given tissue as illustrated by Figure 1.7.2(b).

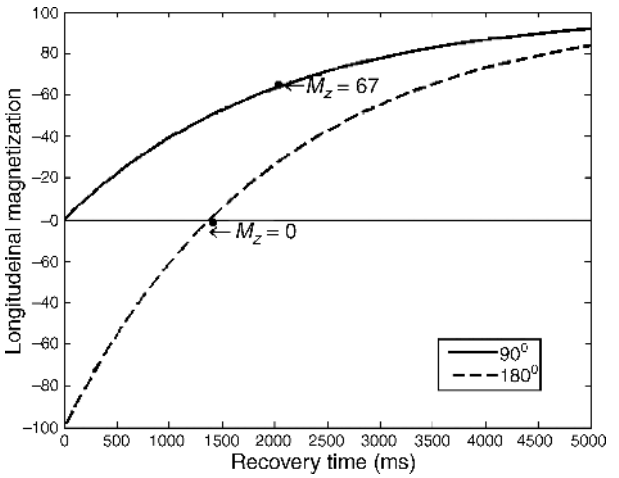

At time t after the creation of the transverse magnetization with amplitude M_{t0}, M_t is given by

$$M_t = M_{t0}\exp(-t/T2). \qquad (1.14)$$

The *transverse relaxation time* $T2$ is the time constant characteristic of this exponential decay.

The decay of the transverse magnetization occurs because each microscopic magnetic moment feels a local microscopic magnetic field created by the other nuclei at proximity, which is added to the external magnetic field $\vec{B}_o$. In a water sample, the thermal agitation of water molecules causes random fluctuations of this small magnetic field created by neighbouring nuclei and then causes small modifications of its resonance frequency. This mechanism spreads the microscopic vectors rotating around $\vec{B}_o$ as shown in Figure 1.3.5. The rotating transverse magnetizations of the nuclei are dephased. This causes the decay of transverse magnetization. The stronger these magnetic interactions between the neighbouring nuclei, the shorter is the relaxation time $T2$.

*1.3.3.3 The apparent relaxation time T2**

When the external magnetic field is not perfectly homogeneous in the volume of interest (the sample or the fraction of sample that constitutes a voxel), then the magnetic moments in this volume have slightly different resonance frequencies according to their location. If the spatial variation of the external magnetic field is larger than the fluctuating microscopic magnetic fields that cause the transverse relaxation, then in the volume of interest the transverse magnetizations are spread (or dephased) more efficiently and the resultant signal decreases more rapidly. This mechanism that accelerates the signal decrease is static: It can be reversed by the realization of a spin echo as seen in the following section.

The resulting apparent relaxation time is called $T2^*$. As seen further (as explained in paragraph 1.5.1), it is shorter inside tissues with heterogeneous structure and in proximity to magnetic agents enclosed in cells or blood vessels.

1.3.4 Dephasing and rephasing of the transverse magnetization: the spin echo

Key points
An echo is made by refocusing the transverse magnetization during its precession at a given time, the echo time. Some components of the transverse magnetization that underwent previous dephasing are rephrased; they add coherently to generate a larger signal. Dispersion of transverse magnetization is reduced at the time of the echo, where signal is maximal.

The spin echo can be used to measure the transverse relaxation time $T2$.

The spin echo can be compared to a race where some runners are faster and some slower (they have different velocities, i.e. precession frequencies). At time τ, they are ordered to start in the opposite direction. At time 2τ, runners arrive altogether at the starting point. Here the race is slightly different: The refocusing pulse does not invert the rotation of magnetization components, but puts them at modified positions on the track, with the same final result; all component have the same phase at the time 2τ (Figure 1.3.6).

The measurement of the transverse relaxation time $T2$ is done by acquisition of several echoes at different echo times, either by spectroscopic or by imaging experiments. The adjustment of these signals to an exponential model allows to determine $T2$.

Figure 1.3.5 The return to equilibrium of transverse magnetization. (a) After excitation, in the transverse plane, the small magnetic moments, the sum of which determines M_t, rotate at different frequencies and their phases become increasingly different: They are more and more dephased. In a very homogeneous magnetic field, the weak microscopic magnetic fields created by neighbouring magnetic moments at the level of one nucleus induce weak variation of the resonance frequency. The individual magnetizations are spread progressively while they rotate. The corresponding time constant is $T2$. (b) When the magnetic field is not homogeneous, the dephasing between individual magnetizations is faster. The corresponding time constant is $T2^*$, shorter than $T2$. (c) The decay of M_t during its precession is drawn for $T2 = 80$ ms in homogeneous field (full line) and for $T2^* = 20$ ms (dotted line). At $t = T2$ or $t = T2^*$, the ratio M_t/M_{t0} is equal to $e^{-1} = 0.367$

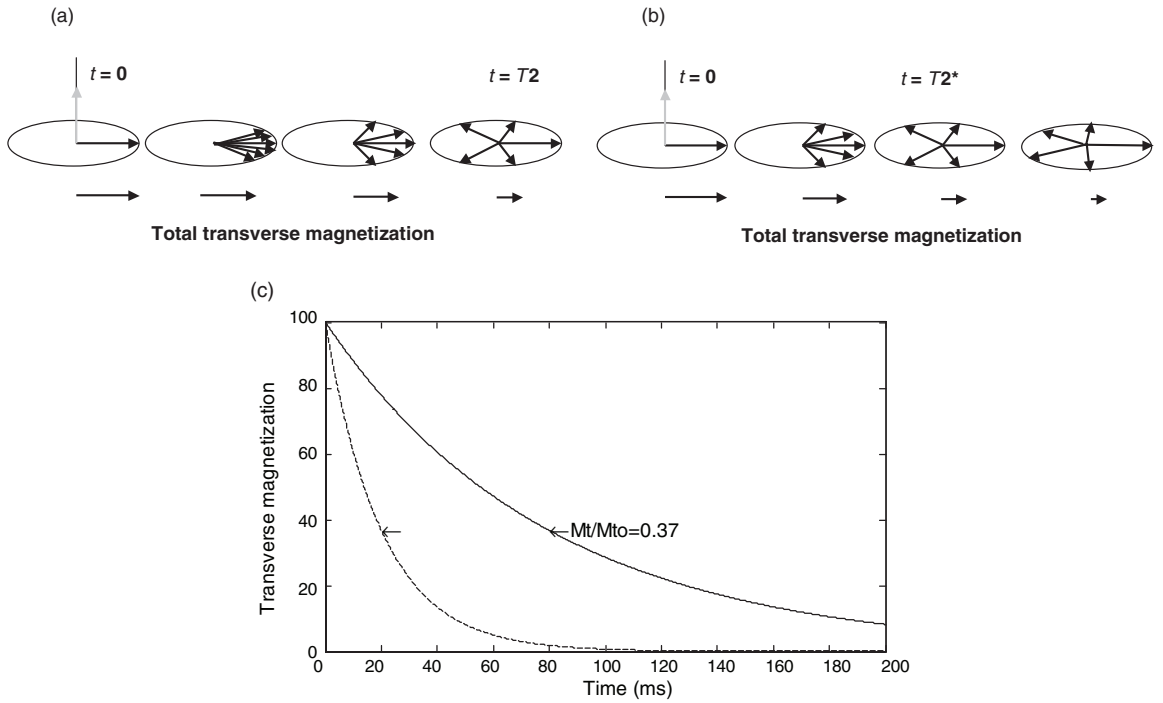

Figure 1.3.6 The spin echo. (a) The spin echo is done by applying a 180° pulse of the RF field B_1 at a given time τ between excitation and signal acquisition of the signal. At time 0, after the 90° RF pulse, the transverse magnetization is lined along OX and begins its rotation in the transverse plane. While it rotates, the spread of resonance frequencies causes quick dephasing of its components. At time τ, the RF field emitted along the y axis flips the magnetization components over the x-y plane, symmetrically to the axis OX. At time $TE=2\tau$, fast and slow rotating magnetizations are gathered and the signal goes through a maximum: This is the echo. (b) Variation of the NMR signal after excitation of resonance and through the echo. The FID takes place at beginning and decays with the time constant $T2^*$. The refocusing RF field is applied at 100 ms and the echo takes place at 200 ms. Before and after the centre of the echo at TE, the decay of signal on both sides of the echo depends on the shorter time $T2^*$

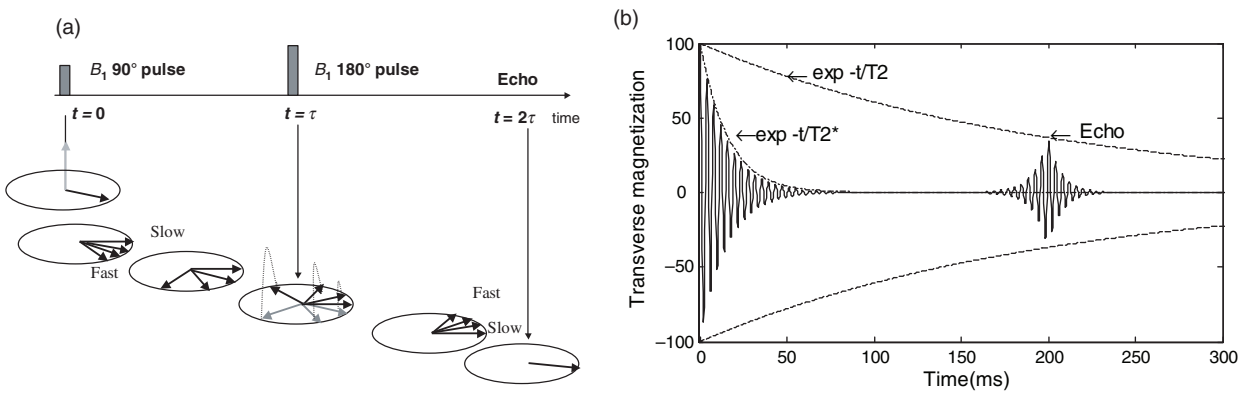

1.3.5 The global evolution of the vector nuclear magnetization

The two components of the nuclear magnetization have different kinetics of return to equilibrium (there is some quantum mechanics hidden behind). After excitation of resonance, the evolution of the magnetization M associates the fast precession of M at the frequency F_o around B_o, the slow increase of M_z along B_o and the faster decrease of the transverse component with the time constant $T2$ or $T2^*$. In most biological tissues $T2$ is much shorter than $T1$: The decay of M_t is much shorter that the recovery of M_z. Considering the handling and measurement of nuclear magnetization, we will go on to describe the evolutions of M_z and M_t as independent phenomena.

1.4 The NMR hardware: RF coils and gradient coils (more technology)

1.4.1 The probe (or RF coil)

A probe (also named as 'coil' because it is often built with coiled copper wire) is an electrical circuit built to emit a magnetic field oscillating at the resonance frequency F_o. The probe emits the 'radio-frequency field' B_1 used to excite nuclear magnetic resonance in the sample. It also receives the magnetic field created by the transverse nuclear magnetization during precession.

Each probe is built to excite or detect NMR at one given frequency (sometimes at two frequencies in order to detect two different nuclei).

The resonance frequency, proportional to B_o and depending on the nucleus observed, lies in the range 10–800 MHz; the frequency range for FM radio broadcasting and GSM telephony.

Probes are built with copper or silver wire or copper sheet to get high electrical conductivity, and with fixed or adjustable amagnetic capacitors.

They are resonating circuits adjusted for a sharp response with high current flowing at the resonance frequency. The current oscillating at the frequency F_o is injected in the circuit of adequate geometry, in order to create an intense magnetic field B_1 in the zone of interest. Homogeneity of B_1 over the zone of interest is useful, but not always obtained.

At the beginning of experiments, the probe response is optimised, usually by trimming adjustable capacitors, to emit maximal B_1 at a given power and at the required frequency. Power of the amplifier that delivers current at the frequency F_o is in the range 100 W–10 kW depending on coils and magnet size.

A probe also is the device used to receive the resonance signal from the sample, at the same resonance frequency. Then homogeneity is a less stringent need, and very small coils at immediate vicinity of the region of interest may offer better sensitivity for detection.

Often probes are used for emission and reception (then named transceivers probes). Some probes are used for B_1 emission only: They are named transmitter probes. Other probes, usually smaller, are used for signal reception: They are receiver probes, positioned in proximity to the organ under examination, around it or at its surface (then named surface coils).

A way to increase sensitivity and spatial extent of measurements is to combine multiple surface coils by building an array of coils around the object under study. Then it is possible to increase the speed of acquisition by parallel imaging (paragraph 6.8.3)

1.4.2 The two simplest RF coil geometries

The surface coil is often built as a circular loop of copper wire. When it is fed with current oscillating at frequency F_o, it generates a magnetic field B_1 also oscillating. The field B_1 has a complex topography across space, except at proximity of the coil centre, as shown in Figure 1.1.2. The quick variation of B_1 amplitude can be used as a tool to select a restricted volume where NMR excitation is done. The surface coil is often built as a circular loop, yielding optimal sensitivity in proximity to the coil centre, within a distance comparable to the coil radius.

The cylindrical coil offer good homogeneity of the RF field B_1 created inside; it is very convenient to house a rat or a mouse inside the cylindrical tunnel of the magnet. The field B_1 is created by several parallel wires (at least four wires are needed); it is homogeneous in the central zone of the structure. The saddle coil, the discrete cosine coil and the birdcage coil are cylindrical coils (Mispelter, Lupu and Briguet, 2006). They can be used for B_1 emission and signal reception, or for B_1 emission only while using a smaller receiver coil.

The efficiency of the coil, as an emitter or a receiver, is higher when the coil is small and is near the region of interest. Increasing the receiver coil efficiency directly increases the signal to the noise of

Figure 1.4.1 RF probes for small animal imaging. (a) Surface coil built to resonate at phosphorus frequency for rat leg muscle spectroscopy. (b) Cylindrical coil for rat half body examination, built according to the discrete cosine geometry (Bolinger, Prammer and Leigh, 1988) (*courtesy of C. Wary, Laboratoire de RMN, Institut de Myologie (AFM-CEA), Paris*)

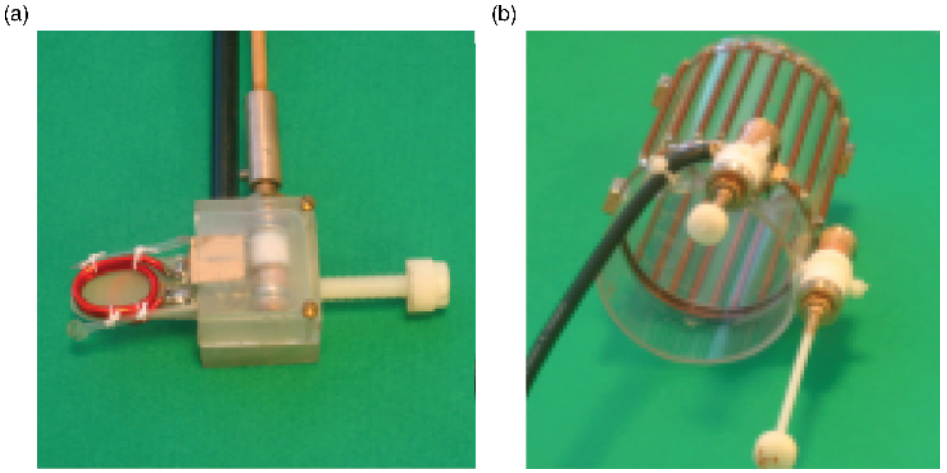

measurements. That is the reason why most labs involved in small animal imaging build their own coils, in order to optimise each experiment as illustrated by Figure 1.4.1. The way to build one's own coils is explained with much practical detail in (Mispelter, Lupu and Briguet, 2006).

1.4.3 The gradient coils

The NMR imaging system includes three distinct gradient coil sets. Each gradient coil set is built in order to create an additional magnetic field parallel to B_o and varying along one axis, either the x-axis or the y-axis or the z-axis as illustrated in Figure 1.4.2. The geometry of the other coils is schematized in Ness Aiver (1997) or Webb (2003).

In presence of this additional field, the proton resonance frequencies vary as a function of location. This makes possible either to select in the sample a slice where NMR excitation takes place or to read a NMR signal with frequencies reflecting the object structure: Spatial encoding of signal is performed.

Each gradient coil set is fed with current during the time interval when signal labelling along the corresponding axis is performed. Strong gradient intensity, obtained by high current flowing in the gradient coil, is needed to obtain high spatial resolution of the sample image.

While current flows in a gradient coil, the force exerted by the magnetic field B_o on the wire where current flows induces vibrations of the winding and its support: This is the cause of the strong acoustic noise during MRI acquisitions, though the gradient coils are firmly fixed along the inner wall of the magnet bore.

The magnetic field from one gradient coil set is risen at the needed value in a fraction of millisecond, the rise time. The rise time of magnetic field gradient is an important characteristic of the hardware: If this time is long, milliseconds are lost while current goes

Figure 1.4.2 The z-gradient coil. The z-gradient coil is made of two (or four) symmetric coils, fed with opposite currents. It creates an additional magnetic field ΔB parallel to B_o, which is proportional to z. At the centre of the magnet ($z = 0$), ΔB is equal to zero. For z positive (resp. negative), ΔB is positive (resp. negative). In the central zone, ΔB does not vary with x and y coordinates and varies linearly with z: $\Delta B = Gz \cdot z$

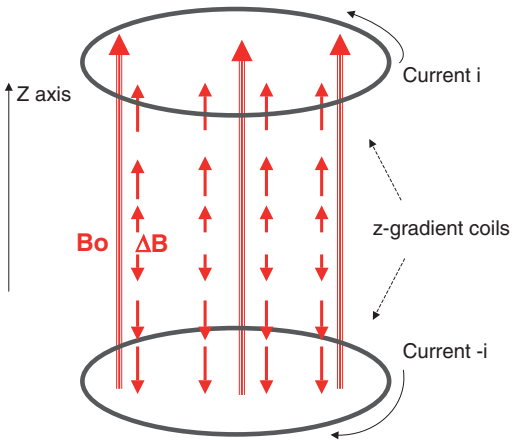

Figure 1.4.3 The three magnetic fields needed for MRI measurements. A mouse is laid upon a surface coil at the centre of the magnet bore. The main magnetic field B_o created by the magnet is directed along z and the additional magnetic field ΔB (the amplitude of which here varies along z) is parallel to B_o. The RF field B_1 is perpendicular to B_o. The mouse is scaled up.

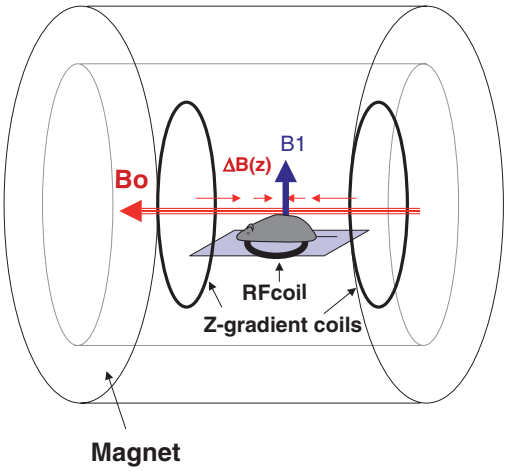

up or down in the gradient coils, and this limits the ability to perform fast imaging.

Gradient strength and gradient rise time are limiting factors for acquisitions with high spatial or temporal resolution. It is easier to obtain high gradient in small gradient coils built for small animals imaging than in larger gradient coils built for medical imaging; typical figures are gradient intensity equal to 200 mT/m and rise time equal to 100 µs, for current intensity peaking at 100 A and voltage at 150 V.

Figure 1.4.3 shows the set of different coils that create B_o, the additional magnetic field varying along $z$axis and the RF magnetic field.

1.5 NMR spectroscopy: the chemical encoding

In vitro NMR spectroscopy, a powerful analytical technique, allows identification and quantification of molecules in a test tube and is widely used to study the structure and dynamics of complex molecules.

In vivo NMR spectroscopy is not so efficient, due to the complexity and the heterogeneity of living systems and less optimal instrumental conditions (lower magnetic field, larger volumes and shorter acquisition times). Its sensitivity is low: Roughly, only metabolites at concentrations above 1 mM can be detected *in vivo*. However, NMR spectroscopy may distinguish several metabolites of a same nucleus that would not be separated by nuclear imaging techniques (PET or SPECT) since their scheme of disintegration is the same. It has then been applied to many physiological studies. An important characteristic of NMR techniques is the possibility to obtain successively or sequentially spectra and images encoding different parameters.

The nuclei ^{31}P, ^{1}H, ^{13}C provide most *in vivo* applications of NMR spectroscopy (Gadian, 1995).

1.5.1 NMR signal and NMR spectrum

Key points
The NMR signal registered during the acquisition time is transformed into a spectrum, which displays the different resonance frequencies of the nuclei present in the sample. As the frequency of resonance of a nucleus depends on its chemical environment, the nuclei in different molecules give rise to different peaks, more or less separated. When no spatial encoding is done, the NMR spectrum reflects the chemical composition of the sample under study. The surface of each peak is proportional to the number of molecules contributing to the peak. High magnetic field homogeneity allows obtaining narrower and higher resonance peaks.

What is a spectrum? The notion of spectrum is familiar: A drop of water, or a prism made with glass, spreads the different coloured components of white light, so that the spectrum of light is made visible. A spectrum is the display of components, at different frequencies, which contribute to a physical phenomenon such as light or sound, or, here, the NMR signal.

When the magnetic moments in the sample resonate at different frequencies (this means that they feel different values of magnetic field, a point explained later), the spectrum of its NMR signal displays these different components as peaks at each frequency. The mathematical operation that gives the spectrum of a NMR signal is the Fourier transform. This operation done by a computer can be compared to the capacity of our ears and brain to identify distinct musical notes played simultaneously.

Molecules can be detected and identified when the corresponding spectral peak is sharp, this being

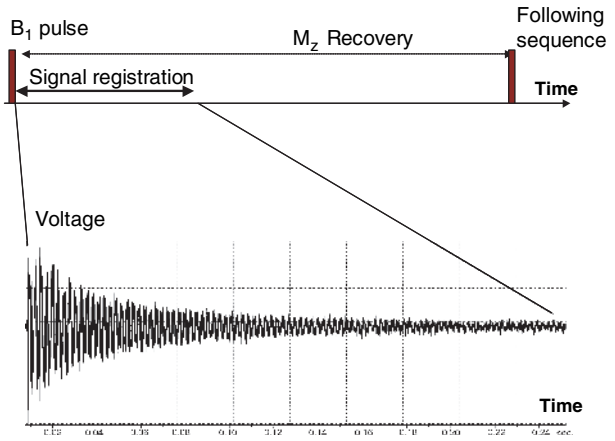

Figure 1.5.1 Spectroscopy sequence and NMR signal. Sequence of measurement showing the excitation by the RF B_1 pulse, the signal registration during the read-out time and the waiting time for recovery of M_z, named the repetition time T_R. The signal results from the addition of several components with different amplitudes, frequencies and decay times. It is digitised at low frequency after demodulation at a frequency $\approx F_o$

related to a long enough relaxation time $T2$; macromolecules that have fast transverse relaxation yield broad peaks that cannot be observed easily.

When the sample contains several kinds of molecules bearing the nucleus under study (most frequent *in vivo*!), the NMR spectrum of this nucleus contains several peaks. If the peaks have sufficient intensity and are well separated, these molecules can be identified and their respective concentrations in the tissue can be measured from the peak areas in the spectrum. Also if a molecule contains several times the observed nucleus, as the three phosphorus nuclei of the ATP molecule, this molecule has several resonance frequencies more or less separated.

When large samples, such as part of living organisms, are examined, the selection of a volume contributing to the spectrum can be done by using a small surface coil that registers signal from its proximity. Also it is possible to select a volume by using the imaging technique named selective irradiation (paragraph 6.1). Figure 1.5.1 shows how to register the NMR signal.

How to obtain a NMR spectrum?

The aim of the experiment is the excitation of resonance for one nucleus contained in several molecular species that have different resonance frequencies around the value $F_o = \gamma/2\pi\, B_o$. Typically, the acquisition is done after emission of the RF field B_1 at the resonance frequency F_o as an intense pulse of short duration (less than 1 ms). This pulse of duration τ excites the resonance frequencies in the interval $\delta F = 1/\tau$ around the frequency F_o, and then nuclei of several molecules with slightly different frequencies can be excited and detected.

The voltage induced in the receiver probe by the precession of magnetization is named the free induction decay signal (FID). It is collected immediately after the emission of the RF field B_1, during the precession of the transverse magnetization, without the additional manipulations needed to build an image. It decays exponentially with a time constant $T2$ or $T2^*$ and is registered as long as possible up to having decreased at the level of the electronic noise.

When the elementary signal is too weak, as is often the case for nuclei with low gyromagnetic factor γ, or molecules at weak concentration, several signals are accumulated, while one has to wait for the repetition time T_R between successive measurements in order to recover longitudinal magnetization M_z.

After amplification, filtering and numerisation, the signal is transformed into a spectrum by a mathematical calculation, the Fourier Transform. The spectrum displays the frequential content of the signal around the frequency F_o.

1.5.2 More physics: the width and height of a resonance peak

The NMR signal is proportional to the number of hydrogen nuclei excited by the RF B_1 pulse and detected by the receiver coil. After Fourier transform, the surface of each peak is proportional to the corresponding number of nuclei. One can estimate simply this surface by the product of height and width of the peak.

When the magnetic field is perfectly homogeneous, the spectrum of the peak corresponding to a given molecule (here for example water) is related to the corresponding transverse relaxation time $T2$. The longer the $T2$, that is the weaker the magnetic interactions between the magnetic moment of the nucleus detected and the neighbouring magnetic moments, the narrower is this peak. The line-width (defined as the full width of the peak at half height) is written as

$$\delta F_o = 1/\pi T2. \qquad (1.15)$$

When the local value of the magnetic field varies inside the sample, the decay of transverse magnetization is faster. During the rotation of the transverse magnetization, the magnetic moments that feel slightly different values of the external magnetic field B_o rotate at different frequencies, and then their sum quickly decreases.

In first approximation the signal decay can be described as exponential, with a time constant analogous to $T2$. The apparent relaxation time that describes the decay of transverse magnetization $T2^*$ is written as

$$1/T2^* = 1/T2 + \pi\gamma\delta B_o, \qquad (1.16)$$

where δB_o is the range of variation of B_o through the sample.

The spectral width of the peak is then

$$\delta F_o = 1/\pi T2^*. \qquad (1.17)$$

It depends on the intrinsic value of $T2$ and on the extrinsic parameter δB_o. It is then important to obtain high magnetic field homogeneity in the zone under study in order to get minimal spectral width and maximal peak height as illustrated in Figure 1.5.2. By sending current in dedicated windings, it is possible to improve the magnetic field homogeneity through the sample. This operation named 'shimming' is needed to obtain high quality spectra. It is performed either manually or automatically with dedicated software.

1.5.3 More physics: Why do nuclei in the different molecules give rise to different peaks in the NMR spectrum?

In addition to the external magnetic field, each nucleus inside a molecule feels a magnetic field created by neighbouring electrons, which depends on chemical bonds between the atom and its neighbours. This additional magnetic field $\vec{B}_{el}$, which originates from

Figure 1.5.2 NMR FID signal and spectrum. (a) FID signal plotted at the relative precession frequency $F - F_o = 50$ Hz, with decay time $T2 = 100$ ms. (b) Spectrum, the peak line width measured at half-height is $\delta f = 3.3$ Hz. (c) FID signal at same relative precession frequency $F - F_o = 50$ Hz, with shorter decay time $T2^* = 50$ ms. (d) Spectrum, the peak area is unchanged, its width is doubled and its height is halved

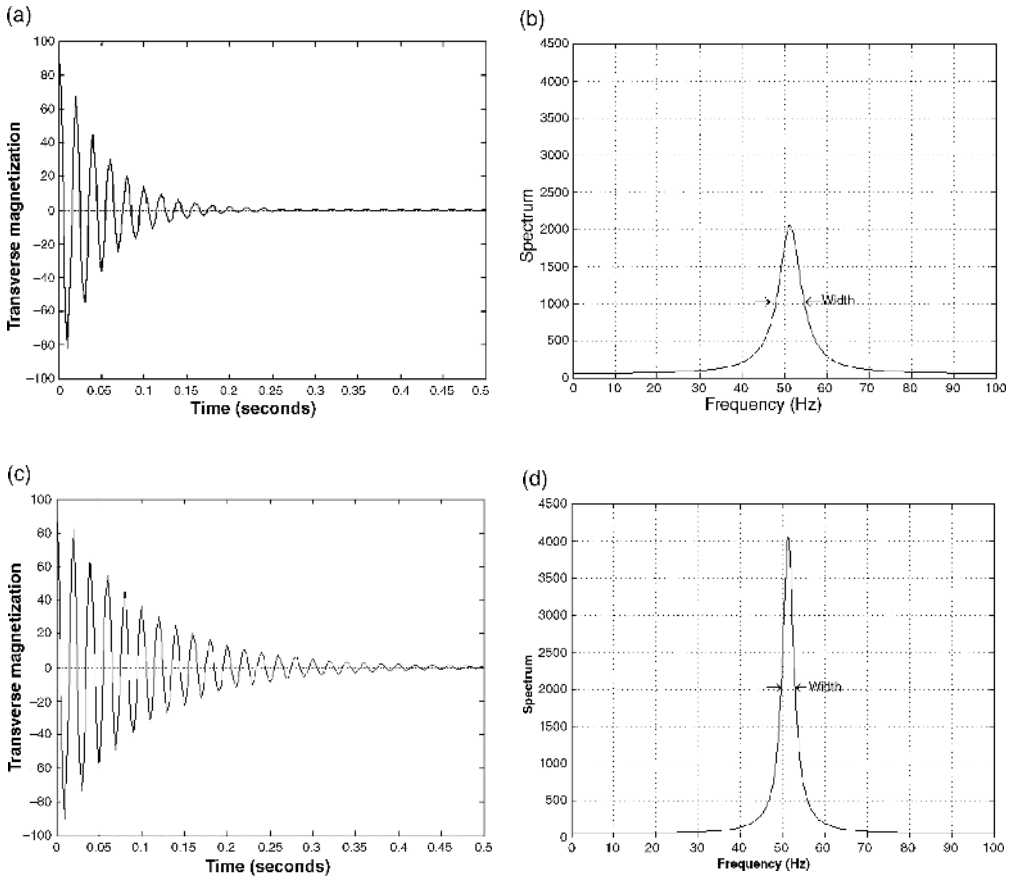

the magnetic polarization of the electrons, is proportional to the external magnetic field B_o.

The frequency of resonance is calculated as a function of this additional magnetic field of neighbouring electrons, written as

$$\vec{B_{el}} = -\sigma.\vec{B_o}. \quad (1.18)$$

Then the resonance frequency is written as

$$F = \gamma/2\pi.(B_o + B_{el}) = \gamma/2\pi.(1-\sigma).B_o, \quad (1.19)$$

$$F = F_o.(1\ \sigma), \quad (1.20)$$

where σ is the chemical shift of the resonance frequency, independent of B_o value, and usually given in parts per million (ppm).

Each type of chemical bond corresponds to a value of σ: For example in the ATP molecules the three phosphorus nuclei have different resonance frequencies.

Spectra are displayed along a relative frequency scale calibrated in ppm ($1\,\text{ppm} = 10^{-6}$).

$$\delta = (F - F_o)/F_o, \quad (1.21)$$

where δ is the displacement of the resonance frequency F relative to the reference frequency F_o.

Using this relative scale, the position of the peaks is independent of the magnetic field intensity, even though they are better separated at higher field, the reason why spectroscopic measurements are done at high magnetic field.

1.5.4 Phosphorus spectroscopy

The phosphorus nucleus ^{31}P is almost 100% naturally abundant and resonates at a frequency around 40% of that of hydrogen. From its lower gyromagnetic factor, its signal is then less intense (see Table 1.2.1); also different RF coils are used for phosphorus spectroscopy and hydrogen imaging.

Phosphorus spectroscopy gives access to the detection of the high-energy phosphorylated metabolites ATP and phosphocreatine (PCr), of the phosphate ion (Pi), and of phosphomonoesters and phosphodiesters. These compounds have intracellular concentrations in the range 1–30 mM. Their relative amounts at rest give an insight into the metabolic status of an organ. The dynamic follow-up of their *in vivo* concentrations can be performed non-invasively with a temporal resolution of a few seconds. The metabolism of organs such as skeletal muscle, myocardium, kidney, brain, and liver can be studied under normal conditions of temperature and pH, at rest and under stimulation. Phosphorus spectroscopy is widely used to perform *in vivo* fully atraumatic biochemical studies (Gadian, 1995).

The surface of each peak in the spectrum of a sample is proportional to the number of molecules of the corresponding metabolites in the sample, but it also depends on their relaxation times, $T1$ and $T2$, and on instrumental factors. This makes the absolute quantification of metabolite concentration difficult. It is easier to follow-up the variation of concentration of a molecule, by measuring the ratio of its peak area to that of a reference compound.

The ratio of phosphocreatine (PCr) peak to the sum of all phosphorylated metabolite peaks is widely used as an index to monitor variations of phosphocreatine concentration in skeletal muscle during exercise and recovery. As oxidative phosphorylations take place in mitochondriae, NMR phosphorus spectroscopy is an important tool for *in vivo* quantification of mitochondrial energy production (Balaban, 1984).

Figure 1.5.3 Phosphorus spectrum of rat leg muscle at rest. Acquisition is done at 4T by using a small 15 mm diameter surface coil. The spectrum exhibits five well-separated peaks: The peak of phosphorus in phosphocreatine (PCr) is the highest. The three phosphorus nuclei in the molecule of ATP are detected at different resonance frequencies located at −2.7 ppm, −7.5 ppm and −16 ppm from the PCr peak. The peak of the phosphorus nuclei of the phosphate ion is located at 4.8 ppm from the PCr peak, corresponding to muscle pH = 7. Another smaller and broader peak at 6.5 ppm is that of phosphorus from phosphomonoesters, mostly sugar phosphates (*courtesy of P. Carlier, Laboratoire de RMN, Institut de Myologie (AFM-CEA), Paris*)

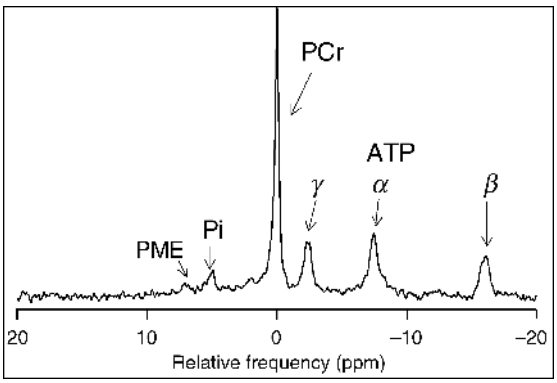

Figure 1.5.4 Rat brain hydrogen spectrum. Acquisition is done at 9.4 T with a spin-echo sequence (TR = 3500 ms, TE = 8 ms). The selection of a small cubic volume located in basal ganglia, with dimensions 3 × 3 × 3 mm is done, is based upon anatomical images by selective irradiation (PRESS sequence). The large water signal is suppressed prior to the acquisition of smaller signals from other less concentrated molecules. From the much weaker concentration of these molecules, the signal of corresponding peaks is low, so that 512 signals are averaged to improve the quality of the spectrum, and the acquisition time is 30 min. The largest peak, at 3 ppm, is that of the methyl protons of NAA. The second highest peak is that of the methyl protons of creatine and phosphocreatine, labelled Cr + PCr. The peak of myo-inositol (Ins) at 4.05 ppm corresponds to a concentration about 5 mM (*courtesy of Bruker SA, Ettlingen Germany*)

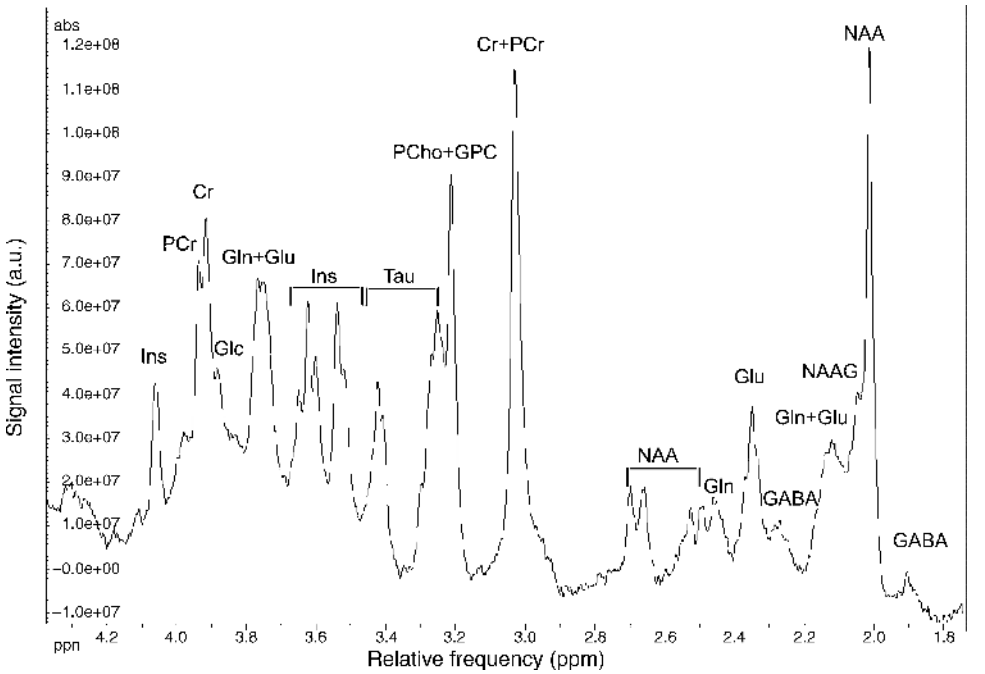

NMR phosphorus spectroscopy allows the measurement of pH in a living system without any perturbation. Phosphate is mostly intracellular, and the resonance frequency of the phosphate ion peak is sensitive to pH. Atraumatic and precise pH measurements are done by measuring the interval between Pi and PCr peaks. The intracellular pH is related to the concentrations of the $H_2PO_4^-$ and HPO_4^- ions and to the dissociation constant of phosphoric acid ($pK_a = 6.75$). The resonance frequencies of the two phosphoric ions differ by 2.42 ppm. In water, the inter-conversion between the two phosphoric ions is so fast that their peaks are collapsed into one single peak, the frequency of which reflects the proportion of the two forms and thus the pH. The relation that links the pH to the interval between Pi and PCr peaks, δ (in ppm), established by Moon and Richards (1973), is then

$$\mathrm{pH} = 6.75 + \log((\delta - 3.27)/(5.69 - \delta)). \quad (1.22)$$

Figure 1.5.3 shows a typical spectrum of rat leg muscle at rest.

1.5.5 Hydrogen spectroscopy

NMR hydrogen spectroscopy benefits from the highest sensitivity and from the value of the hydrogen gyromagnetic factor. However, the range of hydrogen chemical shifts for biological compounds is narrower, and the large signals of water and fat hide the signals of the less abundant metabolites. Also the number of molecules that contain hydrogen is huge, and spectra are often obscured by the multiplicity of superimposed peaks. Only a limited number of peaks are identified easily for biological studies. Most applications of hydrogen spectroscopy concern brain studies (Gadian, 1995). As brain is a complex and heterogeneous organ, brain studies require to combine precise localization and spectroscopic analysis. A volume is

selected by using the selective irradiation, and then its NMR signal is read without magnetic field gradient. As water is at concentration circa 80 M in brain, the huge water signal that would obscure smaller signals has to be suppressed. The large peak of *N*-acetylaspartate (NAA) is a marker of neurons in mature brain. Creatine and choline peaks are also easily detected. The peak of lactate is a marker of brain metabolic disorders. Figure 1.5.4 shows a typical spectrum of rat brain.

1.5.6 Spectroscopic imaging

Magnetic resonance spectroscopy and imaging are combined into spectroscopic imaging, also named chemical shift imaging (CSI), where spectra are obtained for each voxel in the plane or the volume of interest (Gadian, 1995). Several operations of phase encoding (see paragraph 6.3) are performed along two or three spatial directions, similarly to 3D imaging (paragraph 6.7), before reading a signal in the absence of magnetic field gradient. Acquisition times can be very long unless sophisticated fast acquisition techniques are applied. Spectroscopic imaging is mostly applied to brain studies, where a precise localization of biochemical abnormalities is needed.

1.6 How to build NMR images: the spatial encoding

Key points

In order to build images of hydrogen magnetization, the magnetic field in the magnet is made to vary linearly along one axis, so that the resonance frequencies in the sample are labelled according to the location of nuclei along that axis. Three operations allow to build images:

The selective irradiation around a precise resonance frequency, done in presence of the first magnetic field gradient, excites only the magnetic moments located inside a slice perpendicular to this axis, at a selected position.

After excitation of resonance inside this slice, the second, phase-encoding, magnetic field gradient is installed and the precession of magnetization begins; its frequency is a function of the position of nuclei along the second gradient axis. At the end of this step of preparation, the magnetic moments in the selected slice have an initial phase labelled along the second coordinate axis.

Then the signal of nuclei in the slice is acquired in presence of the third, frequency-encoding, magnetic field gradient and the resonance frequency is labelled along the other coordinate axis.

The contributions of all voxels in the slice are registered altogether.The Fourier transform separates the different frequencies contained in the signal, spread by the frequency-encoding gradient. It also separates the phases of the different voxels prepared by the application of the phase-encoding gradient.

To localize the origin of NMR hydrogen signals, the basic operation consists into spreading the resonance frequencies by application of a non-homogeneous magnetic field B that is the sum of B_o and an additional field varying linearly along one direction through the object, for example

$$B = B_o + \Delta B = B_o + G_x\, x.$$

Then a linear relation between the resonance frequency and the position along one direction is created, because the resonance frequency of nuclei at x is

$$F = F_o + \gamma/2\pi.G_x.\, x.$$

What is a gradient?

A gradient is the variation through space, along one direction, of a physical parameter: A gradient of temperature or pressure, or magnetic field. Here the amplitude of the external magnetic field (not its direction, the magnetic field is always lined along z) is modified, so that the resonance frequency of hydrogen nuclei is modified correspondingly.

The magnetic field gradient along the x axis is $G_x = dB/dx$.

This additional magnetic field is made by sending current in a dedicated winding; here it is the x-gradient coil (see paragraph 4.3). However, if the magnetic field delivered by the main magnet is not homogeneous, some magnetic field gradients are present permanently, a source for image distortions.

Practically, three gradients along the x-, y- and z-axis are applied successively in order to label each point of an object and to build 2D or 3D images of this object. For 2D imaging, several slices are selected and measured successively, and a stack of images, each mapping a given slice, is reconstructed throughout a volume inside the object. For 3D imaging, a volume is selected and measured, and then slices of arbitrary orientation are reconstructed and displayed.

The three operations are described below with more details, in the case of axial slices (perpendicular to the axis z which is the direction of B_o), with the phase-encoding gradient along OY and the frequency-encoding gradient along OX. Then Figure 1.6.3 will display the three successive operations. Any other slice orientation (perpendicular to another axis, or oblique) is obtained easily by permutation of axis or by combination of several magnetic field gradients: A sagittal slice is obtained if selective irradiation is done using the gradient G_x.

1.6.1 The slice selection by selective irradiation

The slice selection relies upon excitation by the RF field $\vec{B}_1$ and simultaneous application of a magnetic field gradient.

The additional field $\Delta\vec{B} = \vec{G}_z.\, z$, created by current flowing in the z-gradient coil, is lighted on immediately before and during the application of the RF field at the frequency $F1$, as shown in Figure 1.6.1.

Figure 1.6.1 Slice selection with a gradient of magnetic field B along the z-axis. The two symmetrical z gradient coils create an additional magnetic field $\Delta B = G_z.\, z$, lined along B_o and proportional to z in a zone at centre of the magnet. During application of the gradient G_z, the resonance frequency at z is

$$F(z) = \gamma/2\pi.(B_o + \Delta B) = F_o + \gamma/2\pi.G_z.z.$$

The RF field $B1$ is applied at the precise frequency $F1$, so that resonance is excited only in the slice around $z1$: Only the magnetic moments in this slice are set in transverse orientation, while those out of the slice are not modified

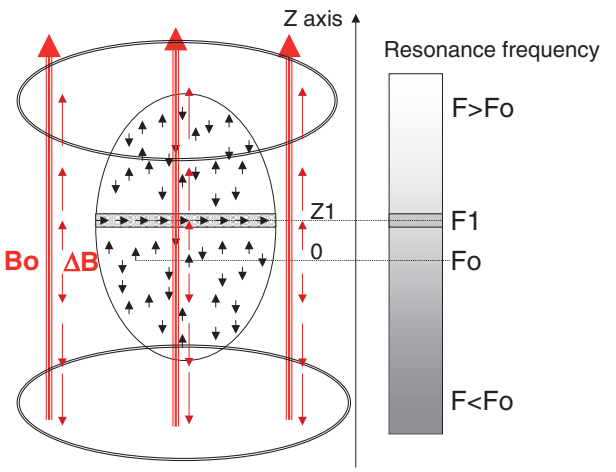

The magnetic field is

$$\vec{B} = \vec{B_o} + \Delta\vec{B} = \vec{B_o} + \vec{G}_z.z. \qquad (1.23)$$

Then the nuclei located at the level z resonate at the frequency

$$F(z) = \gamma/2\pi.(B_o + \Delta B) = F_o + \gamma/2\pi.G_z. \qquad (1.24)$$

At $z1$, the resonance frequency is

$$F1 = F_o + \gamma/2\pi.G_z.z1. \qquad (1.25)$$

The magnetization in the slice at $z1$, which resonates around the frequency $F1$, is excited by the RF field $B1$ and is driven to the transverse plane. Other slices of the object also see the field $B1$ but their magnetization is not modified by this RF field that oscillates at a 'wrong' frequency.

This operation is named the selective irradiation.

Afterwards, the magnetic moments of nuclei inside the selected slice begin precession, and their signal can be registered.

More technology: selectivity of a RF pulse

The RF magnetic field is efficient through a narrow and well-defined frequency interval if it is applied with a carefully modulated shape during a rather long duration; this is a 'selective pulse'. Conversely, to excite a broad spectrum a short and intense pulse of RF magnetic field (a hard pulse) is efficient.

Note that in the spin-echo imaging sequence described further, the 180° refocusing pulse used to refocus the transverse magnetization is also selective and then it is applied in presence of a magnetic field gradient, so that only the moments in the excited slice are refocused, and those out of the slice do not feel the 180° RF field pulse.

It is also possible, before excitation, when the magnetization is longitudinal, to invert it inside a slice by a selective RF pulse giving a flip angle equal to 180°, as is done for the inversion-recovery sequence (as illustrated by Figure 1.7.2(b)).

The selection of a volume can be performed by selective irradiation of a slice along the three orthogonal directions, successively (for example one 90° pulse for excitation, and two successive refocusing 180° pulses). The signal read after this sequence comes from the cube at the intersection of the three orthogonal planes. This is the basis of single voxel brain spectroscopy where the signal of a small volume selected inside brain is measured, after localization from scout images.

Figure 1.6.2 (a) Signal acquisition and frequency encoding along the *x* axis. The frequency-encoding gradient is applied during the detection of the NMR signal of the whole slice selected. The magnetization of one elementary volume around the abscissae x resonates at the frequency

$$F = F_o + \gamma/2\pi.Gx.x.$$

The signals of all elementary volumes add altogether; Fourier transform allows to assign their specific contributions along the *x* axis in the spectrum.
(b) Signal preparation and phase encoding along the *x* axis. The phase-encoding gradient is applied during the preparation time T_P. The magnetization of one elementary volume around the coordinate *y* rotates in the transverse plane at the frequency

$$F = F_o + \gamma/2\pi.Gy.y$$

and its phase after the time TP depends on *y*.
The second step of 2D Fourier transform allows to assign each phase to the position along *y* axis

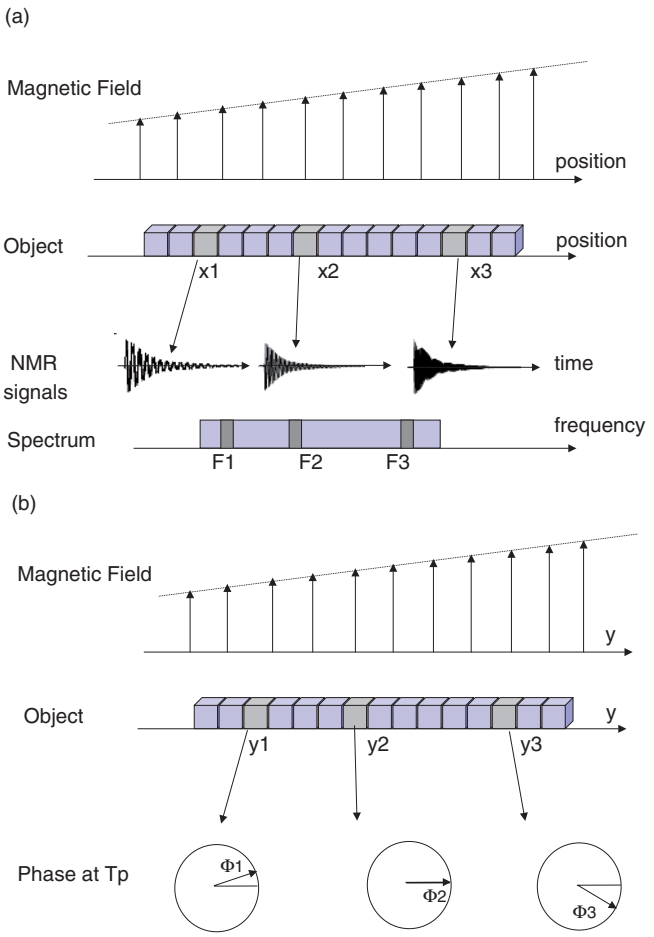

1.6.2 The signal acquisition with frequency encoding

During this operation, the resonance frequency is linearly related to the position of nuclei along the *x* axis. The additional field parallel to B_o and varying with *x* is as follows: $\Delta\vec{B} = \vec{G}_x.\, x$.

It is applied by setting current in the *x*-gradient coils, during the precession of transverse magnetization, as shown by Figure 1.6.2(a).

The resonance frequency is then

$$F = \gamma/2\pi.(B_o + \Delta B) = F_o + \gamma/2\pi.G_x.x. \quad (1.26)$$

Around the position $x1$, inside a volume of width δx delimited inside the selected slice, the hydrogen nuclei resonate around the frequency

$$F1 = F_o + \gamma/2\pi.G_x.x1 \quad (1.27)$$

in the interval

$$\delta F = \gamma/2\pi.G_x.\delta x. \tag{1.28}$$

The NMR signal registered comes from all magnetic moments in the slice; it is the sum of signals of magnetic moments at different abscissae and then at different frequencies.

From this signal the Fourier transform yields a spectrum. In this spectrum, the selection of the interval $\delta F = \gamma/2\pi.\ G_x.\ \delta x$ around $F1$ allows to estimate the signal which originates from this rod around the abscissa $x1$.

The spectrum of the total signal is a one-dimensional image of the object.

1.6.3 The signal preparation by phase encoding

The position in the plane along the other axis, here y, is encoded by another operation, the phase encoding, done after slice selection and immediately before reading the signal. Between these two operations, immediately after the extinction of the RF field $B1$, the gradient G_y along y is applied during the preparation time Tp (a few milliseconds) in order to modify the frequency of precession. At the end of Tp the gradient G_y is shut down, the gradient G_x is lighted on and the signal acquisition begins. The magnetic moments keep the memory of their precession during T_p, which took place at a frequency depending on y and on the value of the gradient G_y. They have rotated in the transverse plane, during T_p, by an angle ϕ depending on their coordinate y (Figure 1.6.2(b)).

F is related to y according to

$$F = F_o + \gamma/2\pi.G_y.y. \tag{1.29}$$

The phase of a magnetic moment with frequency F starting from $\phi = 0$ at $t = 0$, at time T_p is

$$\phi = 2\pi.F.T_p. \tag{1.30}$$

It is related to the position of nuclei along the y axis by:

$$\phi = 2\pi.F_o.T_p + \gamma.T_p.G_y.y. \tag{1.31}$$

Figure 1.6.3 Succession of the three operations that allow spatial labeling of the NMR signal. Slice selection is done by selective excitation of resonance at the frequency $F1$, that is the resonance frequency in the slice at $z1$ in presence of the magnetic field gradient G_z. Phase encoding is done by application of the magnetic field gradient G_y during the preparation time T_p. Then the phase of M_t in the transverse plane at the time T_p depends on the coordinate y. Frequency encoding is done by application of the magnetic field gradient G_x during the signal acquisition. Then the frequency of precession of M_t in the transverse plane during the signal acquisition depends on the coordinate x

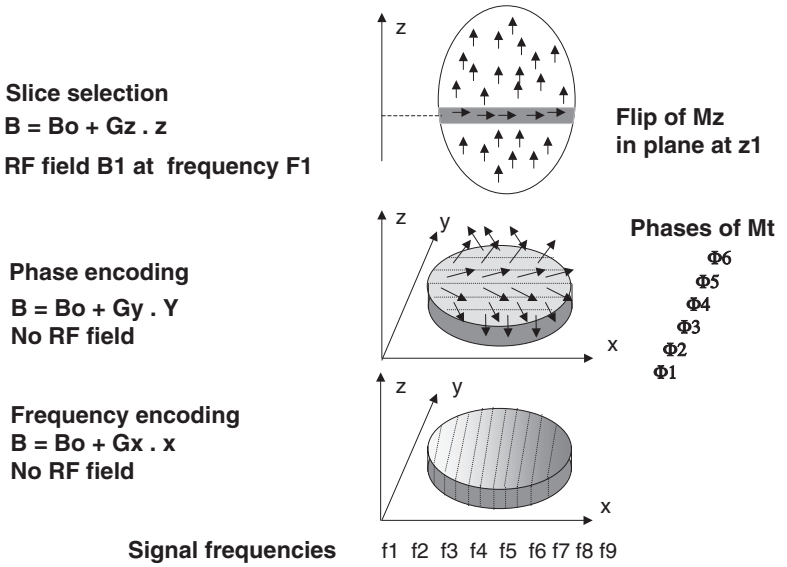

The first term of the phase is the same for all magnetic moments in the slice; the second term varies linearly according their position y.

The phase encoding operation is repeated N_y times, before each signal acquisition, in order to obtain N_y signals, encoded with increasing values of the gradient G_y at each successive step. Each signal acquisition is separated from the previous one by the time interval T_R.

This waiting time T_R is needed for the recovery of M_z before the next excitation and acquisition of the following signal.

1.6.3.1 *The phase artefacts: a specific feature of MRI*

The motions of organs such as heart, lungs and digestive structures often are not synchronized with the phase encoding. This is the source of some image degradation, because phase encoding gives information upon the localization along the y axis at times separated by the interval T_R (the repetition time), not synchronized with physiologic motion. If the localization of a given structure is not stable at the time of encoding, artefacts (often ghost-like images of the moving structures) degrade the image quality as illustrated in Figure 1.6.4. It is possible to reduce these artefacts by synchronizing the NMR acquisition with the motion (for example by triggering acquisition with an electrocardiographic signal to perform heart imaging).

Figure 1.6.4 Phase artefacts. Coronal image through the thorax and abdomen of an anaesthetised mouse, done at 1.5 T with a spin-echo sequence, T_R 600 ms, T_E 18 ms, acquisition time 4 min 15 s. The read gradient is applied along the head-tail direction and the phase encoding gradient along the left-right direction. The respiratory motions induce ghost-like images of organs in the direction of phase encoding, more visible for high intensity structures such as stomach and kidneys

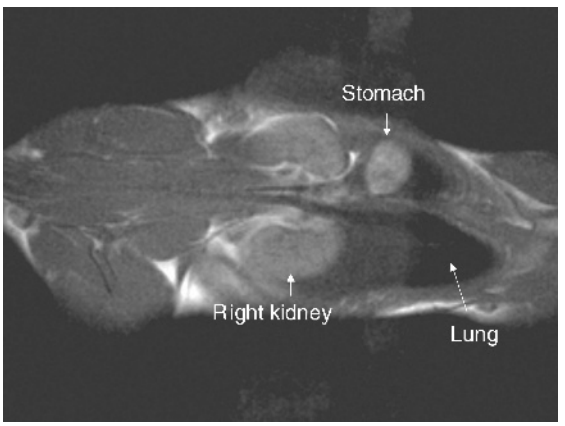

1.6.4 How to increase the amplitude of the NMR signal: the echo

Key points

An echo is made by refocusing the transverse magnetization during its precession at a given time, the echo time. The different components of transverse magnetization contained in one voxel, which were dephased, add more coherently so that their sum generates a larger signal. At the time of the echo the signal goes through a maximum. The value of this maximum is limited by the intrinsic decay of transverse magnetization, expressed by the transverse relaxation time, $T2$ or $T2^*$.

The spin echo efficiently decreases the dephasing caused by the local static magnetic field inhomogeneity and by the read gradient; the spin-echo signal at echo time T_E decreases as $\exp(-T_E/T2)$.

The gradient echo only removes the dephasing by the read gradient; the gradient-echo signal at echo time T_E decreases as $\exp(-T_E/T2^*)$.

The formation of an echo increases signal intensity and then image quality.

The acquisition of each NMR signal is delayed by the time needed for phase encoding. Magnetic field gradients, either resulting from the local inhomogeneity of the static magnetic field or applied for frequency or phase encoding operations, contribute to faster signal decay during the precession. This loss of signal can be partly recovered by the realisation of an echo. The echo is a signal that evolves through a maximum when the dephasing of its components is counterbalanced at a precise time, the echo time (as an opened fan that is closed).

The spin echo is done, as explained in paragraph 1.3.4, and Figure 1.3.6, by applying a 180° pulse of the RF field $B1$ at mid-time between the excitation and the centre of the signal acquisition. At time 0, the transverse magnetization begins its rotation in the transverse plane. While it rotates, the spread of resonance frequencies causes quick dephasing of its components. At time τ, the RF field flips the magnetization over the x-y plane, symmetrically to the axis OX. At

time $T_E = 2\tau$, fast and slow rotating magnetizations are gathered: the signal goes through a maximum at the echo time T_E.

The signal acquisition is done on both sides of the echo.

The frequency-encoding gradient, which is an important source of magnetic inhomogeneity, is applied symmetrically before and after the refocusing pulse. The 'spontaneous' static field gradients from the magnet or from the object structure are applied permanently, and then they are also symmetrical with regard to the refocusing pulse. *Note that the dephasing induced by the phase-encoding gradient must not be refocused: The corresponding information would be lost.*

At T_E the decay of the signal is governed by the transverse relaxation time, and the signal is proportional to

$$M_t(T_E) = M_t(0).e^{-T_E/T2}. \quad (1.33)$$

When the homogeneity of local magnetic field is low, the acquisition of spin echoes greatly enhances the quality of images; however, the refocusing RF pulse takes some time and delays the signal acquisition.

With spectroscopy or imaging techniques, several successive echoes can be generated at times T_{E1}, T_{E2}, T_{E3}, ... This is used to measure $T2$ by sampling the decay of M_t along time and adjusting data to an exponential model.

The gradient echo is done by applying successively two intensities of the frequency-encoding magnetic field gradient, with opposite signs. The first gradient causes quick dephasing of the magnetic moments that have precession frequencies depending on their positions according to the corresponding direction; in presence of the second gradient the magnetic moment that had the higher precession frequency now have the lower one and vice versa. This allows a refocusing of magnetic moments located at different positions along the gradient axis, and then allows to measure a larger signal at time TE. This refocusing compensates 'only' for the dispersion of phases induced by this gradient, not for the other mechanisms of dephasing.

According to the local inhomogeneity of the magnetic field from other sources than this frequency encoding gradient, the transverse magnetization M_t decays with the time constant $T2^* < T2$, and the signal at the echo time T_E is proportional to

$$M_t(T_E) = M_t(0).e^{-T_E/T2^*}. \quad (1.34)$$

The echo time can be made very short because no refocusing RF pulse is applied. Short echo times are needed to perform fast acquisition with short repetition time T_R.

When a small structure inside the object is a local source of magnetic inhomogeneity, $T2^*$ is shortened locally, and at a given echo time T_E the signal around this structure is weakened. This is used to detect local magnetic structures, such as capillaries filled by deoxyhemoglobin in red blood cells, or cells magnetically labelled with iron. Conversely the magnetic inhomogeneity caused by large structures such as the interface between air-filled lungs and heart also shorten $T2^*$ through large zones and decrease image quality (Figure. 1.6.5(c)).

1.6.5 Duration and chronogram of image acquisition

Since N_y phase encoding operations are needed, the basic acquisition lasts for a time equal to $N_y T_R$. Adding several identical measurements in order to improve image quality can be needed. Then the acquisition time is multiplicated by N_a.

In conventional 'spin-echo' sequences, the repetition time T_R is in the range 0.1–3 s and acquisition lasts a few minutes. Gradient-echo sequences with shorter T_R values are widely used to reduce acquisition time to seconds. Still faster modalities are available (see Sections 1.6.8. and 1.7.2.).

Usually several slices are measured during one acquisition as shown in Figure 1.6.6(b), sparing a lot of time: Nuclei in all slices are detected sequentially by repeating successively selective irradiation and signal registration for each slice.

1.6.6 Image reconstruction and image matrix

Image reconstruction is done via a 2D Fourier transform (FT) that transforms the information contained in the frequency and the phase of signals into an information related to the location in the plane (x, y) of proton magnetization. As a comparison, when listening to the orchestra playing, the conductor can identify the sounds from different musical instruments played at the same time and can also detect that one given instrument played a note with a small temporal lag (its phase).

For each slice, N_y signals have been measured. Each signal, after numerisation, is made of N_x values. All the signals that have been measured are recombined

Figure 1.6.5 (a) **The spin-echo**: The frequency encoding gradient is applied symmetrically before and after the 180° RF pulse (applied at time τ). Faster and slower rotating magnetizations have their phases inverted by the 180° RF pulse, and then are rephased at the echo time $TE = 2.\tau$, where the signal is maximal.
(b) **The gradient-echo**: The frequency encoding gradient is applied with successive opposite polarities to obtain the gradient echo at TE. The precession is faster for magnetic moments at $x2 > x1$ when the magnetic field gradient is positive, slower when it is negative. Inverting the gradient creates a rephasing of magnetic moments and then an echo.
(c) **Images of a lemon done with a spin-echo sequences**. $TR = 1000$ ms, $TE = 14$ ms. Flip angle value is 90°, the acquisition time 512 s.
(d) **Images of a lemon done with a gradient-echo sequences**. $TR = 100$ ms, $TE = 9$ ms. Flip angle value is 25°, the acquisition time is 51 s. The two images are done with the same geometrical data and slice location but differ by their acquisition time and by the signal-to-noise ratio. The gradient-echo is done ten times faster, at the optimum flip angle as explained in paragraph 1.7.2.1. The two images also differ by the magnetic artifacts, clearly visible on the gradient-echo image. Magnetic inhomogeneities, induced by the small difference in local magnetic field between the water of lemon pulp and the denser tissue of fibrous borders, or between lemon structures and air, have high visibility in the gradient-echo image. The central region is filled with air that yields no MNR signal (no protons!) and also has a magnetization different from that of water. Then, from local shortening of T2*, the signal of water is destroyed at the border of the zone filled with air. This artifact is strongly reduced in the spin-echo image.

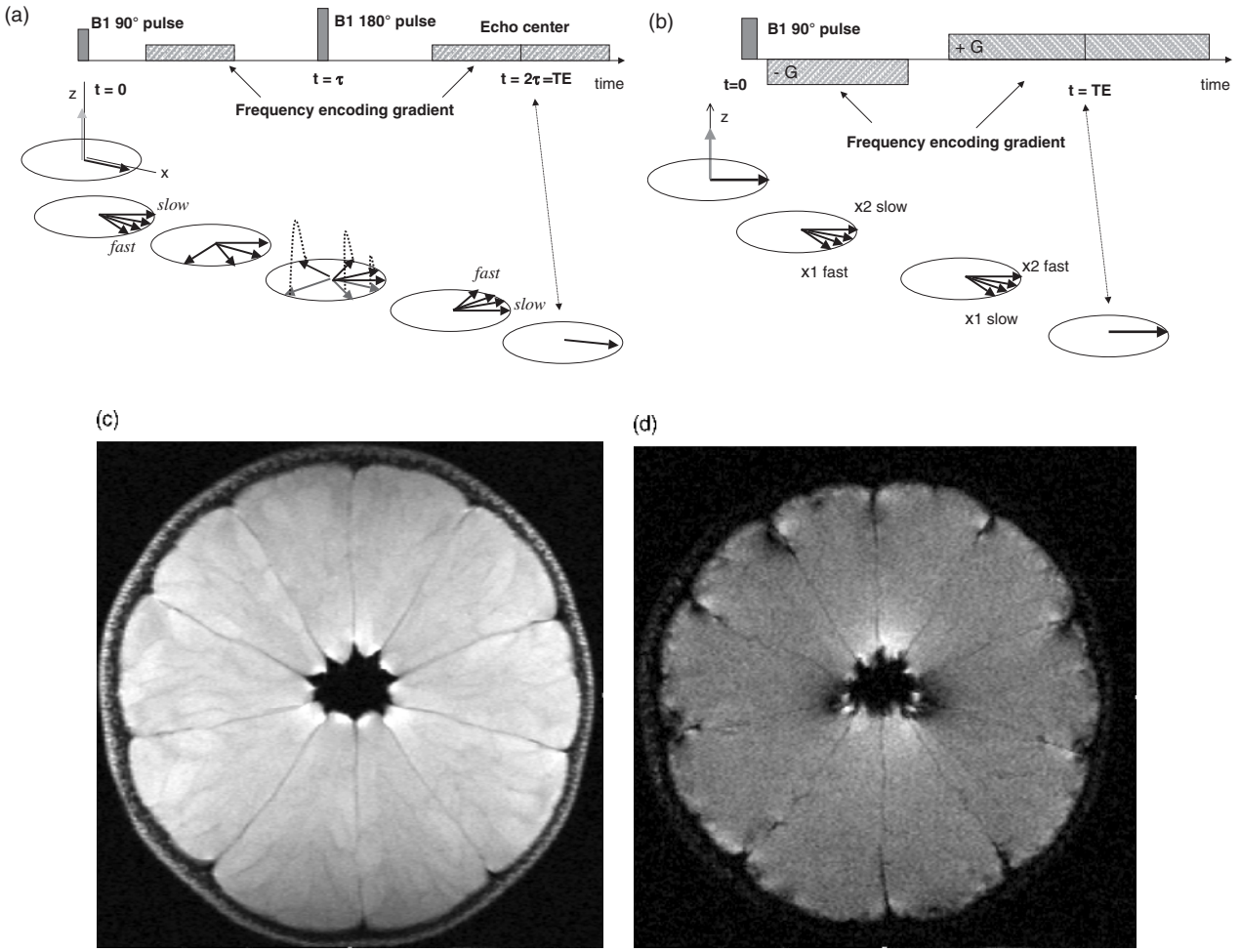

Figure 1.6.6 More technology Chronograms of MRI acquisition sequences. Each line of a chronogram shows a distinct physical operation. (a) Gradient-echo sequence. At $t = 0$, the RF $B1$ pulse is emitted and the slice selection gradient is applied to select the first slice. Then the phase encoding gradient is applied: here, 16 successive values of the gradient are drawn, the 10th value is applied. Simultaneously, the predephasing read gradient is applied. Then the signal of the slice is read before and after the centre of the gradient-echo at the time T_E. N_x signal values are registered during this read time. The longitudinal magnetization is let to recover during the repetition time T_R and then the following sequence is performed.
(b) Multislice gradient-echo sequence. The operations described for slice 1 are done consecutively for the other slices during the time T_R, while the magnetization in each slice returns to equilibrium after its own excitation. After excitation of the first slice, phase encoding and signal acquisition, the z gradient is lighted on again, RF field $B1$ is applied at the second frequency $F2$, the second slice at $z2$ is selected and so on. During the following T_R interval, the gradient G_y is increased and the same operations are performed, here again beginning with the first slice. Each of the N slices is then excited at intervals equal to T_R. At end of acquisition the sequence has been repeated N_y times. For each slice, N_y signals are registered successively, with N_y stepwise increasing values of the signal phase, obtained by stepwise increasing the value of the encoding phase gradient G_y.
(c) Spin-echo sequence. Slice selection and phase encoding are done in a similar way. The refocusing 180° pulse is applied at $T_E/2$ in order to rephase selectively the magnetic moments in the slice (this needs a selective RF impulsion applied in presence of the gradient G_z). The frequency-encoding gradient is applied symmetrically on each side of the refocusiong 180° pulse, and the echo is obtained at T_E.
(d) 3D gradient-echo sequence. The RF $B1$ pulse is applied without a selection gradient to flip magnetization of all the volume. Two phase-encoding gradients are applied. Here, each of them varies across 16 steps; the 9th step along the first axis, and the 4th step along the second axis are being applied. 16×16 phase-encoding steps will be done

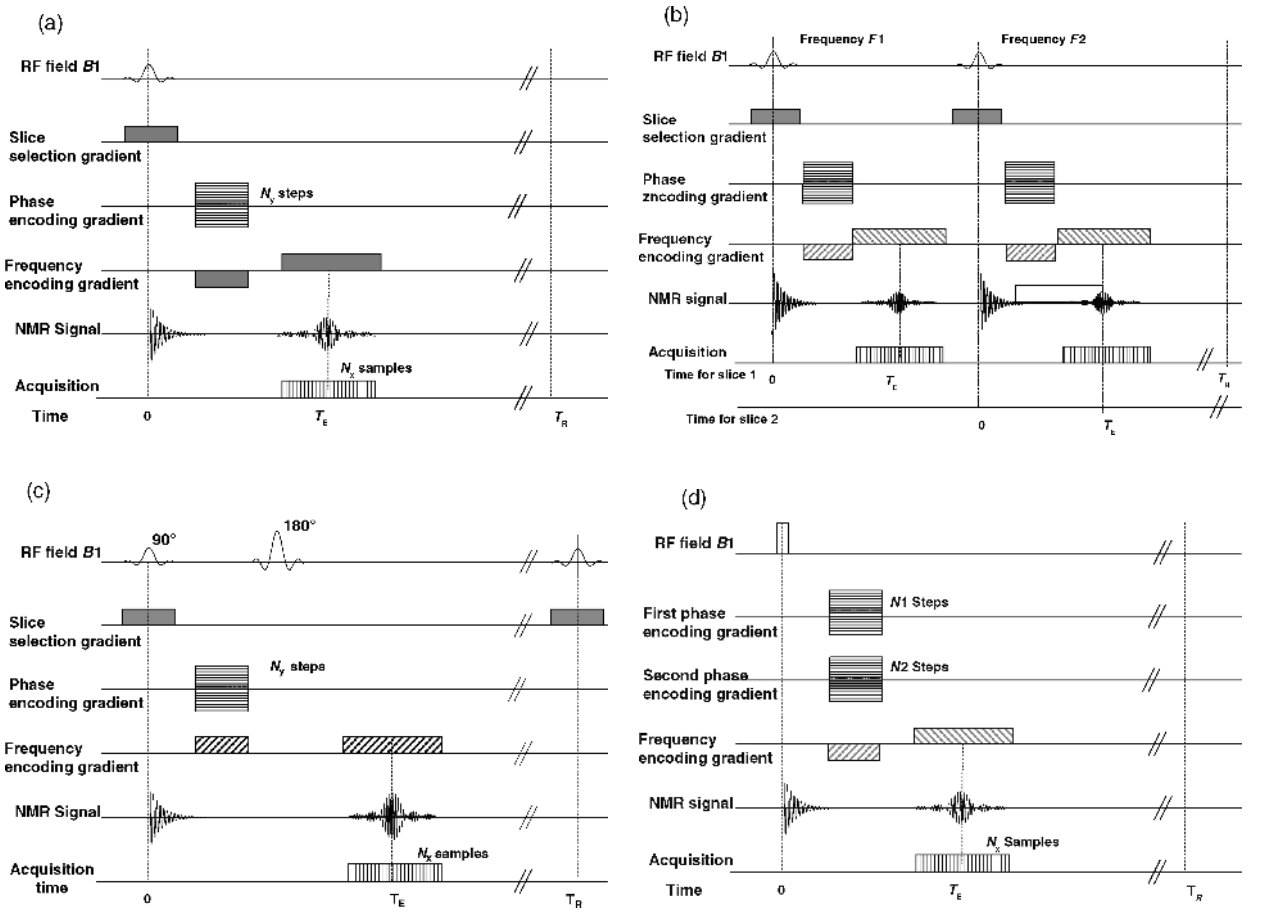

by the Fourier transform to calculate the magnetization of a given pixel of the image.

The matrix of the image is N_x and N_y: This means that $N_x.N_y$ voxels are identified, each giving rise to a signal, and that the corresponding image will be made of $N_x.N_y$ corresponding pixels.

The first Fourier transform gives the spectra of each of the N_y signals registered with frequency encoding along OX, after phase encoding along OY. Each of these N_y spectra is an image of the slice along the axis, distorted by phase variations. The second FT makes the same calculation for the N_y spectra, along the direction of phase encoding: Each step of phase encoding gradient is equivalent to a point along a pseudo-time scale.

Often an image acquired with matrix N_x, N_y is reconstructed with a larger matrix N_x, $2N_y$ by interpolation of data, an improvement of the display without additional information (Figure 1.6.7(b)).

1.6.7 Three-dimensional imaging

Three-dimensional (3D) imaging associates to each voxel of a selected volume, a number proportional to the local value of magnetisation.

From this collection of data, the images of slices with any orientation can be further displayed (since 2D visualisation is easier), without the need of another acquisition.

The first step of 3D acquisition is the excitation of resonance in the volume under study. The phase encoding is performed along two directions, before signal acquisition in presence of the frequency-encoding gradient. The number of phase encoding steps is defined by the matrix in the two corresponding directions: Typically, one may envisage that N_z (e.g. 64) phase-encoding steps are done along the first axis, N_y (e.g. 128) phase encoding steps are done along the second axis and Nx (e.g. 256) points are sampled according to the third axis during each signal acquisition (Figure 1.6.6(d)). Then the volume under study is divided into $N_x.\ N_y.\ N_z$ (e.g. $256 \times 128 \times 64$) voxels.

All the possible combinations of the two phase-encoding gradient (their number is $N_y.\ Nz$) are applied successively and for each a signal is read.

The acquisition time is at least $N_y.\ N_z.\ T_R$ multiplied by the number of averages of identical signals N_a if needed. The large number of signals measured successively ($N_a.\ N_y.\ N_z$ instead of $N_a.\ N_y$ in 2D imaging) contributes to efficient noise averaging (as explained further at paragraph 8.3).

From the large number of signals needed, 3D acquisition is usually performed at short values of T_R and T_E, except in MRI microscopy where acquisition times of several hours are often needed. 3D imaging is mostly used to display complex anatomy (brain, embryonic structure, articulations), when physiologic motion does not interfere with image quality. Figure 1.6.8 shows one slice of a 3D volumic acquisition.

1.6.8 From slow imaging to snapshot imaging

1.6.8.1 Snaphot imaging

In the two fastest acquisition sequences, echo planar imaging (EPI) or fast spin-echo imaging (FSE), N_y successive spin-echo or gradient-echo are read within a very short time, each one with a distinct phase encoding, in order to obtain all the information needed to build the image in one single signal acquisition (Stark and Bradley, 1992; Ness Aiver, 1997). This acquisition has to be performed within a time comparable to the time for signal decay, $T2^*$ or $T2$, typically 50–100 ms. Each elementary echo is read more quickly than in usual conditions, and gradients for encoding are set very quickly to strong intensities, needing powerful hardware. Another full image can be built after the recovery time T_R.

EPI is very sensitive to magnetic inhomogeneity, a problem when images are done at high magnetic field. The images obtained by snapshot acquisition are not degraded by motion, but their spatial resolution is low: N_y and N_x have low values, typically 64–128. The time between successive echoes is very short. The effective echo time TE_{eff} (often equal to the time at middle of the echo train) determines the influence of $T2$ on the signal, and the images are strongly $T2$-weighted (for FSE) or $T2^*$-weighted (for EPI). Then magnetic field inhomogeneities have strong influence on the quality of EPI images.

1.6.8.2 Segmented imaging

In less fast 'segmented' acquisitions with EPI or FSE sequences, a train of N echoes is read within one acquisition, each one at a distinct phase encoding. At the following T_R, another echo train is read, until the N_y signals needed for completion

Figure 1.6.7 Display of the signals registered to build an image. (a) Data before reconstruction. N_y signals (here 64), one for each phase encoding step, are displayed. Each signal contains N_x values read during 4 ms around the echo time T_E. Each signal is maximal at mid acquisition, at the echo time T_E. Larger signals are registered around the central line ($G_y = 0$). The whole of the slice contributes to each of the signals displayed. All the signals registered contribute to each pixel of the reconstructed image. (b) Image obtained by 2D Fourier transform of these data. The acquisition matrix is 256×64 (64 signals each with 256 samples). After Fourier transform, the image is interpolated: The display matrix is 256×256. This gradient-echo image shows the magnetic distortion induced by an air bubble at the middle of a sphere filled with water. The magnetic field distortion caused by the difference between air and water susceptibilities has a spatial extent much larger than the diameter of the air bubble, with two lateral lobes. Also the bubble is distorted in the phase encoding direction, because the resolution is lower and then the encoding gradient lower

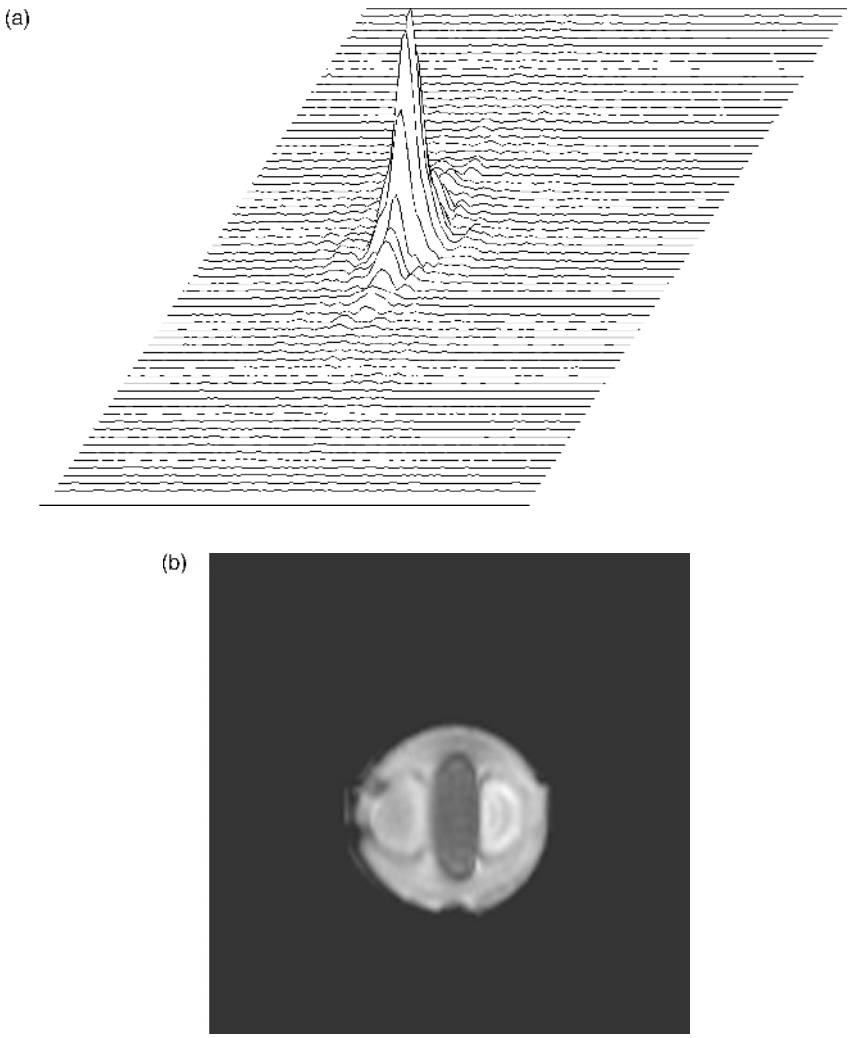

of image acquisition are obtained. Then the acquisition time is shortened N times and lasts for $(N_y/N).T_R$. This trade off between speed of acquisition and spatial resolution is less technically demanding and less subject to artifacts, and also images are less heavily $T2$ or $T2^*$ weighted. Figure 1.6.9 illustrates these snapshot and segmented spin-echo imaging techniques.

1.6.8.3 Parallel imaging

Parallel imaging, now available on all medical MRI systems, is another way to speed the acquisition of images (Hornack, 2005). Several (typically 4–12) receiver coils, positioned around the object, collect signals from distinct regions weakly overlapping. This makes possible to perform a lower number of phase encoding

Figure 1.6.8 *Ex vivo* 3D imaging of articular structures in rabbit knee at 4.7 T. 3D imaging is done at 4.7 T with a spin-echo sequence ($T_R = 500$ ms, $T_E = 10$ ms). Voxel size is $100\mu \times 200\mu \times 400\mu$. Acquisition time is 3 h. The knee structures are displayed on 48 thin contiguous slices. Fat is visualised with a high signal; cartilages have higher signal than bone and muscle. Cortical bone is dark; spongious bone appears heterogeneous, due to the magnetic heterogeneity induced by bone/fat interfaces (*courtesy of G. Guillot, U2R2M, Orsay France*)

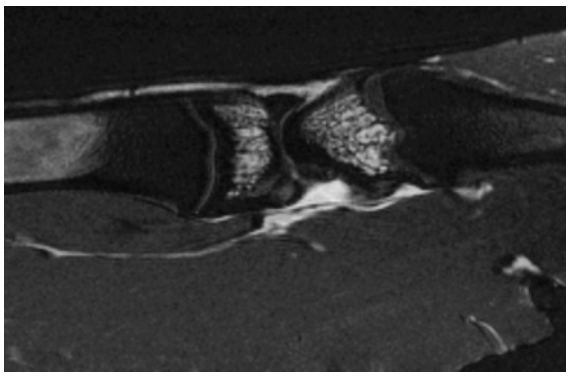

steps (e.g. $N_y/4$ instead of N_y). Then complex algorithms allow to reconstruct the full image with matrix $N_x.N_y$.

1.7 MRI and contrast

MRI is an imaging modality that offers huge versatility as so many different parameters may contribute to the contrast of images.

MRI is a black and white technique: The signal intensity is proportional to the local value of the proton transverse magnetization, modified by local values of parameters such as relaxation times, water diffusion coefficient, blood motion, blood oxygenation, iron load and so on. Sometimes the information derived from a special sequence is overlaid in 'false colours' upon an anatomical black and white image displaying anatomy.

Increasing the contrast means weakening the signal of some constituents: An image where all voxels

Figure 1.6.9 Fast spin-echo imaging. Transverse section of a fruit obtained at 1.5 T.
(a) Segmented acquisition: 16 groups of 8 echoes, each for one step of the phase encoding gradient, are obtained with T_R. 3s: The acquisition lasts 48 s, eight times shorter than the conventional acquisition done with same T_R). Matrix is 128×128. Spatial resolution $= 0.63$ mm $\times$ 0.63 mm $\times$ 3 mm. The effective echo time, corresponding to the middle of the echo train, is $TE_{eff} = 15$ ms. This image done with long T_R and short T_E has weak $T1$ and $T2$ weighting.
(b) Single-shot acquisition: 64 echoes, each for one step of the phase encoding gradient, are registered during 170 ms, that is the total acquisition time. Matrix is 64×64. Spatial resolution 1.25 mm $\times$ 1.25 mm $\times$ 3 mm. The effective echo time, corresponding to the middle of the echo train, is $TE_{eff} = 80$ ms. This low-resolution snapshot image is strongly $T2$ weighted: The variation of hydration between the different fruit layers is highlighted

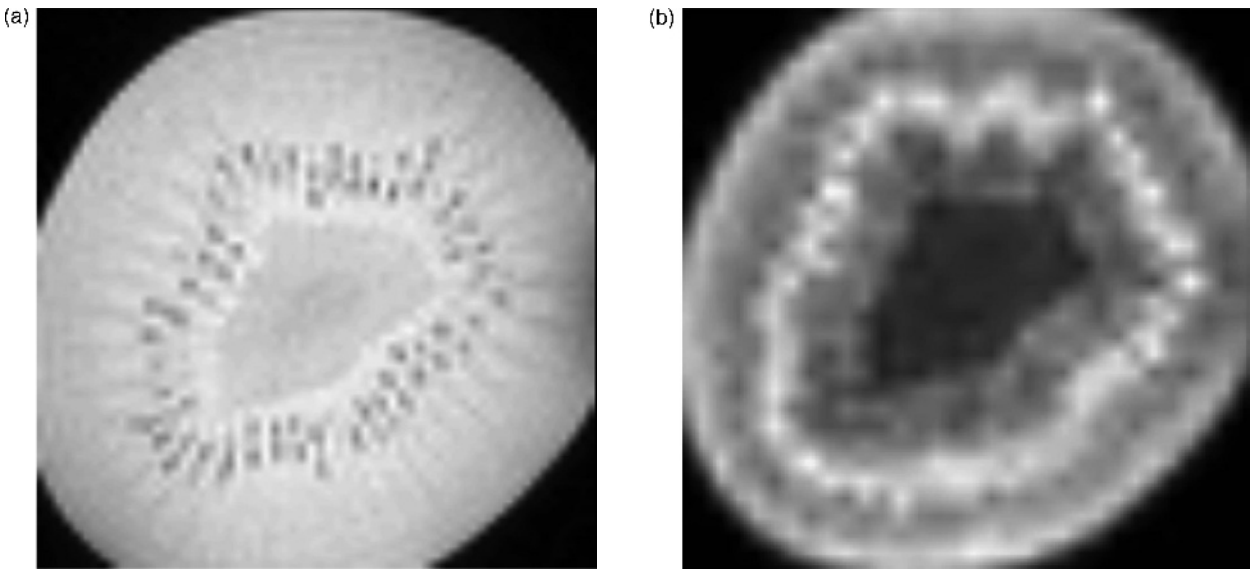

would have maximal intensity would not be very informative.

Let us consider now the basic parameters currently used in anatomical imaging.

The proton density is the first parameter that determines magnetization. The maximal signal intensity is that of pure water with maximal proton concentration, at least if the interval between measurements is much longer than water $T1$ and if the decay of transverse magnetization at the time of echo is negligible. The proton density does not vary so much between soft tissues (the water content is in the range 65–85% in non-adipose tissues; in adipose tissue, the fat content is around 85%, corresponding to a high proton density from -CH2- and -CH3- groups).

The other determinants of contrast are more effective. The amplitude of variation of the relaxation times in biological objects is much larger than that of the proton density, so that the contrast is modulated mostly by $T1$ and $T2$ values in each voxel.

The way to adjust contrast is to play with the times T_R and T_E of the acquisition sequence, the influence of which is related to relaxation times $T1$ and $T2$.

The repetition time T_R is the time waited between successive measurements of a slice to rebuild M_z.

The echo time T_E is the time at which some refocusing of dispersed magnetizations is done during signal acquisition.

Key points

The three main determinants of contrast are the proton density, which determines M_o, and the relaxation times $T1$, $T2$ of hydrogen nuclei. The repetition time T_R between measurements conveys the sensitivity to $T1$, and the echo time T_E conveys the sensitivity to $T2$.

When a spin-echo acquisition is done with short T_R and short T_E, the tissues with short $T1$ values (such as fat) appear as bright and tissues with long $T1$ (such as water) appear as dark. Images are mostly dependent on $T1$ values and are qualified as '$T1$ weighted'.

When a spin-echo acquisition is done with long T_R and long T_E, the tissues with long $T2$ values (water, other fluids, oedema) appear as bright, and those with short $T2$ values (muscle, tendon, bone) appear as dark. Images are mostly dependent on $T2$ values and are qualified as '$T2$ weighted'.

When fast imaging is performed at short value of T_R, other determinants of contrast are the flip angle and the management of the residual transverse relaxation.

Often several images of a same organ with different sequences are registered in order to obtain better characterization.

1.7.1 Contrast with spin-echo sequences

Let us write the expression of signal in the case of a classic spin-echo sequence (the flip angle for NMR excitation is 90°; the refocusing is done by a 180° RF pulse).

In a given voxel with coordinates x, y, z, the transverse magnetization $M(x, y, z)$ is proportional to the local density of protons that determines M_o.

It also depends on the time interval T_R between two measurements, during which M_z is rebuilt:

In the simple case where M is flipped with 90° angle at the beginning of the sequence, then $M_z = 0$ at time 0, and after waiting T_R, it is rebuilt to the value.

$$M_z(T_R) = M_o[1 - \exp(-T_R/T1)]. \tag{1.35}$$

At the following excitation, this longitudinal magnetization becomes transverse

$$M_t \text{ initial} = M_z(T_R). \tag{1.36}$$

M_t decreases during its precession, and the signal is read around the echo time T_E

$$M_t(T_E) = M_t \text{ initial}. \exp(-T_E/T2). \tag{1.37}$$

The spin-echo signal is proportional to

$$M_t(T_E) = M_o.[1 - \exp(-T_R/T1)]. \exp(-T_E/T2), \tag{1.38}$$

where M_o depends on the local proton tissue concentration; local values of $T1$ and $T2$ depend on many complex parameters related to tissue structure, and the contrast is modulated by the choice of the parameters T_R and T_E, within some limits.

Figure 1.7.1 displays the variations of M_z and M_t with T_R and T_E for brain components.

Images with short T_R and short T_E values (such as Figure 1.9.3) display as bright the tissues with short $T1$ values (such as fat) and as dark the tissues with

Figure 1.7.1 Contrast: Influence of M_o, $T1$, $T2$. Values of M_z and M_t are calculated for $T1$, $T2$ and water percentages representative of brain white matter grey matter and cerebrospinal fluid (CSF) at 3 T.

Tissue	Water percentage (%)	$T1$ (ms)	$T2$ (ms)
White matter	80	600	60
Grey matter	90	900	90
CSF	100	2500	500

(a) Playing with T_R and $T1$. M_z recovery curves are plotted as a function of the repetition time T_R, according equation 1.35M_z values at long T_R reflect the tissue water percentages. At $T_R = 1000$ ms the values of M_z mostly reflect $T1$ differences between the three brain components. At time T_R much larger than $T1$ values (e.g. 10 000 ms), M_z is lower in white matter from its lower water percentage.
(b) Playing with T_E and $T2$. Signals for $T_R = 1000$ ms are plotted as a function of the echo time T_E, according equation 1.38. At short T_E, the values of signals mostly reflect $T1$ differences. At T_E above 20 ms WM and GM are differentiated from their $T2$ values. CSF appear as brighter only above $T_E = 80$ ms, due to its longer *T1*

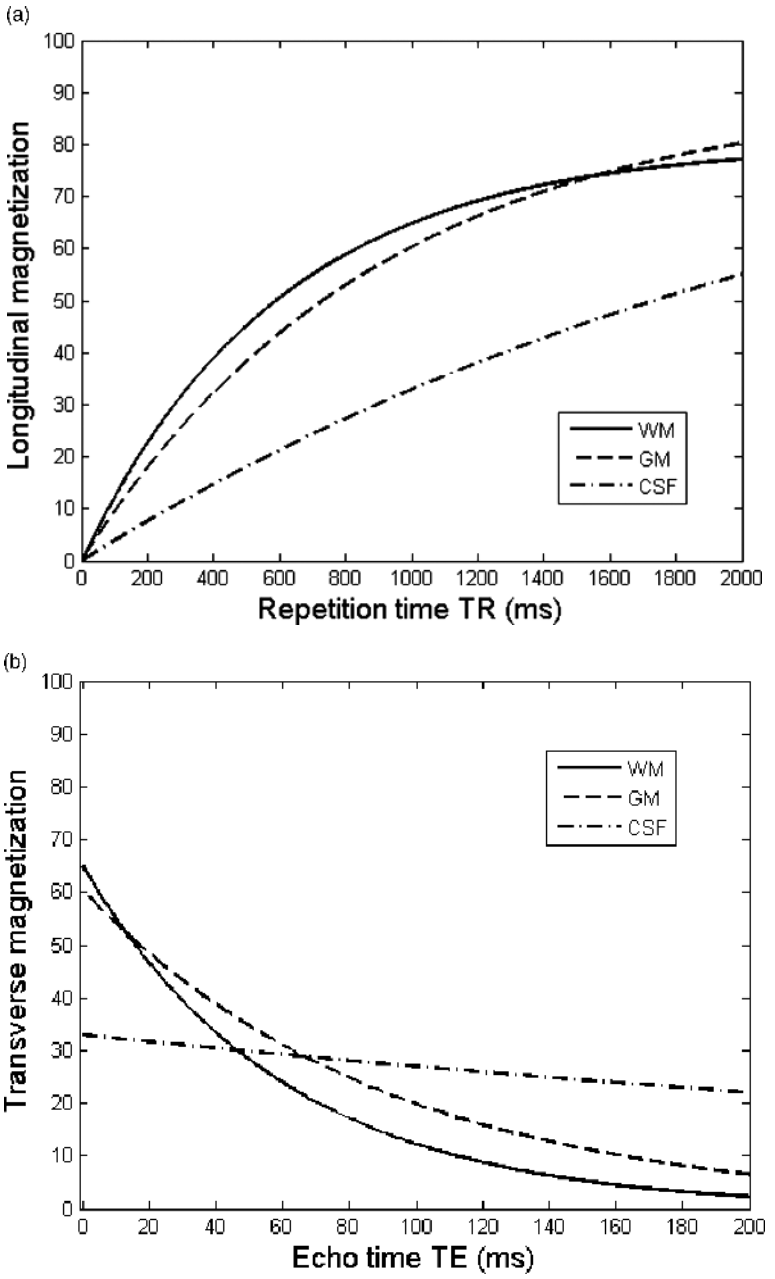

Figure 1.7.2 Contrast: Influence of M_o, $T1$, $T2$. Coronal images of normal Macaque brain, done at 3 T. A 8 cm $\times$ 5 cm surface coil laid at top of the skull is used for excitation and reception: the RF field $B1$ varies with the distance from the coil; this variation is the cause of image quality degradation near the coil, stronger for the spin-echo sequence. The same anatomical plane through striatal structures is visualised with different parameters.
(a) M_o-weighted gradient-echo image ($T_R = 2000$ ms, $T_E = 4$ ms, flip angle 25°). The contrast between brain structures is low; white matter tracts are delineated, from the lower proton density: A large fraction of myelin protons, strongly bound to membrane phospholipids, have very short $T2$ values and yield no signal even at this short echo time.
(b) $T1$-weighted inversion-recovery gradient-echo image ($T_R = 2800$ ms, $T_I = 880$ ms, $T_E = 4$ ms). The inversion time is chosen to suppress CSF signal as shown by Figure 1.3.3(b). From their markedly different $T1$ values, there is a high contrast between the white matter tracts with high signal, grey matter in cerebral cortex, caudate (arrow) and globus pallidus (arrowhead) with medium signal and CSF which appears dark.
(c) $T2$-weighted spin-echo image ($T_R = 2000$ ms, $T_E = 70$ ms). From their markedly different $T2$ values, there is a high contrast between CSF ($T2 = 500$ ms) in ventricles and subarachnoidal spaces (white), and brain ($T2$ about 60–80 ms). Globus pallidus appears slightly darker from the higher iron concentration. The temporal muscles with $T2$ about 30 ms are still darker (*courtesy of F. Boumezbeur and V. Lebon, Service Hospitalier Frédéric Joliot, CEA, Orsay France*)

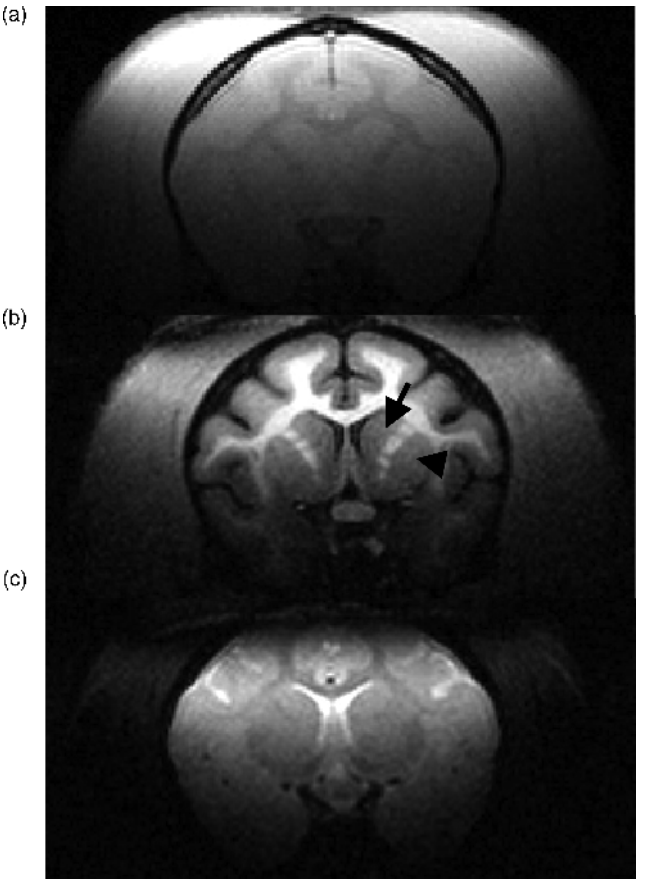

long $T1$ values (such as pure water). They are mostly weighted by $T1$ values and are qualified as '***T*1weighted images**'. The inversion-recovery image of Figure 1.7.2(b) also is $T1$-weighted.

Images with long T_R and long T_E values (Figure 1.7.2(c)) display as bright the tissues with long $T2$ values (water, other fluids, oedema). They are mostly weighted by $T2$ values and are qualified as '$T2$-weighted images'. However, we should keep in mind that image weighting depending on only one parameter is very difficult to obtain; some degree of $T1$ weighting is often present.

Long values of T_R directly cost long acquisition time; small values of T_R mean weak signals.

Short T_E values are limited by the time needed for phase encoding and by the 180° RF pulse duration. Long T_E values mean weak signals from exponential decay of M_t.

1.7.2 Contrast with gradient-echo sequences

Acquisition using a gradient-echo sequence can be done at much shorter echo time than when using a spin-echo sequence: T_E range is 0.5–5 ms depending on gradient hardware. The calculation of contrast is more complex and reflects the diversity of gradient-echo sequences.

The decay of M_t is determined by $T2^*$ instead of $T2$, because the gradient echo does not remove the influence of static magnetic field inhomogeneity. This influence can be utilised (see blood oxygen level dependent (BOLD) contrast at paragraph 11.2) or minimised.

The contrast of gradient-echo images done at very short T_E values and moderate T_R values is similar to that of $T1$-weighted spin-echo images done at the same T_R, but shorter T_E values are needed to limit signal decay and magnetic distortions (see Figure 1.7.2(a,b)).

When the repetition time T_R is shorter than some of the $T2$ values in the sample, some transverse magnetization did not decay to zero at the end of the time T_R. The way to destroy or to recycle this residual transverse magnetization modifies the NMR signal.

This complex way to play with T_R, T_E, the flip angle α and the residual transverse magnetization M_t is explained in Ness Aiver(1997) and Stark and Bradley(1992). The influence of the two last parameters is very briefly described below.

1.7.2.1 Fast imaging at small flip angle

Rapid gradient-echo imaging is often performed with a flip angle α smaller than 90°. Then M_z is less strongly decreased by the excitation at smaller flip angle, and a shorter value of the repetition time T_R is sufficient to rebuild M_z up to a given steady state value. The transverse magnetization available for measurement is lower, being equal to $M_z \sin \alpha$. The trade off is to collect fewer signals while waiting less between measurements.

At a very short T_R value, imaging with a small but optimal flip angle allows to obtain the highest possible signal within a short acquisition time. This is very useful at high field as M_o is higher (and then part of the signal can be sacrificed), and also because $T1$ and then T_R increases with B_o.

Figure 1.7.3 Signal variation with T_R and flip angle in gradient-echo imaging. Evolution of the signal calculated for $T1 = 1000$ ms, at T_R values from 10 to 1000 ms, and flip angles between 10° and 90°. The curves show that at low flip angles the signal reaches a plateau as a function of T_R

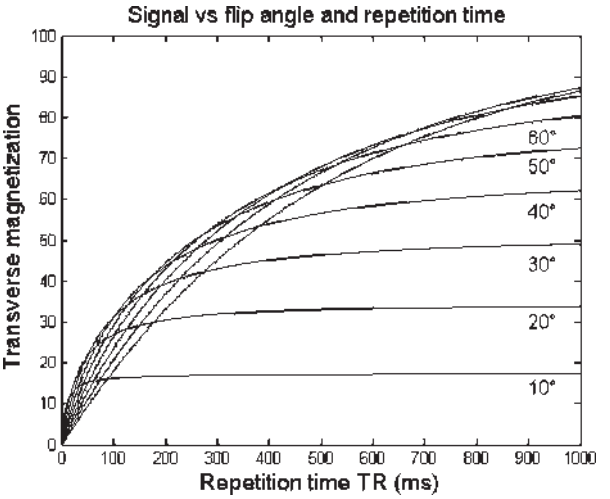

More physics: the optimal flip angle. When the decay of the transverse magnetization is complete at the end of T_R, the steady state signal after several T_R intervals is written as

$$M_t(T_E) = \frac{M_o \sin\alpha[1-\exp(-T_R/T1)].\exp(-T_E/T2*)}{[1-\cos\alpha.\exp(-T_R/T1)]} \quad (1.39)$$

For given values of T_R and $T1$, M_t is maximal at the 'optimal flip angle' α (also named Ernst angle), given by the equation

$$\cos\alpha = \exp(-T_R/T1), \quad (1.40)$$

Figures 1.7.3 and 1.7.4 show the influence of the flip angle upon the signal at a given T1 value and upon an image.

1.7.2.2 Fast imaging at shortest T_R values: recycling of transverse magnetization

At very short T_R values ($T_R < 100$ ms) the transverse magnetization decay is not achieved at the end of the sequence, because T_R is shorter than $T2$ for some

Figure 1.7.4 Influence of the flip angle in gradient-echo imaging. (a) Transverse slice of a lemon done with $T_R = 600$ ms, $T_E = 5$ ms, flip angle $\alpha = 40°$. (b) Same acquisition done with $\alpha = 90°$. Fruit water $T1$ is about 1800 ms. At T_R 1000 ms, at flip angle 40° (the optimal value is 44°), the signal is 60% of the theoretical maximum available, whereas at flip angle 90°, it is only 28%. The contrast between water of the fruit pulp and lipids of the pip with shorter $T1$ is inverted between the two images

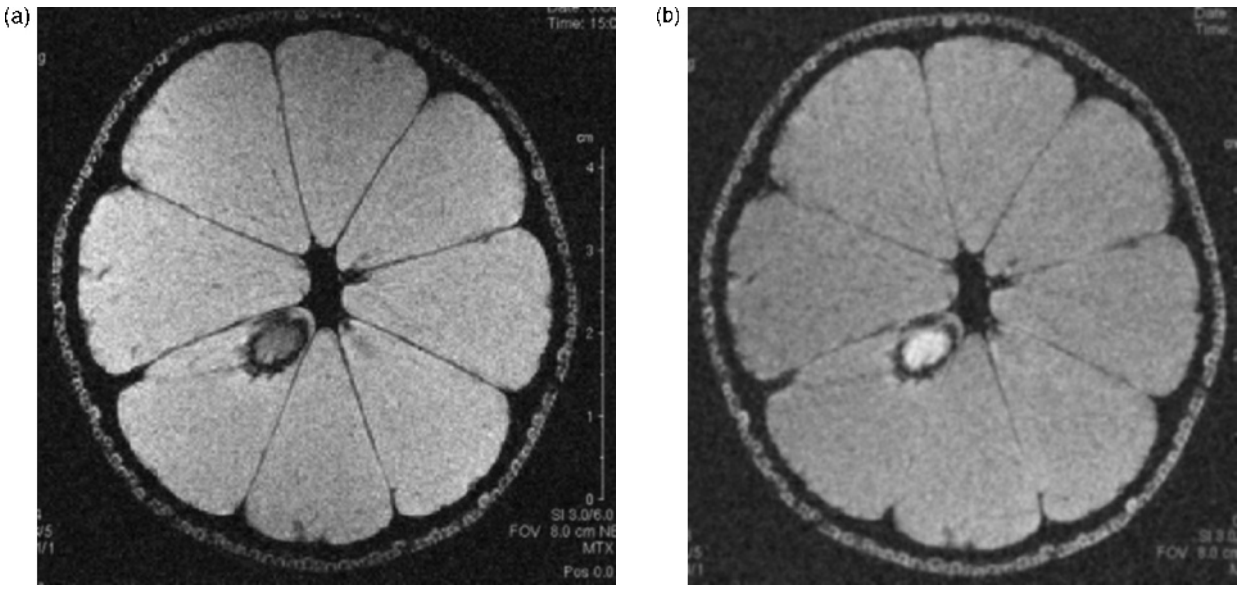

constituents of the sample. Then two distinct measurement strategies are either to spread the residual transverse magnetization by additional gradients or to recycle it.

The destruction (named spoiling) of the residual magnetization yields the contrast described in previous paragraph, depending on T_R, T_E and flip angle values.

The recycling of transverse magnetization yields, in adequate conditions, a signal proportional to M_o and to the ratio $T2/T1$, higher in liquids with long $T2$ values than in soft tissues with shorter $T2$. Then liquids such as blood in cardiac chambers, fluids in cysts, CSF in brain appear as bright. However, a very high homogeneity of the magnetic field is needed. The corresponding '*fully refocused*' sequences bear nicknames such as SSFP or FISP or FIESTA according to the commercial brand of the spectrometer.

1.7.3 More about relaxation times T1, T2, T2*

The relaxation times $T1$ and $T2$ are complex parameters, determined by molecular interactions, which depend on the composition and structure of tissues, and also at different degrees on the magnetic field B_o. $T1$ and $T2$ correspond to distinct physical mechanisms and their values are markedly different in most biological tissues. $T2$ is shorter or equal to $T1$, never longer. Every tissue has its own values of $T1$ and $T2$: This enables MRI to differentiate between different types of tissue.

The longitudinal relaxation time T1 is determined by several mechanisms that add their effects:

- Magnetic interactions between the water protons magnetic moments have weak efficiency because the water molecular motions are extremely fast. $T1$ is very long in pure water (3–5 s).
- Magnetic interactions between the water protons and the protons of macromolecules or proteins are more efficient: $T1$ is then around one second, depending on B_o.
- Magnetic interactions between water protons and paramagnetic substances (with unpaired electrons) are very efficient; these paramagnetic substances are used to shorten $T1$ and to increase contrast (cf paragraph 9).
- Magnetic interactions between fat protons are efficient because the lipid aliphatic chains do not move too fast. Fat has a high proton content and a very short $T1$. Its signal is very bright on $T1$-weighted images.

The transverse relaxation time $T2$ also conveys information on the tissue structure, and is very sensitive to some biological variations such as variations of water content and oxygenation of tissues.

$T2$ is long (~500 ms) in water, because water molecules rotate too fast and magnetic interactions between them are averaged by fast motions. It is long also in other biological fluids and in liquid tissues such as blood. It is shorter, in the range 10–100 ms, in tissues where water molecules have strong interactions with other bigger molecules and the water viscosity is high. $T2$ is much shorter, less than 1 ms, in fibrous media such as tendons and bone, where macromolecules have high concentration and strongly interact with water.

In most, but not all, cases of pathology, $T1$ and $T2$ values are increased in comparison to their values in normal tissues. When the pathology causes the accumulation of iron, $T2$ and sometimes $T1$ values are decreased.

The 'effective' transverse relaxation time $T2^*$ is similar to $T2$ as a time measuring the decay of the NMR signal, but its causal mechanism is different: It is partly caused by the static magnetic field gradients. Since these local gradients do not fluctuate, the dephasing that they induce can be recovered by refocusing, as described in paragraph 6.4. Local variations of the magnetic field are more important when some parts of the object present a magnetic susceptibility (defined at paragraph 9.1) different from that of the bulk water. This is the case of air-filled structures, of bones, of erythrocytes and every biological structure containing iron. The influence of $T2^*$ on NMR signals can be important, either as a parasitic effect (in spectroscopy; in cardiac imaging from the complex shape of lungs filled with air) or as a source of information (in bone structure studies; in brain studies using blood oxygen level dependent (BOLD) contrast introduced in paragraph 10.2).

Figure 1.7.5 Variation of the longitudinal relaxation time in brain structures, as a function of the magnetic field. To determine biologically relevant $T1$ values, two juvenile C57/Bl6/J mice were scanned at three field strengths (4.7, 11.1 and 17.6 T) using a saturation recovery multislice spin-echo sequence in which the recovery time (T_R) was incremented to sample longitudinal relaxation. White matter (white symbols) in the corpus callosum, grey matter (black symbols) in the cortex and CSF (grey symbol) in the ventricles were segmented to provide a range of $T1$ values. Region of interest analysis was utilized to provide mean signal intensities for each of the T_R times. These data were fit to a three component, single exponential model using a nonlinear least squares Levenburg-Marquadt algorithm to generate $T1$ coefficients for each of the neuroanatomical structures (Padgett, Blackband and Grant, 2005) (*courtesy of Dr. K.R. Padgett, Dr. S.J. Blackband and Dr. S.C. Grant of the McKnight Brain Institute at the University of Florida, USA*)

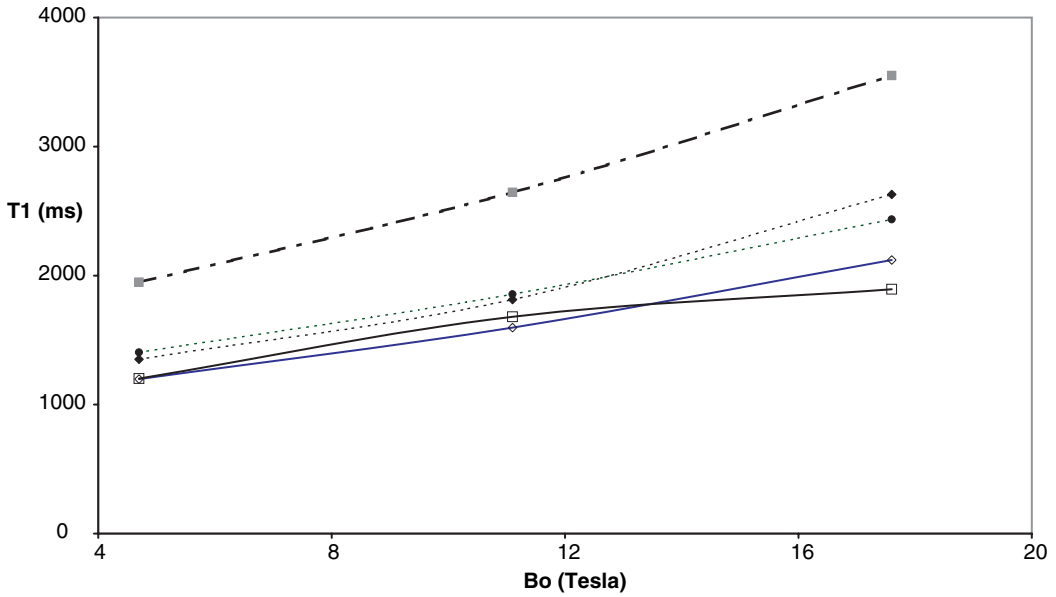

The values of the relaxation times in a given organ depend on many parameters: magnetic field intensity, temperature, species, age of animal and more interestingly modifications induced by pathology. Many data in the literature are obtained from ex vivo organs often studied at room temperature. In vivo measurements are not easily performed in organs like heart, requiring high quality synchronization of data acquisition.

$T1$ increases with the magnetic field Bo (Johnson, Herfkens and Brown, 1985); $T2^*$ and to a lesser degree $T2$ decrease with B_o. The increase of $T1$ values with B_o (Figure 1.7.5) results in longer imaging times; this counteracts with the signal increase at higher magnetic field.

1.8 Sensitivity, spatial resolution and temporal resolution

Key points
Sensitivity of MRI and MRS are measured by the signal-to-noise- ratio. The signal is determined by the number of nuclei detected in the volume of interest. Smaller voxels mean smaller signals, and then lower signal-to-noise ratio. To overcome the signal weakness at high spatial resolution, higher magnetic field B_o and/or more efficient receiver coil are needed. Selection of small voxels also needs strong magnetic field gradient intensity.

The spatial resolution, the signal-to-noise ratio and the acquisition time are three parameters strongly linked. For each MRI protocol, a compromise is negotiated between them.

The field of view is the spatial extent that can be mapped adequately without fold-over.

Sensitivity of MRS is further limited by the concentration of molecules studied and by the intrinsic sensitivity of the nucleus detected.

1.8.1 The spatial resolution

As MRI makes a correspondence between one volume element, the voxel, and one image element (or picture cell), the pixel, the in-plane resolution is given by the voxel dimensions δx and δy. (Often smaller pixel size is obtained by interpolation.) Usual values range from 1mm to 50 μm depending on resolution needed or affordable. Out-plane resolution is given by the slice thickness δz (usually larger, between 2 mm and 500 μm). 3D imaging, at the cost of a long acquisition time, allows to reach isotropic spatial resolution with thinner slices (δx, δy, δz between 100 μm and 40 μm).

The volume of one voxel is the product

$$\delta v = \delta x.\delta y.\delta z. \tag{1.41}$$

1.8.2 Determinants of the MRI signal

The signal of the voxel is related to its magnetization and to the volume of the voxel:

$$\delta M = M_o.\delta v. \tag{1.42}$$

At first a higher spatial resolution means a smaller voxel volume and a weaker elementary signal.

The magnetization M_o is proportional to the number of nuclei par volume unit and to their polarization P (see Section 1.2.4. and Table 1.2.1). The signal amplitude S is also proportional to the resonance frequency F_o. Then S increases roughly as the square of the magnetic field intensity B_o (or slightly less rapidly depending on instrumental factors and animal size).

The signal amplitude in a given acquisition sequence also depends on the values of T_R, T_E, $T1$, $T2$, as written in the Eq. (1.38) for the spin-echo sequence and α, $T2^*$ for the gradient-echo sequence.

At last, importantly, the signal amplitude is proportional to the receiver coil efficiency. A receiver coil is more efficient when a larger voltage is induced by the precession of a given magnetization. The voltage induced is higher when the receiver coil is very close to the sample. Choosing an efficient coil is the simplest and cheapest way to increase the signal-to-noise ratio of NMR measurements.

1.8.3 The noise

The electronic noise is a fluctuating voltage added to the NMR signal at reception (Webb, 2003). It neither depends on voxel size, nor on B1 intensity (i.e. on the flux of RF photons). The noise originates from the random electrical fluctuations in the coil and it is proportional to the resistance R of the receiver coil: A 'good' receiver coil has a low resistance. Some noise may also originate from the electric losses in the

Figure 1.8.1 Field of view and spatial resolution. Images of a fruit done at 1.5 T with a spin-echo sequence ($T_R = 1000$ ms, $T_E = 15$ ms). The acquisition time is 512 s; the matrix is 512×256. Left, FOV 10 cm; spatial resolution is $390\mu \times 195\mu \times 3000\mu$. Right, FOV 5 cm; spatial resolution is $195\mu \times 97\mu \times 3000\mu$. The spatial resolution is higher, from identical matrix and smaller field of view. Therefore the signal-to-noise ratio is lower (divided by four!). The fold over (also named aliasing) of an outer portion of the object is observed: The frequency spectrum corresponding to the width of the object is wider than the spectral range that can be analysed properly in the conditions of acquisition

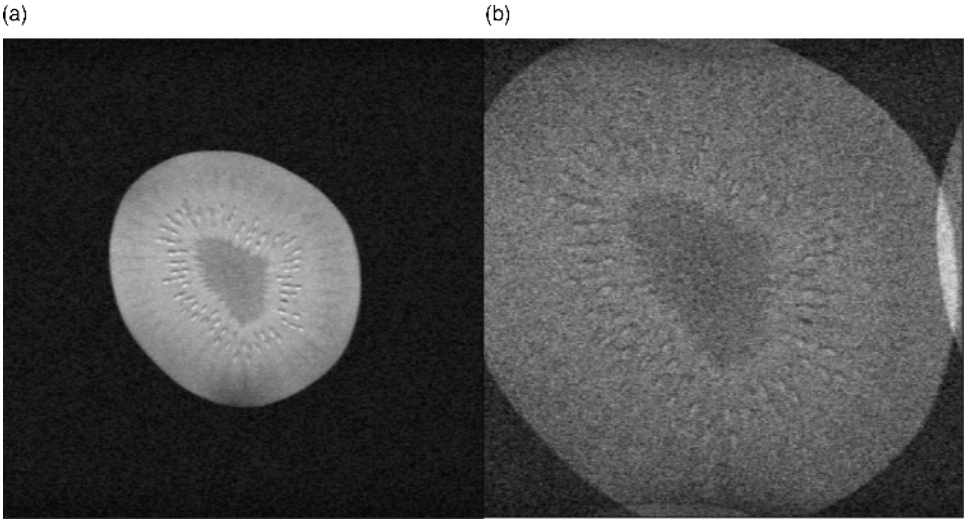

object; this is especially important for larger animals or those at very high magnetic field.

A small receiver coil has a lower resistance than a larger one, and it also picks noise (but also signal) from a smaller volume across the object.

The electronic noise is independent of the frequency. After Fourier transform, it is spread uniformly across the spectrum, and then across the image. It can be appreciated visually on images of a homogeneous structure, when signals of neighbouring pixels have different intensities, as represented on Figure 1.8.1. It can be measured easily from the fluctuation of signal in the background around an object, in the zones where signal would ideally be equal to zero, as may be seen in Figures 1.6.5 and 1.7.4.

The signal-to-noise ratio can be increased, at the cost of a longer acquisition time, by taking the average of several measurements, that is adding Na signals, thus multiplying signal – and also the measurement time – by N_a and the noise only by $(N_a)^{1/2}$.

The physiological noise, typical of living objects, results from motions that are not synchronized with the phase encoding: Signals from moving parts of the object are then depicted at improper location in the image, and they behave as some additional noise (see Figure 1.6.4).

1.8.4 The field of view and the spatial resolution

The spatial resolution is determined by the strength of the magnetic field gradient available and by the number of points sampled along the corresponding direction of the image.

The field of view is the maximal dimension of the object that can be represented accurately in given conditions of acquisition. There is a limitation of this dimension, because there is a limitation of the highest frequency that can be analysed by the spectrometer.

The spectral width available around the central frequency F_o is ΔF_o, related to parameters of acquisition.

The width of the spectrum of an object of length X, when its signal is read with a frequency encoding gradient G, is $\Delta F = (\gamma/2\pi).G.X$.

If $\Delta F > \Delta F_o$, the parts of the spectrum of the object that lie out of the interval $(-1/2\Delta F_o, +1/2\Delta F_o)$ are not correctly analyzed: They are 'undersampled'

Figure 1.8.2 Using a high temperature super-conductive coil. High resolution images of stems are done with voxel size $39 \times 39\,\mu m^2$ in plane and slice thickness $900\,\mu m$, at 1.5 T. (a) Detection with a small (12 mm diameter) circular copper coil. (b) Detection with a same sized high temperature super-conductive coil: The signal-to-noise ratio is improved by a factor of 5 (*courtesy of J.C. Ginefri, UMR CNRS 8081 and Université Paris-Sud, Orsay, France*)

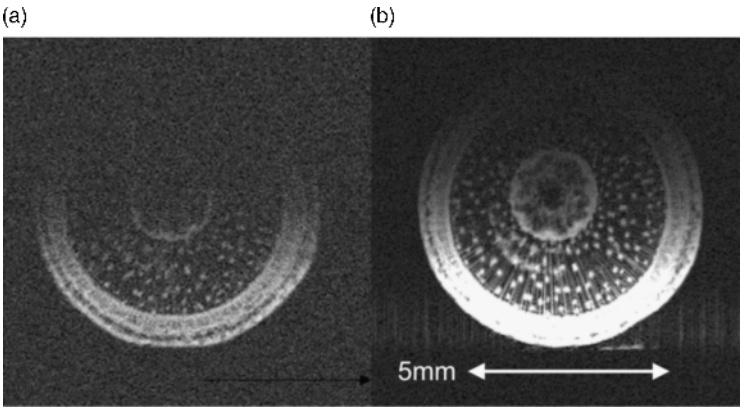

(Ness Aiver, 1997), and so they are translated into lower frequencies superimposed to the frequencies that represent the central part of the object. The corresponding regions of the object are wrongly localized, and are folded over the central zone. This artefact is named 'aliasing'; it is illustrated in Figure 1.8.1(b).

This makes it difficult to build the image of a small organ inside a large body; but technical recipes such as 'suppression' of the magnetization in parts of the object may solve this difficulty (Parzy *et al.*, 2003) as illustrated by figure 10.1.3.

1.8.5 More technology: High temperature supraconductive coils

The signal-to-noise ratio strongly depends on the efficiency of the RF receiver coil; the reason why coils are often optimised for a given experiment (Mispelter, Lupu and Briguet, 2006).

The signal-to-noise ratio (SNR) of images can be enhanced by using a receiver coil with extremely low resistance. The receiver coil efficiency can be further increased if the coil is built from a super-conducting material that has a resistance much lower than copper, at very low temperature. The coil is located near the object of study, itself kept at 'normal' temperature. This new technology needs complex and expensive cryogenic system, using liquid nitrogen (77 °K). Its implementation in pre-clinical or clinical environment is still in progress. However, the use of super-conducting coils opens a lot of investigations on different fields of biomedical applications. The SNR can be 4 to 15 times higher than that with a similar room-temperature copper coil, a function of imaged area (Ginefri *et al.*, 2005) as illustrated by Figure 1.8.2. Then current whole body MRI systems at 'moderate' field Bo can be used to examine small animals. The accessible spatial resolution at a given field is comparable to that usually obtained at a field two or three times higher. For several biomedical issues, imaging with super-conducting coils can offer a true alternative to higher magnetic field.

1.8.6 High resolution and Microscopy

Higher spatial resolution is needed for smaller animal imaging, mouse at first. Scaling from the human to the mouse corresponds to a decrease in linear dimension of approximately 15-fold. For example, if the voxel size is scaled down from $(1\,mm)^3$ to $(70\,\mu m)^3$, the voxel volume is divided by 3500 compared to usual clinical MRI, and the same figure is needed for sensitivity gain if equivalent signal-to-noise ratio is planned. Note that functional imaging is often done with coarser spatial resolution. Part of the sensitivity gain needed is obtained by increasing the field strength

and by decreasing the receiver coil size (efficient and less expensive). The remaining sensitivity gain is obtained by averaging multiple acquisitions so that acquisition time can be several hours.

In vivo microscopy has been proposed initially as a tool to visualise the embryonic development, with the help of labelling some cells with a paramagnetic contrast agent (Jacobs and Fraser, 1994). *Ex vivo* 3D acquisitions with very high spatial resolution, though bringing no functional data, bear some advantages in regard to optical microscopy: The shape of organs and the relation between organs are clearly depicted, the field of observation is larger, 3D reconstruction of blood vessels is possible and the technique is non destructive, allowing other use of organs after MRI. Johnson *et al.* (2002) presented *ex vivo* high-resolution microscopy of mouse whole body or organs. In their study, acquisition times last 14 h, and fixation of tissue is done with a mixture of formaline and Gd-DTPA to shorten $T1$ of tissues and then T_R and the acquisition time.

1.9 Contrast agents for MRI

Key points

Contrast agents for MRI are either positive agents (increasing water signal) or negative agents (decreasing water signal). They contain strongly paramagnetic or ferromagnetic metallic compounds. They are not detected directly but modulate the signal of protons, a factor that increases their efficiency.

MRI natural contrast is easily made high by clever choice of T_R, T_E, depending at first on M_o, $T1$ and $T2$. Also MRI acquisitions can be sensitised to many other parameters (see paragraph 11). Yet contrast agents are widely used. They modify locally $T1$ or $T2$ or $T2^*$ values and help to get additional information such as the permeability of blood vessels, the vascularity of lesions, the extent of perfusion defects in brain or heart and the location of magnetically labelled cells.

Rinck (2001) wrote an excellent introduction to contrast agents for MRI. The field of application of contrast agents (CA) is wider for animal experimentation where the requirements of clinical safety are lower and then 'experimental' products built by research laboratories may be used.

1.9.1 What are diamagnetism, paramagnetism, ferromagnetism and superparamagnetism?

The magnetization of a sample depends on how magnetic moments inside are polarized (spontaneously or under action of the external magnetic field). The 'electronic' magnetization that derives from electronic magnetic moments is always much higher (about 10^4 times) than the nuclear magnetization.

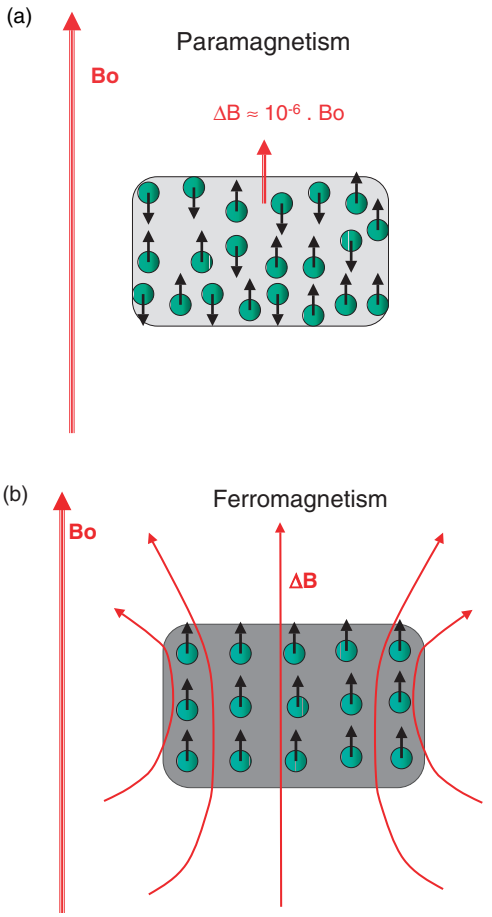

Figure 1.9.1 Paramagnetism and ferromagnetism. The additional field ΔB, in the piece of magnetic material and around it, is proportional to the product χ. B_o, where χ is the magnetic susceptibility of the material. This product is multiplicated by geometrical factors. χ is typically three orders of magnitude larger in the ferromagnetic material than in the paramagnetic material. Around the piece of ferromagnetic material a strong variation of the magnetic field takes place over a distance larger than the dimensions of the piece of material

Table 1.9.1 Characteristics of some magnetic contrast agents at 0.47 Tesla

Contrast agent	k1 (s^{-1} . mM^{-1})	k2 (s^{-1} . mM^{-1})	Rat plasma half-life (min)	Size (nm)
Positives				
Gd-DTPA	4.5	5.9	20	1
Gd-DOTA	3.8	5.8	23	1
Gd-BOPTA	4.4	5.6	Biexponential (5.5/22)	1
Negatives				
AMI 225	23	107	10	80–120
AMI 227	22	53	118	30

Data given for the main contrast agents validated for human diagnostic are the relaxivities k1 and k2 that link T1 and T2 to the contrast agent concentration (see equations (1.46) and (1.47), the plasma half-life and the size of the molecule or particle.

The susceptibility is the ratio of the magnetization (defined at paragraph 1.2.3) to the external magnetic field:

$$\chi = M/Bo. \tag{1.43}$$

In a sample such as drawn in fig 1.9.1 the additional magnetic field created by the internal magnetic moments is proportional to $\chi.B_o$. Around the sample, the influence of internal magnetic moments decays quickly across distance. If the surrounding material has a different susceptibility, the magnetic field outside has a different value, and there is a zone of inhomogeneous magnetic field at the interface.

Briefly, four main types of electronic magnetism are described:

Diamagnetism is observed in compounds with paired electrons such as water, fat and a vast majority of the organic compounds: The field inside a diamagnetic material is slightly lower than its value outside (the additional term is very weak: -10^{-8} times the external field).

Paramagnetism is observed in compounds with unpaired electrons such as iron, copper, nickel, manganese, rare earths as gadolinium and also dioxygen O^2. When the interactions between atoms are weak, magnetic moments are not oriented at zero external magnetic field, and they line parallel or anti-parallel to the magnetic field (see paragraph 1.2.3). The resulting effect is a slight increase of the magnetic field inside the material (the additional term is weak: $+10^{-6}$ to $+10^{-7}$ times the external field).

Ferromagnetism is observed in compounds with unpaired electrons as iron, cobalt, nickel, in metallic state, when the interactions between neighbouring atoms are strong. Magnetic moments are fully ordered under a weak magnetic field, and often stay ordered at zero external magnetic field. The magnetic field inside and around a piece of ferromagnetic material is very strong: The piece of ferromagnetic compound is a magnet.

Superparamagnetism is a phenomenon quite similar to ferromagnetism, in conditions where the total number of atoms is weak, such as in small solid particles smaller than 30 nm containing iron oxides. Then the magnetic moments are fully ordered in the presence of external magnetic field, but the magnetization does not persist in the absence of external magnetic field.

More physics: the relaxivity of contrast agents

The efficiency of a relaxation mechanism is expressed by the *relaxation rate* that is the inverse of the relaxation time: A high efficiency of relaxation corresponds to a high relaxation rate $R1$ (resp. $R2$) and then a short relaxation time $T1$ (resp. $T2$). When several mechanisms a, b,... contribute altogether to the relaxation, their contributions to the relaxation rate are additive. The relaxation of the longitudinal and transverse components of water nuclear magnetization are then written as

$$1/T1 = R1 = R1a + R1b + \ldots, \tag{1.44}$$
$$1/T2 = R2 = R2a + R2b + \ldots.. \tag{1.45}$$

In the presence of a contrast agent, the relaxation rate of a tissue is the sum of its natural relaxation rate and of an additional term from the contrast agent. The relaxation rate from the contrast agent is the product of the concentration of the contrast agent, C, by its relaxivity k.

In a tissue with natural relaxation times $T1o$, $T2o$ (relaxation rates $R1o$, $R2o$), the relaxation rates are written as

$$R1 = R1o + k1.C \tag{1.46}$$

also written

$$1/T1 = 1/T1o + k1.C,$$
$$R2 = R2o + k2.C, \tag{1.47}$$

also written

$$1/T2 = 1/T2o + k2.C,$$

where $k1$ (resp. $k2$) are the longitudinal (resp. transverse) relaxivities of the contrast agent in the tissue and C is its concentration. $k1$ and $k2$, expressed in s^{-1}/mM^{-1}, measure how the CA at concentration 1 mM increases $R1$ or $R2$, and then shortens $T1$ or $T2$.

The positive contrast agents that contain gadolinium have similar efficiency for $T1$ and $T2$ shortening ($k1$ and $k2$ have similar values). As in most tissues, $T2$ is much shorter than $T1$, that is $R2o \gg R1o$, the shortening of $T2$ is negligible at low concentration of the agent.

With the negative contrast agents, $k2$ is larger than $k1$, corresponding to efficient $T2$ shortening; the shortening of $T2^*$ is still more effective, and better exploited by gradient-echo imaging. $T2^*$ shortening is not expressed by a relaxivity because it heavily depends on the measurement sequence. Table 1.9.1 shows the relaxivities of some contrast agents approved for diagnostic imaging.

1.9.2 Positive paramagnetic contrast agents

The positive contrast agents contain paramagnetic atoms with unpaired electrons, usually gadolinium. The gadolinium atom Gd has 7 unpaired electrons; its electronic magnetic moment is very large (10,000 times that of a proton). Furthermore, the kinetic of fluctuations of its magnetic moment is optimal, so that the relaxation of water molecules around this atom is strongly increased (just imagine it as a magnetic stirrer in a jug of water).

Positive contrast agents are molecules which contain one or several gadolinium atoms (or less frequently manganese atoms). As the free gadolinium ion Gd^{3+} is toxic, Gd is chelated to a complex with very high stability so that free Gd^{3+} release in tissues is negligible and the contrast agent clearance is complete, usually through renal elimination. Chelates of Gd are extremely safe products.

The shortening of $T1$ causes an increase of proton signal, as long as the acquisition is $T1$-weighted, which means that the repetition time T_R value is not too long (see Eq. (1.38)). Then these agents increase water signal of the zone inside which they are dispersed: They have to be exposed to water.

Conversely shortening of $T2$ causes a decrease of proton signal, more effective at long T_E values. As this effect is opposite to that induced by $T1$ shortening, it is better to handle the CA at a concentration low enough to shorten mostly $T1$ as illustrated in Figures 1.9.3 and 1.9.4.

Figure 1.9.3 Variation of water signal in the urinary bladder of a mouse with Gd concentration, during the urinary elimination of GdDTPA injected IP at a dose of 0.5 mM/kg; axial spin-echo image with TR 700 ms, TE 15 ms, at low spatial resolution (pixel size 273μ).Urine $T1$ and $T2$ are shortened by the contrast agent. The upper zone in urinary bladder contains light urine with lower concentration of Gd-DTPA. The water signal is strongly increased, from $T1$ shortening. The lower zone in urinary bladder contains heavier urine with higher concentration of Gd-DTPA. $T1$ and $T2$ are shortened under 20 ms so that the water signal is decreased, from $T2$ shortening. The urinary concentration of Gd-DTPA is about 10 mM at the transition between the bright and the dark zones

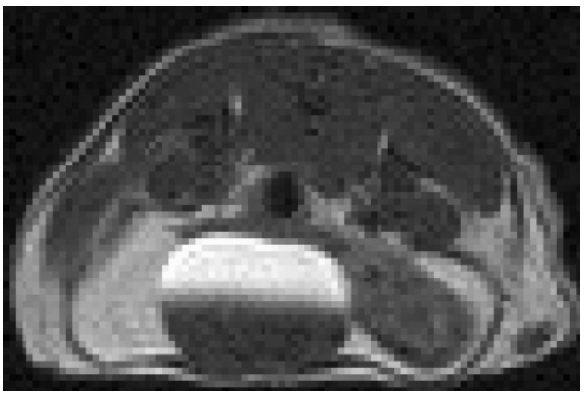

1.9.2.1 How to use the positive contrast agents?

They are a family of products with various molecular weights and biological destiny.

Small molecular weight gadolinium chelates (600 to 1000 Da) have extracellular diffusion.

Most of them (Gd-DTPA, Gd-DOTA, Gd-DTPA-BMA, Gd-HPDO3A) are rapidly eliminated by renal excretion. They diffuse quickly after injection in the extracellular compartment of all organs except brain. In brain, they diffuse only inside the lesions with blood brain barrier disruption. Thus $T1$-weighted images done after injection of the contrast agent enlighten the modification of the capillaries and of the extracellular space. When capillaries normally impermeable become leaky (in brain lesions such as tumours, abscess or inflammation) or in necrotic zones where the extracellular space volume is increased, strong signal increase is observed quickly after injection of the agent, as shown in Figure 1.9.3.

Figure 1.9.4. Myonecrosis induced by toxin injection in mouse leg. Images are obtained 24 h after injection of a snake venom toxin that induces necrosis of muscle fibres; the same slice is depicted with different contrasts that contribute to a better characterization of lesions. (a) *T*1-weighted spin-echo image with $T_R = 500$ ms, $T_E = 12$ ms. Fat signal is white. The treated leg (left of image) shows increased volume and slightly increased signal. (b) *T*2-weighted spin-echo image done with $T_R = 1500$ ms, $T_E = 102$ ms. Contrast depends heavily on *T*2. Oedema and fluids in the heterogeneous necrotic zone appear as bright. (c) *T*1-weighted spin-echo image done with the same parameters as (a), after IP injection of a positive CA (Gd-DTPA). The CA shortens *T*1 in the extracellular space. In necrotic zones where the extracellular space is increased, the mean CA concentration is higher: Necrotic leg muscles in the treated leg exhibit a strong signal increase (*images from (Wishnia et al., 2001) with permission of Neuromuscular Disorders*)

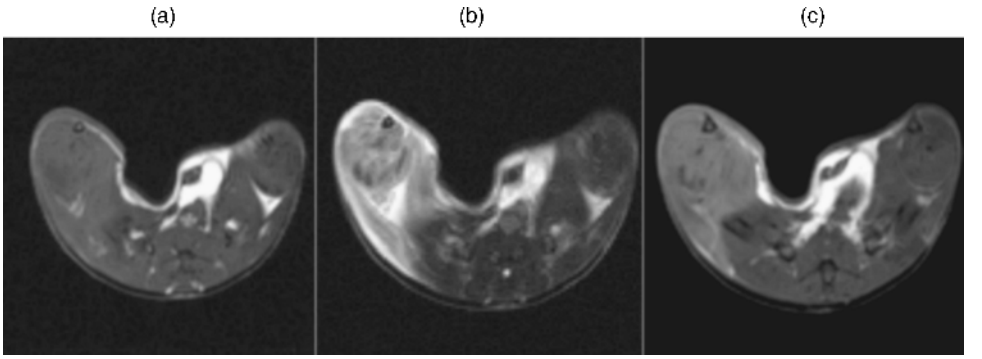

Other contrast agents (Gd-EOB-DTPA, Gd-BOPTA, MnDPP) that undergo hepatic captation, strongly increase liver signal and have hepatic elimination.

Macromolecular gadolinium chelates with molecular weight of more than 50 kDa stay in the vascular sector a longer time, making easier the visualisation of blood vessels by angiographic techniques, as shown in Figure 1.11.4, and the measurement of blood volume in an organ.

Gadolinium chelates can also be used to measure perfusion (see paragraph 1.11.7.1). This technique is named dynamic contrast enhancement (DCE). For brain studies, $T2^*$ decrease induced by a strong concentration of a positive agent around non-permeable brain capillaries is easily detected. For heart or kidney perfusion maps, *T*1 shortening is detected either with a positive agent or with a negative agent, which also shortens *T*1: Measurement of myocardial perfusion can be performed after injection of an ultra small particles of iron oxide (USPIO) at very low concentration using an imaging sequence extremely sensitive to *T*1 variations.

1.9.3 Negative contrast agents

Negative contrast agents are small particles of superparamagnetic material. The particle core made of iron oxides, of diameter 3–5 nm, is surrounded by a thick coating of a non-magnetic material such as dextran, starch, albumin or silicone. These particles are named MION (monocristalline iron oxyde nanoparticles) or more precisely SPIO (small particles of iron oxide) and USPIO depending on the thickness of coating that determine their biologic properties.

These particles behave as tiny magnets:They create a strongly heterogeneous magnetic field in their environment. The loss of homogeneity of the magnetic field causes weakening of tissue water signal. *T*2 is shortened by the diffusion of protons in the local magnetic field gradients. $T2^*$ is shortened much more efficiently: By using gradient-echo imaging, it is possible to detect these magnetic particles with a huge sensitivity. Over a distance of several microns around one particle, the signal of water is strongly diminished. This does not depend on interactions of the contrast agent with water molecules. If the particles are enclosed inside vessels or cells, they still destroy water signal at distance. Figure 14.2.1 in the report by Heryneck (Chapter 14) shows patterns of water signal destruction around 20 µg of iron inside brain.

Negative CA distribution and elimination vary with particle size: SPIO (particles with diameter 50–500 nm) are quickly cleared out of blood. Within liver and spleen, Kupffer cells selectively take these molecules up by phagocytosis. USPIO (particles with

diameter under 50 nm) stay longer in circulating blood. Measurements of vascular parameters are then possible. USPIO are taken by macrophages and can be used to visualise lymph nodes or to detect inflammatory reaction inside an organ, as done in experimental models of arthritis, multiple sclerosis, diabetes (Billotey *et al.*, 2005).

Cell labelling with a negative CA before injection has been applied to visualise migration of stem cells at the vicinity of brain ischemic lesion (Hoehn *et al.*, 2002; Jendelova *et al.*, 2005). Single cell detection was demonstrated in optimised *ex vivo* conditions; it is possible if signal-to-noise and spatial resolution are high enough: with an isotropic spatial resolution equal to $(100\ \mu m)^3$, single cells loaded by iron mass as low as 2–10 pg can be detected as a signal void, depending on the signal-to-noise availability (Heyn *et al.*, 2005). However, this high sensitivity sets a limit to quantification if many loaded cells are close from one another. Also one has to check for viability of labelled cells, because after cell death iron in the tissue is ingested by macrophages and still detected *in situ*.

New kinds of magnetic nanoparticles are now developed for molecular imaging (Lanza *et al.*, 2004).

New NMR contrast agents are presented in Chapter 7.

1.10 Imaging of 'other' nuclei

Though hydrogen nucleus is the most favourable because of its concentration in the living tissue and its high resonance frequency, imaging nuclear magnetization of other nuclei is of interest: Hyperpolarized noble gases ^{3}He, ^{129}Xe and sodium ^{23}Na are used mostly for physiological studies.

1.10.1 Hyperpolarization and NMR of noble gases

In spite of the low gas density, roughly one thousand times lower than that of water, the nuclear magnetization of hyperpolarized gases can be directly measured by NMR since their nuclear polarization is increased by up to five orders of magnitude with techniques from atomic physics. So one can start with nearly all magnetic moments parallel to the magnetic field B_0. Two noble gases, the stable isotopes ^{3}He and ^{129}Xe, bear magnetic moments that can be polarized by optical pumping and then easily detected.

More physics: how to build hyperpolarization?

There are currently two efficient techniques. They both rely on an optical pumping process by a circularly polarized laser to prepare the atoms in a polarized electronic spin state. This polarization is then transferred to the nuclei. In the first technique, optical pumping is performed on alkali atoms (e.g. rubidium) in a high temperature and pressure cell. Spin exchange collisions with ^{129}Xe or ^{3}He transfer the polarization to their nuclei. It yields polarization up to 60%. In the second technique, optical pumping is performed directly on metastable ^{3}He gas excited in a radio-frequency discharge at low pressure. Metastability exchange collisions between ^{3}He atoms eventually prepare polarized ^{3}He nuclei up to 90%.

Nuclear polarization can reach values up to 90%. This 'hyperpolarization', prepared in a low field outside of the magnet, is up to 10^5 times higher than the thermal polarization obtained at equilibrium in the magnetic field of a standard MRI magnet. Hyperpolarized gases then yield high NMR signal. This makes possible to image the air spaces of lungs, which give no signal with normal MRI techniques because water is barely present and the nuclei in air, oxygen ^{16}O and nitrogen ^{14}N, bear no net magnetic moment. Special imaging techniques are to be used to make efficient use of the hyperpolarization, because the spontaneous longitudinal relaxation brings nuclei to the much lower equilibrium polarization within 15 seconds and each RF pulse contributes to the destruction of the huge initial longitudinal magnetization.

Two gases are used for lung imaging. Helium (the weakly abundant isotope ^{3}He) is expensive but well tolerated; it is mostly used for lung imaging as illustrated by Figure 1.10.1. High resolution rat lung images has been obtained with hyperpolarized helium (Dupuich *et al.*, 2003) and now are used to study lung function and respiratory diseases (Chen *et al.*, 2000). ^{129}Xe is abundant and cheap, and because it diffuses less rapidly it should ultimately yield sharper images. Moreover, it dissolves in blood (with possible side effect as an anaesthetic at high concentration). Although hyperpolarized xenon is stable for only tens of seconds in the blood, it is enough time to quickly image its transport to the brain and to distinguish white and grey matter

Figure 1.10.1. Rat lung imaging using hyperpolarized ^{3}He. The rat is ventilated with a respiratory cycle duration 1s and the acquisition of image is synchronized with ventilation. Measurements are done using a dedicated sequence, with $T_R = 10$ ms, $T_E = 30$ μs, 900 lines, according to a radial technique (Dupuich *et al*., 2003). Spatial resolution is 156×156 μm^2 in plane, without slice selection. Each elementary image explores 1/6th of the respiratory cycle. The image displayed here is the sum of three elementary images, showing bronchic tree and alveolae filled with helium (*courtesy of Y. Cremillieux, Laboratoire de RMN, UniversitéClaude Bernard, Lyon, France*)

there. It can also be integrated into chemical carriers that allow to perform biochemical studies and angiography.

1.10.2 Sodium imaging

Sodium ^{23}Na is a 'difficult' but interesting nucleus: From the large difference between its concentration inside and outside cells, the quantification of the intracellular and extracellular sodium pools inside an organ is a sensitive index to detect and quantify ischemia and necrosis: When the intracellular ATP concentration is diminished, the function of the sodium ion pump is compromised resulting in increased intracellular sodium level. Intracellular and extracellular sodium signals are characterized by different $T2$ values, typically ranging around 1 and 40 ms, respectively. Specific imaging techniques are needed to obtain extremely short echo times, less than 1 ms, so as to ensure that both intracellular and extracellular sodium ion pools contribute to the sodium MRI signal (Constantinides *et al*., 2001). Applications to myocardial ischemia in animal modes have been published by Kim *et al*.,(1999) and Constantinides *et al*. (2001).

1.11 More parameters contributing to MRI contrast

NMR signal can be sensitised to many parameters other than Mo, T1 and T2; here we propose a list of those that are informative in the biological field. Some of them are presented in this paragraph and/or are illustrated in part II. Measurement of these parameters often requires to minimize the influence of local differences in the three major parameters, Mo, T1 and T2, a task not always easy.

Several measurement techniques are based upon modification of the water signal by magnetic agents; this concerns parameters such as

- Blood oxygenation (using haemoglobin as a contrast agent, with contrast dependent on $T2^*$),
- Blood volume (using an exogenous magnetic contrast agent),
- Vessel permeability (using an exogenous magnetic contrast agent),
- Macrophage activity (using an exogenous magnetic negative contrast agent),
- Quantification of endogenous iron accumulation,

Perfusion (using a bolus of an exogenous contrast agent).

Other measurement techniques rely upon the difference in resonance frequencies of water and other metabolites: this is the case of

- Magnetization transfer after irradiation of a proton pool other than water.
- Chemical composition of voxels, encoded by resonance frequency, in chemical shift imaging (CSI).

At last, other measurement techniques rely upon the sensitisation of the water signal to protons motion.

The measurements, which involve moving magnetic moments, rely either on $T1$ modifications or upon phase modification during the application of a magnetic field gradient. The displacement of protons is potentially a strong factor of degradation of measurements in anatomical MRI; the motion of organs creates artefacts, fought by cardiac and respiratory synchronization, or by single shot imaging. However motion of magnetic moments can be turned into a source of information. The applications where motion is detected and utilized to gain information are

– Angiography.
– Measurement of blood velocity.
– Measurement of myocardial contractility with tagging.
– Measurement of diffusion.

These parameters can be measured inside a single examination, either sequentially or sometimes interleaved with high simultaneity.

1.11.1 Quantification of iron storage

Iron is normally present in all tissues, bound to nitrogen atoms of heme in haemoglobin and myoglobin, bound to sulphur atoms in non-heme iron proteins such as aconitase, or bound to cytochroms. Storage of iron in excess is done by large proteins, hemosiderin and ferritin. In the inherited disorders of iron metabolism, as well as in chronic haemolysis, and in neurodegenerative diseases, iron accumulates in liver, kidney, heart and in specific brain zones.

Iron in solution or in a small protein may act as a paramagnetic agent that shortens the longitudinal relaxation time of blood water. Conversely, iron borne by a large storage protein, or contained in a small solid particle, has weaker influence upon $T1$ of water molecules at vicinity, but, behaving as a negative contrast agent, very efficiently 'kills' the NMR signal of water molecules at vicinity as illustrated by Figure 1.11.1.

Labelling of cells with a contrast agent made of iron oxide makes these cells detectable after transplantation.

MRI is very efficient for detection of endogenous or exogenous iron. The detection of iron, either loading a labelled cell or stored by a protein such as ferritin or hemosiderin, is based upon the strong local magnetic field around a particle of iron. This local magnetic field is inhomogeneous and large variation of water resonance frequency takes place around the particle. Thus the water signal is strongly weakened inside a volume much larger than the particle or the iron-loaded cell. The effective relaxation time $T2^*$ is the index that measures this water signal decay.

Gradient-echo imaging is very sensitive to small amounts of iron. Spin-echo imaging, less sensitive, can be used at best to evaluate more abundant iron deposits such as observed in liver with hemochromatosis. Many studies have been performed in order to quantify iron deposition in human or animal organs (Haacke *et al.*, 2005).

1.11.2 Blood oxygenation and BOLD contrast

Oxygen modulates the magnetic properties of the oxygen-binding proteins, haemoglobin and myoglobin. The deoxyhemoglobin molecule Hb, that contains one iron atom, is paramagnetic. The oxygenated haemoglobin HbO2, which combines Hb and O2 (both of them paramagnetic) is diamagnetic.

Deoxyhemoglobin in deoxygenated blood behaves as an endogenous magnetic contrast agent, contained in red blood cells. Each red cell containing Hb behaves as a small magnet. A vessel filled with deoxygenated blood can be described as a small rod filled with magnetic material, thus creating a small additional magnetic field outside the vessel. This additional magnetic field is proportional to the degree of deoxygenation of blood and to the magnetic field B_o. It also depends on the vessel size and on its orientation relative to B_o. The homogeneity of the magnetic field is degraded at short distance around the vessel leading to shortening of $T2^*$ in water surrounding the vessel. $T2^*$-weighted images, obtained by a gradient-echo sequence, are sensitive to local magnetic field inhomogeneity linked to blood deoxygenation. At last, variations of haemoglobin saturation in blood, resulting from physiological variations of oxygen supply or consumption, are translated into MR signal variations. Ogawa demonstrated on rat brain at $B_o = 7\,\mathrm{T}$ that the visibility of blood vessels as dark lines was greatly increased by blood deoxygenation (Ogawa *et al.*, 1990). He named this effect the blood oxygen level dependent (BOLD) contrast, at the origin of so many brain functional imaging studies.

BOLD contrast is widely used to detect activated neurons in many functional imaging experiments,

Figure 1.11.1 Detection of iron. Axial slice done through liver at 1.5 T with a spin-echo sequence ($T_R = 500$ ms, 8 echoes with T_E ranging from 10 ms to 80 ms). Eight images of this slice are obtained at increasing values of the echo time. The measurement of mean signal in a region of interest pasted upon these images allows to fit the signal decay and to determine the local value of *T*2. Top: normal C57/Bl6 mouse, images at $T_E = 10$ ms and $T_E = 20$ ms. Liver (black arrow) yields signal comparable to that of muscle. Liver *T*2 is 33±1 ms. Bottom: C57/Bl6 mouse 2 h after IV injection of Endorem (Guerbet, Aulnay, France) at the dose of 20 μM iron per kg. The negative contrast agent is taken by Kuppfer cells and strongly decreases liver signal. Images of echoes at $T_E = 10$ ms and $T_E = 20$ ms. Liver (white arrow) is darker than muscle at $T_E = 10$ ms and still darker at $T_E = 20$ ms. Liver *T*2 is 20±1 ms (*courtesy of C.V. Denis and D. Geldwerth, INSERM U770 at Hopital Kremlin-Bicêtre, France*)

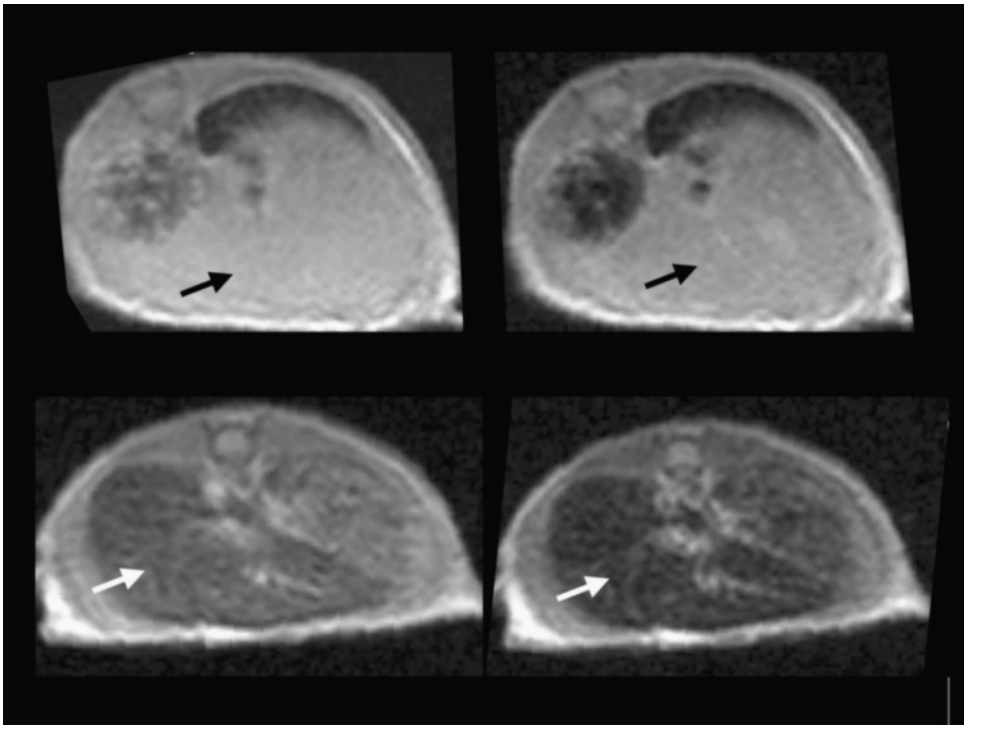

named by the acronym fMRI. Activation of brain neurons first induces an increase of oxygen consumption and a decrease of venous blood oxygenation, but it is followed a few seconds later by a strong increase of perfusion, such that venous oxygenation increases. In the activated zone, the blood oxygenation increase causes the decrease of the signal perturbation around capillaries and veins, so that the correlate of neuronal activation is NMR water signal increase (Figure 1.11.2).

This technique of localization of brain activation is fully atraumatic and offers a high spatial resolution; measurements can be done through the whole brain volume and repeated many times (as long as fatigue does not interfere with brain activity), so that complex protocols for brain stimulation can be performed. Often a repetitive stimulus is applied every 10–30 s, as perfusion adaptation typically needs 5–8 s. The coherence between the NMR signal variations and the stimulation protocol allows identification of activated voxels. The voxels where activation (or sometimes deactivation) is identified are often overlaid in colour upon an anatomical image of the same location. High-resolution BOLD studies, where voxels of 1 μl contain 600–800 neurons, can help to understand how neural networks are organized.

However, the signal variation depends on many parameters (perfusion, metabolic demand, shape of vascular tree), and its calibration in function of the

Figure 1.11.2 Detection of brain neuronal activation with an endogenous or exogenous magnetic agent. The intersection of a small vessel, filled with erythrocytes, with a brain voxel is schematised at rest (left column) and in activated state (right column). In the activated state, perfusion strongly increases; capillary oxygenation microvascular blood volume also increase. The signal of water around the vessel is displayed from white to dark grey.
Top: BOLD contrast from hemoglobin oxygenation. Water signal is weakened, from *T*2* shortening induced by the magnetization of deoxyhemoglobin in erythrocytes (represented as dark arrows). At rest, low blood oxygenation yields high extent of decreased signal around the vessel. In the activated state, higher blood oxygenation yields smaller extent of the decreased signal area and then higher signal of the corresponding voxel. Also from perfusion increase in activated brain, the capillary diameter increases.
Bottom: Exogenous contrast agent. Water signal is weakened, from *T*2* shortening induced by the magnetization of the intravascular negative contrast agent. When vessel volume increases, without significant change of the contrast agent concentration, the area of decreased signal around the vessel increases. The corresponding pixel is darker. Simultaneous variation of blood oxygenation induces much weaker signal variation

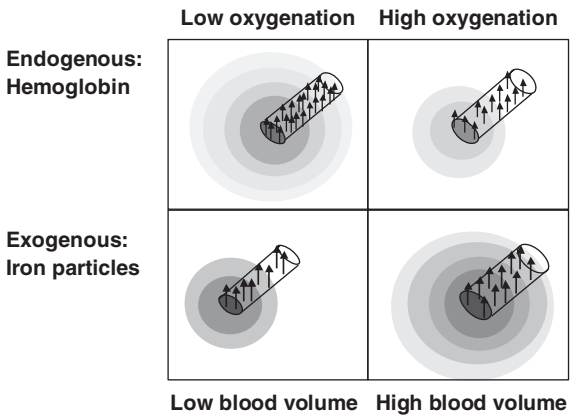

value of blood oxygen content and perfusion increase is difficult. Brain activation studies have been performed on many species from humans to rats and mice. Higher magnetic field is needed to explore smaller brains (Kim and Ogawa, 2002).

BOLD contrast detection is also applied to physiological studies of heart (Reeder *et al.*, 1999), kidney (Li *et al.*, 2003) and muscle (Jordan *et al.*, 2004).

1.11.3 Blood volume measurement using exogenous magnetic agents

After intravascular injection of a negative contrast agent with slow elimination, such as an USPIO (see 9.4), a modulation of microvascular volume can be detected from the induced variation of extravascular water signal (Figure 1.11.2). This is similar to BOLD contrast, but the magnetization of the intravascular contrast agent is much larger than that of deoxygenated hemoglobin in blood, so that the influence of oxygenation variation is negligible.

This technique is used to measure microvascular volume, and can also give information upon the distribution of vessel size in organs (Tropres *et al.*, 2004). Also the increase of sensitivity obtained by this technique allows detection of neuronal activation from the colocalized vascular volume increase. The signal variation during neuronal activation is typically 5 times higher than that detected with BOLD contrast at same B_o value and is of opposite sign as shown in Figure 1.11.2. The increase in sensitivity also makes easier the detection of neuronal activation in the brain of awake animals (Vanduffel *et al.*, 2001).

1.11.4 Manganese-enhanced MRI (MEMRI)

Another way to study brain activation uses the shortening of water *T*1 by a positive contrast agent, manganese (Lin and Koretsky, 1997) and is named manganese-enhanced MRI (MEMRI). $MnCl_2$ is an efficient paramagnetic contrast agent (not used for human studies, because Mn^{2+} ion can interfere with many enzymatic mechanisms). Small doses, around 100 μM in water, efficiently shorten tissue water *T*1. The ion Mn^{2+}, an analogue of Ca^{2+}, is taken up through voltage gated Ca^{2+} channels, so that it can reflect the activity of cardiac and nervous cells. It is concentrated in active neurons and is washed out several days after local injections, then allows detection of neuronal activation during a long time period. Mn^{2+} is transported along axons and across synapses, and it has been shown to trace neuronal connections

in the small animals central nervous system (Van der Linden *et al.*, 2004).

1.11.5 Water diffusion

Key points
Water diffusion derives from the random 3D motion of water molecules caused by thermal agitation. In tissues, it is limited by structural barriers (cell membrane, intracellular structures).

In the presence of intense magnetic field gradients, random displacements are converted into NMR signal attenuation that allows measuring the diffusion coefficient (see Figure 1.11.3).

Diffusion-weighted MRI is widely used for early detection of brain ischemia, being the first index that varies less than one hour after the ischemic event. It is also used to study connexions in the brain.

In biological tissues, water molecules are subject to the 'Brownian motion' caused by thermal agitation: Water molecules move randomly with velocities increasing with temperature and have frequent collisions with other molecules. This determines the viscosity of water in the tissue, and its diffusion coefficient.

A molecule with coefficient of diffusion D diffuses at a mean distance d from its initial location during a time interval t:

$$d^2 = 6Dt. \tag{1.48}$$

The value of the water diffusion coefficient is $2.4 \times 10^{-9}\ m^2\ s^{-1}$ in pure water at 37°C, corresponding to a mean displacement of 15 μm during 50 ms. The diffusion coefficient of water is weaker in biological tissues. It is modulated by tissue structure and by cellular energetic status.

The water coefficient D may reflect the existence of several water pools with different viscosities and of intracellular structures that limit water displacement. When cell membranes restrict the displacement of water molecules, the value of D, called ADC for apparent diffusion coefficient, depends on the time interval allowed for displacement (LeBihan, 1995, Nicolay,van der Toorn and Dijkhuizen, 1995).

In an isotropic tissues, such as muscle or brain white matter tracts, the diffusion coefficient has different values along the direction of displacement. For example, a water molecule inside an axon can move freely along the axis of the fibre, whereas it has a low probability to cross the myelin sheath. If the fibres are parallel to axis z, water diffusion is more strongly limited along the x and y axes (small cell dimensions) than along z, and the diffusion coefficient is a set of three values $D_{xx} = D_{yy} < D_{zz}$. More generally the

Figure 1.11.3 Diffusion measurement. The diffusion-weighted sequence is a spin-echo sequence including two additional large gradient pulses separated by the time interval *T*. The 180° refocusing pulse invert phases at the middle of this time interval. A magnetic moment that stayed at the same position is dephased and then rephase by the two symmetrical gradient pulses. A magnetic moment that moved from position x to x + δx during *T* is dephased by an angle $\delta\phi = \gamma . G . T . \delta x$. The addition of elementary signals with random phases causes signal attenuation

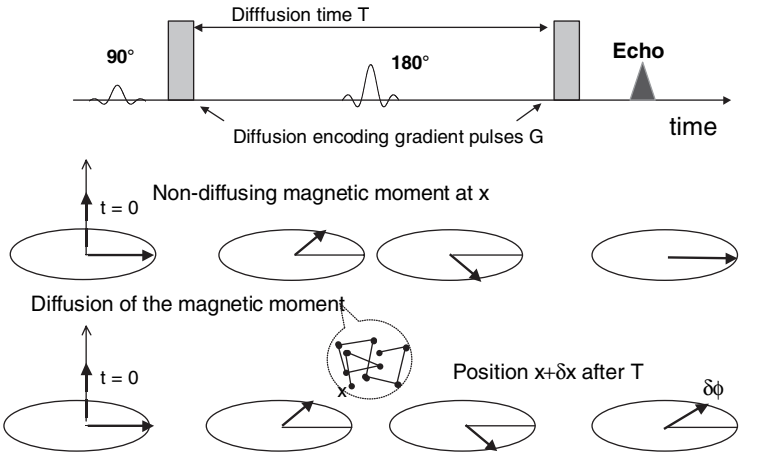

Figure 1.11.4 Multiparametric MRI study of rat cerebral ischemia induced with photochemical occlusion of proximal middle cerebral artery. Images are done at 1 h and 24 h after stroke induction using a 1.5 T clinical imaging system. In the *T*2-weighted high resolution images (T2WI) done with $T_R = 5680$ ms and $T_E = 100$ ms, no modification of signal is seen at 1 h (A1), whereas a large zone of increased signal is observed at 24 h (B1). Diffusion weighted images (DWI), obtained with a EPI spin-echo sequence, at lower spatial resolution, exhibit a zone of increased signal in the ischemic area at 1 h (A2) and 24 h (B2). The diffusion coefficient parametric image (ADC) is modified in the same area: The increased DWI signal is caused by the decreased attenuation due to the strong decrease of the water diffusion coefficient in the stroke area. The stroke is detected at 1 h after stroke induction (A2,A3) and has a wider extent at 24 h (B2,B3). Perfusion weighted images (PWI) are obtained by fast acquisition of *T*2* weighted images during the first pass of a bolus of a positive contrast agent. Brain signal is diminished in the normally perfused tissue. Images at peak of contrast agent concentration show the extent of the perfusion defect at 1 h (A4) and at 24 h (B4). The various maps obtained at 24 h correspond well to the extent of the infarct on the histologic control (*images from (Chen et al., 2004) with permission of MAGMA*)

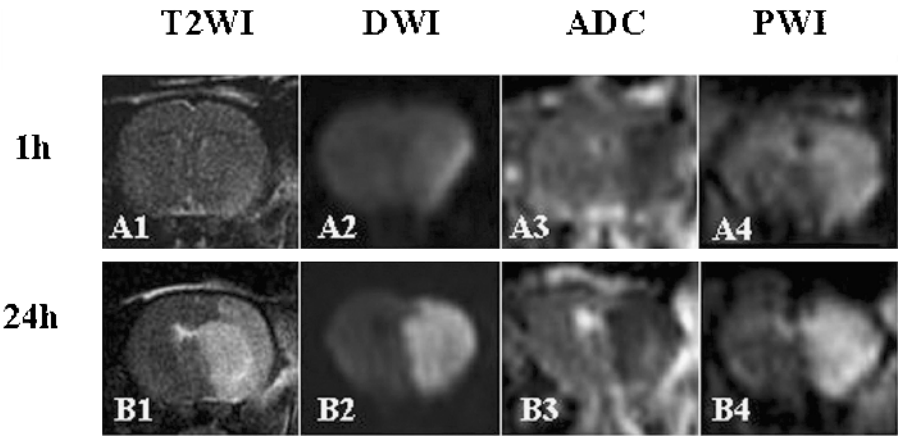

diffusion is described by a matrix of nine diffusion coefficients, the diffusion tensor. Diffusion tensor imaging (DTI) is the technique combining diffusion measurement under a combination of gradients directions that allows measuring this diffusion tensor (Zhang *et al.*, 2003).

Also, modification of cell size or content can induce large modifications of water diffusion coefficient. An important example is that of brain acute ischemia. In cat brain middle cerebral artery occlusion, the water apparent diffusion coefficient, measured by using diffusion weighted MRI, decreases strongly within 15 min following arterial occlusion (Moseley *et al.*, 1990). The decrease is around −40 to −60%, and the ADC stays at low values for several days. The stroke area, where water molecules displacements are weaker, appears as bright on diffusion-weighted images and dark on ADC maps as shown in Figure 1.11.4. This technique can be combined to other measurements such as perfusion, and it has gained much importance to measure the stroke volume and to evaluate the influence of therapies (Hoehn *et al.*, 2001).

More physics: How to measure the diffusion coefficient by using NMR

Conventional MRI utilizes contrast changes from *T*1 and *T*2 variations, reflecting the concentration of free water in tissues. Diffusion-weighted MRI utilizes the translation of water molecules during an interval of time *T*, in presence of a large magnetic field gradient: Random motion is converted into random dephasing of magnetic moments (Figure 1.11.3).

The classic diffusion-weighted sequence is a spin-echo sequence where intense gradient pulses of intensity *G* are added symmetrically before and after the 180° RF pulse. The effect of the first diffusion gradient pulse is to encode each proton with a given phase according its position, as is done during the phase encoding. If the proton does not move, the second diffusion gradient pulse brings the same phase and then (because of the 180° pulse) there is no net dephasing. Conversely if the proton has moved, there is no exact compensation of the first dephasing by the second gradient pulse: The magnetic moments that have moved randomly are dephased randomly. The

resulting transverse magnetization is decreased without global net dephasing.

The signal collected is attenuated according to an exponential law:

$$S = S_o \exp(-b.\mathrm{ADC}), \qquad (1.49)$$

where S_o is the signal in the absence of the gradient G, ADC is the 'apparent diffusion coefficient' of molecules for the applied gradient direction, b is proportional to G^2 and depends on the time interval T and the gradient G duration.

S is measured at several successive intensities of the gradient G to determine the ADC in each voxel. This makes it possible to build ADC images.

1.11.6 Magnetic resonance angiography

Magnetic resonance angiography (MRA) generates images of blood vessels (Bradley, 1992). The simplest principle for MR angiography, the 'time of flight' technique, is based upon the enhancement of magnetization caused by the flow inside a vessel, as illustrated in Figure 1.11.5. At a very short value of T_R, the signal of stationary water in the slice is weak, as $T_R \ll T1$: The time between successive measurements is too short for an efficient recovery of M_z. For blood water flowing in arteries or veins, if the velocity of blood is fast enough, that is its time of flight through the slice is shorter than T_R, in the slice under examination the water inside the vessel has not been submitted to previous selective irradiation because the circulation of blood brings fresh magnetization. Water in the vessel section has the maximal magnetization M_o. Then the vessel appears as a very bright structure on the image.

This technique requires acquisition with short values of T_R and T_E, at best obtained by 3D gradient-echo techniques. High spatial resolution is needed to visualise small diameter vessels without dilution in large voxels. Contrast agents can be injected in the vascular volume to shorten blood $T1$, in order to improve quality of the angiography (Miraux *et al.*, 2004).

Figure 1.11.5 Angiography. Magnetic resonance angiography (MRA) using the 'time of flight' method relies upon the difference in longitudinal magnetization between flowing and static water. Especially in short animals, shortening blood $T1$ with a positive contrast agent makes easier to perform 3D angiography in a given volume within a short time (Miraux *et al.*, 2004). 3D angiographic acquisition at $B_o = 4.7$ T, after intravenous injection of Gd-DOTA that improved vessels visualisation during ten minutes. Acquisition is done with a gradient-echo sequence, the flip angle is 90°; $T_R = 12$ ms, $T_E = 3.1$ ms; the acquisition time is 1 min 38 s for one volume. The displayed volume is $65 \times 38 \times 32$ mm (matrix acquisition $256 \times 128 \times 64$). Three such volumes are needed to visualise vessels from aortic cross to top of brain. (a) Jugular veins; (b) vertebral arteries; (c) sub-clavian arteries; (d) aortal; (e) right ligated common carotid; (f) left common carotid. A: axial slice from the 3D acquisition. Vessel signal is much higher than the background tissue signal. The right ligated carotid artery appears with low signal and small section. B: construction of blood vessels from the 64 slices, using a maximum intensity projection (MIP) algorithm to reconstruct 3D views of vessels. *Images from Miraux et al., (2004) with permission of MAGMA*

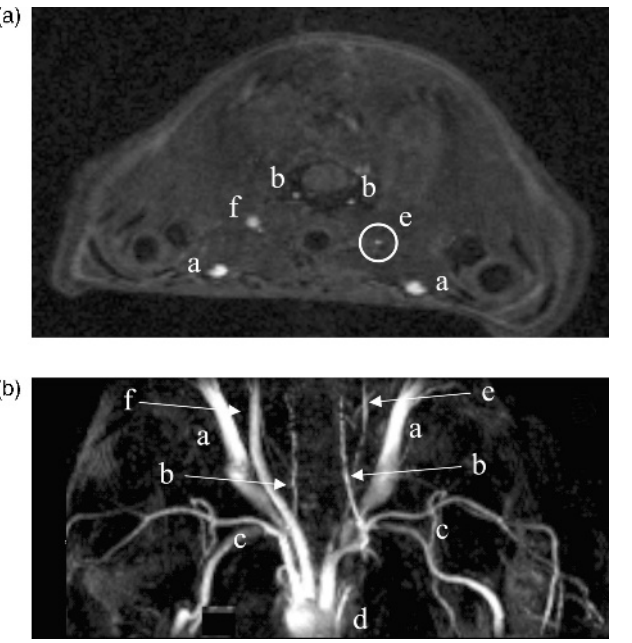

1.11.7 Perfusion measurement

Perfusion is the amount of blood flowing in the capillary bed of a given mass of tissue during a fixed period of time, delivering oxygen and nutrients. It is usually expressed in milliliters blood per 100 g tissue per min. Its value is of critical importance to maintain adequate energy status of the tissue. Perfusion measurements quantify the amount of blood flowing at low

velocity in the smallest vessels. Two distinct MRI techniques allow perfusion measurements (Barbier, Lamalle and Decorps, 2001): The first one is based upon the follow-up of a contrast agent bolus after quick injection; the second one detects blood flow from the magnetic labelling of arterial water magnetization.

1.11.7.1 Dynamic contrast enhanced imaging (DCE-MRI)

After quick intravenous injection, a magnetic contrast agent (CA) can be detected during its first passage through capillaries of the organ under study. High-speed acquisition is needed (typ. one image every 0.5 s, depending on animal size).

The CA, before dilution in the extracellular space, modifies the blood relaxation times $T1$ and $T2$. Even though the CA is confined to the vascular space, it also modifies the tissue water signal around capillaries by two distinct mechanisms:

The first one is the shortening of tissue water $T1$ by exchange with the water containing the CA in capillaries. When using a gadolinium chelate, or an USPIO at very low concentration, $T1$ shortening can be detected by a very strongly $T1$-weighted sequence. This technique is widely used to detect ischemia and to evaluate myocardial perfusion.

The second one is the shortening of tissue water $T2^*$ around the capillaries, resulting from the high CA concentration in capillaries (Figure 1.11.2). Water $T2^*$ shortening around capillaries is easily detected by gradient-echo imaging as a strong signal drop during first pass of the CA (Caramia *et al*., 1998). This technique is efficient to detect hypoperfused zones as illustrated by Figure 1.11.4, images A4 and B4. However accurate quantification of perfusion is difficult, and modification of capillary permeability can modify the curve of signal variation. Moreover there is no linear variation between the CA concentration and the signal variation. Also it is not possible to repeat perfusion measurement at short intervals because one has to wait the time needed for renal elimination after one injection.

DCE-MRI may also give information on vascular permeability. The size of the CA determines its issue out of the vascular sector, depending on capillary structure. The analysis of vascular and tissular signals by compartmental analysis of dynamic data allows to determine parameters that characterize the tissue (microvascular volume and permeability).

1.11.7.2 Arterial spin labelling

In arterial spin labelling (ASL) techniques, the blood water magnetization is used as an endogeneous contrast agent: The arterial water magnetization is modified upstream the organ by selective labelling of a thick slice containing the feeding artery (Detre *et al*., 1994). Labelling is done either by a 180° RF pulse that inverts the longitudinal magnetization M_z inside the slice or by a 90° RF pulse that zeroes the longitudinal magnetization inside the slice (see paragraph 6.1). In the slice of the organ under study, located downstream, the effect of arterial labelling is related to the perfusion that brings some water with modified magnetization (here called 'spin') into the capillaries and then into the tissue. The resulting tissue magnetization is modified by a quantity related to perfusion, so that the perfusion is quantified from the difference between an image obtained with labelling and an image obtained without labelling.

ASL techniques, that rely upon a weak difference between two images, are more easily handled at high magnetic field and in organs highly perfused such as brain and kidney (Detre *et al*., 1994), heart (Kober *et al*., 2004) (Streif *et al*., 2005) and muscle (Carlier and Bertoldi, 2005).

They allow absolute quantification of perfusion and do not require contrast agent injection, so that measurements can be repeated easily, and then allow dynamic studies under stress (Carlier and Bertoldi, 2005). With use of specific technological developments, ASL measurements can be coupled with simultaneous acquisitions of ^{1}H and ^{31}P NMR spectroscopy data. These protocols offer new possibilities whereby the microcirculatory control of cell oxygenation and high-energy phosphate metabolism can be explored (Reeder *et al*., 1999).

1.12 More about applications

Multiparametric studies combining several NMR acquisitions, to probe sequentially or simultaneously several parameters, are of particular interest. MRI and MRS sequences offer a variety of contrast. Often a fast acquisition modulus, offering short acquisition time but weak contrast, is combined with a preparation modulus that sensitises magnetization to local value of a parameter such as $T1$, $T2$, $T2^*$, perfusion, diffusion, local tissue displacement.

Anatomy and physiology are the main grounds of application for NMR techniques. NMR applications to molecular imaging are less important, because optical and nuclear imaging techniques offer a much higher sensitivity for detection of compounds at low concentration. The only compound detected with very high sensitivity is the iron atom, detected through its influence upon water signal, so that applications of NMR in the field of cellular labelling and tracking are very promising.

NMR techniques (mostly spectroscopy) have been applied to cellular physiology (Balaban, 1984) since the 1970s and to *in vivo* studies of physiology on larger biological systems since the 1980s.

The following review papers give an extended view of the applications of MRI and MRS in specific domains of biomedical research such as brain diseases (Hoehn *et al*., 2001; Dijkhuizen and Nicolay, 2003), drug discovery and development (Rudin *et al*., 1999; Beckmann *et al*., 2001), gene and cell therapies (Bell and Taylor-Robinson, 2000; Allport and Weissleder, 2001; Leroy-Willig *et al*., 2003).

Many of these applications are illustrated in Part II of this book.

References

Allport, J. R., Weissleder, R., 2001. "*In vivo* imaging of gene and cell therapies." *Exp. Hematol.* **29**, 1237–1246.

Balaban, R. S., 1984. "The application of nuclear magnetic resonance to the study of cellular physiology." *Am. J. Physiol.* **246**, C10-9.

Barbier, E. L., Lamalle, L., Decorps, M., 2001. "Methodology of brain perfusion imaging." *J. Magn. Reson. Imaging* **13**, 496–520.

Beckmann, N., Mueggler, T., Allegrini, P. R., Laurent, D., Rudin, M., 2001. "From anatomy to the target: Contributions of magnetic resonance imaging to preclinical pharmaceutical research." *Anat. Rec.* **265**, 85–100.

Bell, J. D., Taylor-Robinson, S. D., 2000. "Assessing gene expression *in vivo*: Magnetic resonance imaging and spectroscopy." *Gene Therapy* **7**, 1259–1264.

Billotey, C., Aspord, C., Beuf, O., Piaggio, E., Gazeau, F., Janier, M. F., Thivolet, C., 2005. "T-cell homing to the pancreas in autoimmune mouse models of diabetes: *In vivo* MR imaging." *Radiology* **236**, 579–587.

Bolinger, L., Prammer, M., Leigh, J., 1988. "A multiple-frequency coil with a highly uniform *B*1 field." *J. Magn. Reson.* **81**, 162–166.

Bradley, W. G., 1992. "Recent advances in magnetic resonance angiography of the brain." *Curr. Opin. Neurol. Neurosurg.* **5**, 859–862.

Bushberg, J., Seibert, J., Leidholdt, E., Boone, J., 2001. *The Essential Physics of Medical Imaging*, Lippincott, Williams and Wilkins, Philadelphia.

Caramia, F., Yoshida, T., Hamberg, L. M., Huang, Z., Hunter, G., Wanke, I., Zaharchuk, G., Moskowitz, M. A., Rosen, B. R., 1998. "Measurement of changes in cerebral blood volume in spontaneously hypertensive rats following L-arginine infusion using dynamic susceptibility contrast MRI." *Magn. Reson. Med.* **39**, 160–163.

Carlier, P. G., Bertoldi, D., 2005. "*In vivo* functional NMR imaging of resistance artery control." *Am. J. Physiol. Heart Circ. Physiol.* **288**, H1028–H1036.

Chen, F., Suzuki, Y., Nagai, N., Peeters, R., Sun, X., Coudyzer, W., Marchal, G., Ni, Y., 2004. "Rat cerebral ischemia induced with photochemical occlusion of proximal middle cerebral artery: A stroke model for MR imaging research." *Magma* **17**, 103–108.

Chen, X. J., Hedlund, L. W., Moller, H. E., Chawla, M. S., Maronpot, R. R., Johnson, G. A., 2000. "Detection of emphysema in rat lungs by using magnetic resonance measurements of ^{3}He diffusion." *Proc. Natl. Acad. Sci. USA* **97**, 11478–11481.

Constantinides, C. D., Kraitchman, D. L., O'Brien, K. O., Boada, F. E., Gillen, J., Bottomley, P. A., 2001. "Non-invasive quantification of total sodium concentrations in acute reperfused myocardial infarction using ^{23}Na MRI." *Magn. Reson. Med.* **46**, 1144–1151.

Detre, J. A., Zhang, W., Roberts, D. A., Silva, A. C., Williams, D. S., Grandis, D. J., Koretsky, A. P., Leigh, J. S., 1994. "Tissue specific perfusion imaging using arterial spin labeling." *NMR Biomed.* **7**, 75–82.

Dijkhuizen, R. M., Nicolay, K., 2003. "Magnetic resonance imaging in experimental models of brain disorders." *J. Cereb. Blood Flow Metab.* **23**, 1383–1402.

Dupuich, D., Berthezene, Y., Clouet, P. L., Stupar, V., Canet, E., Cremillieux, Y., 2003. "Dynamic ^{3}He imaging for quantification of regional lung ventilation parameters." *Magn. Reson. Med.* **50**, 777–783.

Gadian, D., 1995. *Nuclear Magnetic Resonance and its Applications to Living Systems*, Oxford University Press, New York.

Ginefri, J. C., Poirier-Quinot, M., Robert, P., Darrasse, L., 2005. "Contrast-enhanced dynamic MRI protocol with improved spatial and time resolution for *in vivo* microimaging of the mouse with a 1.5-T body scanner and a superconducting surface coil." *Magn. Reson. Imaging* **23**, 239–243.

Haacke, E. M., Cheng, N. Y., House, M. J., Liu, Q., Neelavalli, J., Ogg, R. J., Khan, A., Ayaz, M., Kirsch, W., Obenaus, A., 2005. "Imaging iron stores in the brain using magnetic resonance imaging." *Magn. Reson. Imaging* **23**, 1–25.

Heyn, C., Bowen, C. V., Rutt, B. K., Foster, P. J., 2005. "Detection threshold of single SPIO-labelled cells with FIESTA." *Magn. Reson. Med.* **53**, 312–320.

Hoehn, M., Kustermann, E., Blunk, J., Wiedermann, D., Trapp, T., Wecker, S., Focking, M., Arnold, H., Hescheler, J., Fleischmann, B. K., Schwindt, W., Buhrle, C., 2002. "Monitoring of implanted stem cell migration in vivo: a highly resolved in vivo magnetic resonance imaging investigation of experimental stroke in rat." *Proc. Natl. Acad. Sci. USA* **99**, 16267–16272.

Hoehn, M., Nicolay, K., Franke, C., van der Sanden, B., 2001. "Application of magnetic resonance to animal models of cerebral ischemia." *J. Magn. Reson. Imaging***14**, 491–509.

Hornack, 2005. The basis of MRI, http://www.cis.rit.edu/htbooks/mri.

Jacobs, R. E., Fraser, S. E., 1994. "Magnetic resonance microscopy of embryonic cell lineages and movements." *Science* **263**, 681–684.

Jendelova, P., Herynek, V., Urdzikova, L., Glogarova, K., Rahmatova, S., Fales, I., Andersson, B., Prochazka, P., Zamecnik, J., Eckschlager, T., Kobylka, P., Hajek, M., Sykova, E., 2005. "Magnetic resonance tracking of human CD34+ progenitor cells separated by means of immunomagnetic selection and transplanted into injured rat brain." *Cell Transplant* **14**, 173–182.

Johnson, G. A., Cofer, G. P., Gewalt, S. L., Hedlund, L. W., 2002. "Morphologic Phenotyping with MR Microscopy: The Visible Mouse." *Radiology* **222**, 789–793.

Johnson, G. A., Herfkens, R. J., Brown, M. A., 1985. "Tissue relaxation time: *In vivo* field dependence." *Radiology* **156**, 805–810.

Jordan, B. F., Kimpalou, J. Z., Beghein, N., Dessy, C., Feron, O., Gallez, B., 2004. "Contribution of oxygenation to BOLD contrast in exercising muscle." *Magn. Reson. Med.* **52**, 391–396.

Kim, R. J., Judd, R. M., Chen, E. L., Fieno, D. S., Parrish, T. B., Lima, J. A., 1999. "Relationship of elevated ^{23}Na magnetic resonance image intensity to infarct size after acute reperfused myocardial infarction." *Circulation* **100**, 185–192.

Kim, S. G., Ogawa, S., 2002. "Insights into new techniques for high resolution functional MRI." *Curr. Opin. Neurobiol.* **12**, 607–615.

Kober, F., Iltis, I., Izquierdo, M., Desrois, M., Ibarrola, D., Cozzone, P. J., Bernard, M., 2004. "High-resolution myocardial perfusion mapping in small animals *in vivo* by spin-labelling gradient-echo imaging." *Magn. Reson. Med.* **51**, 62–67.

Lanza, G. M., Winter, P. M., Caruthers, S. D., Morawski, A. M., Schmieder, A. H., Crowder, K. C., Wickline, S. A., 2004. "Magnetic resonance molecular imaging with nanoparticles." *J. Nucl. Cardiol.* **11**, 733–743.

LeBihan, D., 1995. "Molecular diffusion, tissue microdynamics and microstructure." *NMR Biomed.* **8**, 375–386.

Leroy-Willig, A., Fromes, Y., Paturneau-Jouas, M., Carlier, P., 2003. "Assessing gene and cell therapies applied in striated skeletal and cardiac muscle: Is there a role for nuclear magnetic resonance?" *Neuromuscul. Disord.* **13**, 397–407.

Li, L., Storey, P., Kim, D., Li, W., Prasad, P., 2003. "Kidneys in hypertensive rats show reduced response to nitric oxide synthase inhibition as evaluated by BOLD MRI." *J. Magn. Reson. Imaging* **17**, 671–675.

Lin, Y. J., Koretsky, A. P., 1997. "Manganese ion enhances *T*1-weighted MRI during brain activation: An approach to direct imaging of brain function." *Magn. Reson. Med.* **38**, 378–388.

Miraux, S., Serres, S., Thiaudiere, E., Canioni, P., Merle, M., Franconi, J. M., 2004. "Gadolinium-enhanced small-animal TOF magnetic resonance angiography." *Magma* **17**, 348–352.

Mispelter, J., Lupu, M., Briguet, A., 2006. "NMR probeheads for biophysical and biomedical experiments." *Theoretical Principles and Practical Guidelines*, Imperial College Press, London.

Moon, R., Richards, J., 1973. "Determination of intracellular pH by 31P magnetic resonance." *J. Biol. Chem.* **248**, 7276–7278.

Moseley, M. E., Kucharczyk, J., Mintorovitch, J., Cohen, Y., Kurhanewicz, J., Derugin, N., Asgari, H., Norman, D., 1990. "Diffusion-weighted MR imaging of acute stroke: correlation with *T*2-weighted and magnetic susceptibility-enhanced MR imaging in cats." *AJNR Am. J. Neuroradiol.* **11**, 423–429.

Ness Aiver, M., 1997. *All You Really Need to Know About MRI Physics*, Simply Physics, Baltimore.

Nicolay, K., van der Toorn, A., Dijkhuizen, R. M., 1995. *In vivo* diffusion spectroscopy. *An overview: NMR in Biomedicine*, vol. 8, pp. 365–374.

Ogawa, S., Lee, T., Nayak, A., Glynn, P., 1990. ''Oxygenation-sensitive contrast in magnetic resonance image of rodent brain at high magnetic fiels.'' *Magn. Reson. Med.* **14**, 68–78.

Padgett, K., Blackband, S., Grant, S., 2005.*Proceedings of the International Society for Magnetic Resonance in Medicine: 13th Scientific Meeting and Exhibition*, Miami, p. 2198.

Parzy, E., Fromes, Y., Wary, C., Vignaux, O., Giacomini, E., Leroy-Willig, A. and Carlier, P. G., 2003. ''Ultrafast multiplanar determination of left ventricular hypertrophy in spontaneously hypertensive rats with single-shot spin-echo nuclear magnetic resonance imaging.'' *J. Hypertens.* **21**, 429–436.

Reeder, S. B., Holmes, A. A., McVeigh, E. R., Forder, J. R., 1999. ''Simultaneous non-invasive determination of regional myocardial perfusion and oxygen content in rabbits: Toward direct measurement of myocardial oxygen consumption at MR imaging.'' *Radiology* **212**, 739–747.

Rinck, P., 2001. *Magnetic Resonance in Medicine: The Basic Textbook of the European Magnetic Resonance Forum*, 4th ed. Blackwell Science, Berlin, Germany.

Rudin, M., Beckmann, N., Porszasz, R., Reese, T., Bochelen, D., Sauter, A., 1999. ''*In vivo* magnetic resonance methods in pharmaceutical research: Current status and perspectives.'' *NMR Biomed.* **12**, 69–97.

Stark, D., Bradley, W. J., 1992. *Magnetic Resonance Imaging*, Mosby-Year Books, St. Louis.

Streif, J. U., Nahrendorf, M., Hiller, K. H., Waller, C., Wiesmann, F., Rommel, E., Haase, A., Bauer, W. R., 2005. ''*In vivo* assessment of absolute perfusion and intracapillary blood volume in the murine myocardium by spin labelling magnetic resonance imaging.'' *Magn. Reson. Med.* **53**, 584–592.

Tropres, I., Lamalle, L., Peoc'h, M., Farion, R., Usson, Y., Decorps, M., Remy, C., 2004. ''*In vivo* assessment of tumoural angiogenesis.'' *Magn. Reson. Med.* **51**, 533–541.

Van der Linden, A., Van Meir, V., Tindemans, I., Verhoye, M., Balthazart, J., 2004. ''Applications of manganese-enhanced magnetic resonance imaging (MEMRI) to image brain plasticity in song birds.'' *NMR Biomed.* **17**, 602–612.

Vanduffel, W., Fize, D., Mandeville, J. B., Nelissen, K., Van Hecke, P., Rosen, B. R., Tootell, R. B., Orban, G. A., 2001. ''Visual motion processing investigated using contrast agent-enhanced fMRI in awake behaving monkeys.'' *Neuron* **32**, 565–577.

Webb, A., 2003. *Introduction to Biomedical Imaging*, John Wiley & Sons, Inc., Hoboken, New Jersey.

Webb, A., 2003. *Introduction to Biomedical Imaging*, John Wiley & Sons, Inc., Hoboken, New Jersey.

Wishnia, A., Alameddine, H., Tardif de Gery, S., Leroy-Willig, A., 2001. ''Use of magnetic resonance imaging for non-invasive characterization and follow-up of an experimental injury to normal mouse muscles.'' *Neuromuscul. Disord.* **11**, 50–55.

Zhang, J., Richards, L. J., Yarowsky, P., Huang, H., van Zijl, P. C., Mori, S., 2003. ''Three-dimensional anatomical characterization of the developing mouse brain by diffusion tensor microimaging.'' *Neuroimage* **20**, 1639–1648.